Department of Precision and Microsystems Engineering

# Design Study of a Diamagnetic Long-Range Movement Stage Actuated by Electrostatic Force

Lucas Wiedenhoff

| | |
|---|---|
| Report no | : 2025.061 |
| Coach | : Peter Steeneken |
| Professor | : Peter Steeneken |
| Specialisation | : Engineering Dynamics |
| Type of report | : Master Thesis |
| Date | : 19 September 2025 |

Delft University of Technology

Challenge the future

# Design Study of a Diamagnetic Long-Range Movement Stage Actuated by Electrostatic Force

by

Lucas Wiedenhoff

to obtain the degree of Master of Science
at the Delft University of Technology,
to be defended publicly on Friday September 19, 2025 at 11:00 AM.

| | | |
|---|---|---|
| Student number: | 4952332 | |
| Project duration: | May 23, 2024 – September 19, 2025 | |
| Thesis committee: | Prof. dr. P. G. Steeneken, | TU Delft Professor, supervisor |
| | Dr. F. Alijani, | TU Delft Associate Professor |

# Preface

Dear reader

This master thesis presents my first contribution to the world of engineering and is the result of the accumulated knowledge and experience of my studies at TU Delft. The project has been both challenging and rewarding. Spanning a full year, it allowed room for trial and error while also providing the opportunity to develop solutions.

I am deeply grateful for the support I received, which helped me tremendously with exploring the subject. The guidance I have received from Prof.dr.Steeneken always proved valuable and allowed me to form ideas and to evaluate these ideas. The discussions I had with my fellow researchers on the subject of diamagnetism helped form a better picture of the possibility. The 3ME-PME Lab support team provided support for designing and building my setup. And I also want to thank my family and friends for their support and thoughtful encouragement.

*Lucas Wiedenhoff*
*Delft, Augustus 2025*

# Abstract

Diamagnetic levitation provides a frictionless and entirely passive method of actuation, operating even in vacuum and at cryogenic temperatures. It has been explored in fields ranging from seismology to microfluidics handling, and its qualities make it attractive for MEMS devices by reducing production costs and improving robustness.

This work develops a diamagnetic motion stage aimed at extending the achievable range of motion beyond prior nanometer-scale demonstrations. This objective is formulated as the following research question: **What would be an optimal design for a long range actuator to create maximum movement range using diamagnetic levitation to eliminate contact friction and electrostatic force as propulsion method using only feedforward control, while keeping the cost low?**. Magnet arrays were modeled, with a railroad configuration selected for its levitation properties. An electrostatic actuation model was derived, showing that force depends on both electrode area and its change as a result of movement, and that stable control requires balancing charged and grounded electrodes.

Two systems were implemented: a low-voltage (0–200 V) setup with high control but low force, and a high-voltage (0–1200 V) setup with greater force but less control. Characterization revealed Duffing-type nonlinear dynamics. The low-voltage stage enabled three-phase frequency control, useful for resonance testing, while the high-voltage stage achieved up to 5.5 mm controlled travel and 23.47 mm one-way displacement, though with the end position being unrecoverable using electrostatics.

The results show that longer travel requires repeating magnet arrays where all potential local minima support levitation. Another important finding was that electrostatic force has both x and z components, with their ratio depending on levitation height and stage surface area, highlighting the importance of thin electrodes. Scaling analysis suggests further potential for MEMS integration.

# Contents

# Nomenclature

## Symbols

| Symbol | Definition | Unit |
|---|---|---|
| $\vec{F}$ | Force | $N$ |
| $\vec{F}_g$ | Gravitational force | $N$ |
| $E'$ | Co-energy | $J$ |
| $\vec{M}$ | Magnetization | $A/m$ |
| $\vec{B}$ | Magnetic Flux Density | $T$ |
| $\chi$ | Magnetic susceptibility | $-$ |
| $\mu_0$ | Permeability of free space | $N/A^2$ |
| $V$ | Volume | $m^3$ |
| $m$ | Mass | $kg$ |
| $\rho$ | Density | $kg/m^3$ |
| $g$ | Acceleration due to gravity | $m/s^2$ |
| $Q$ | Charge | $C$ |
| $C$ | Capacitance | $F$ |
| $U$ | Voltage | $V$ |
| $\epsilon$ | Electric permittivity | $F/m$ |
| $A$ | Common surface area | $m^2$ |
| $l$ | Common covered length | $m$ |
| $z$ | Height in $\hat{k}$-direction | $m$ |
| $\omega_n$ | Eigen frequency | $rad/s$ |
| $c$ | Damping coefficient | $Ns/m$ |
| $k$ | Stiffness | $N/m$ |
| $t$ | Time | $s$ |
| $\hat{k}$ | Z direction unit vector | $-$ |
| $\vec{\nabla}$ | Gradient operator | $-$ |
| $H$ | Hessian matrix | $-$ |

## Acronyms

| Acronym | Full Word |
|---|---|
| MEMS | Micro-Electromechanical Systems |
| HOPG | Highly oriented pyrolytic graphite |
| DOF | Degree of freedom |
| PCB | Printed circuit board |
| FEM | Finite element method |

# 1

# Introduction

## 1.1. Motivation

Levitation offers numerous advantages, primarily due to the absence of contact forces. Eliminating contact removes friction and hysteresis. Diamagnetic levitation adds two more benefits compared to other forms of levitation like electromagnetic and acoustic levitation: it is passive and can function in a vacuum. Diamagnetic levitation uses the negative magnetic susceptibility to levitate, as such only requires permanent magnets. As it is passive an actuation method is required, in this research electrostatic force is used for this.

Permanent magnets are inexpensive to produce, and electrodes can be precisely manufactured using printed circuit board (PCB) technology. As a result, high-precision, large-range motion stages can be produced more cost-effectively. Additionally, depending on the design, such stages may also be more reliable. Passive levitation allows the system to return to a stable resting position upon shutdown. Moreover, this approach can be more energy efficient, as minimal heat is generated during electrode charging and discharging, and leakage currents can be limited using isolation.

These characteristics are very valuable in the production and operation of Micro-Electromechanical Systems (MEMS), which require nanometer-level precision. MEMS fabrication is often performed in vacuum environments, as illustrated by companies like [1]. They could also be applied to new use cases; for example, micro-bots could be used for micro fluid handling, connecting modular lab equipment, micro-construction in vacuum and/or cryogenic environments, or sampling in sterile environments.

Diamagnetic levitation has previously been combined with various actuation methods. The most common approach involves electromagnetic actuation for both actuators [2]–[11] and rotors [12], [13]. Other methods include photothermal actuation [14]–[20]. Finally, electrostatic actuation has also been explored for both rotors and actuators [21]–[25]. This method is particularly appealing because it works in vacuum and can be very energy efficient and precise. Section 1.3 reviews the findings of previous studies, which this research seeks to build upon and further develop.

## 1.2. Thesis Outline

The first chapter covers previous work on diamagnetic levitating motion stages and the insights gained from them. The second chapter explains the physics used in this paper to provide a better understanding of diamagnetic levitation and electrostatic forces, as well as the theory behind the motion stage design. The third chapter presents the design derived from the theory and the insights gained during the research. The fourth chapter covers various models used in designing the PCB and magnet array. The fifth chapter discusses the setup used to create and manage the voltages for the electrostatics. It also details the measurement techniques employed. The sixth chapter analyzes the characteristics of the magnet array to quantify the possible motions. The seventh chapter discusses the motions achieved through different applications of electrostatic force. The eighth chapter summarizes the research and draws key insights from the results. The ninth chapter presents the conclusion, addresses the main research question, and outlines possible directions for future research.

## 1.3. Literature Review

This section discusses previous work relevant to this research to gain insights and foundational knowledge on the subject.

### 1.3.1. Search Strategy

To ensure comprehensive coverage of relevant literature, a combination of backward citation tracking and gap analysis was used. In backward citation tracking, references from existing papers are used to discover additional sources, and this process is repeated iteratively. Gap analysis is then applied to identify any missing but potentially relevant works not covered by the citation chain.

### 1.3.2. Electrostatic Stage

By applying the principle that opposite charges attract, an electrostatic force can be generated. This force, when combined with active control, can be used for actuation, as demonstrated in [26] to create a moving stage. Figure 1.1a illustrates how electrodes are used for levitation and propulsion. When an electrode is charged, the stage becomes locally oppositely charged. Then, by grounding the initial electrode and charging the next one, the stage is pulled forward. Figure 1.1b shows the complete setup.

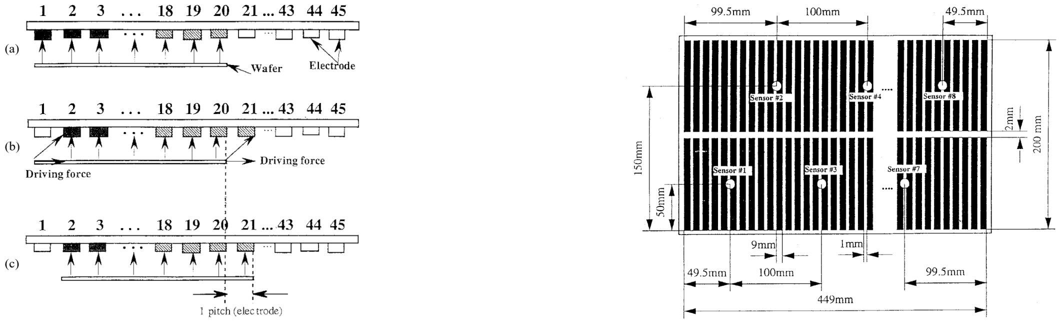

(a) Phases and stages used.

(b) Workspace setup.

Figure 1.1: Technique and setup from [26].

### 1.3.3. Diamagnetic Electrostatic Movement Stage

The same principle was combined with diamagnetic levitation by [24], marking the first attempt to use electrostatic actuation in such systems. Two configurations were explored. In the first (Figure 1.2a), a basic pyrolytic graphite plate with a small glass plate on top is levitated. An electrostatic comb above the plate generates a charge in the glass. Since the glass is non-conductive, it stays locally charged, attracting the comb's subsequent sections. In the second configuration (Figure 1.2b), comb electrodes are placed both above and on the stage. These electrodes are charged with a phase shift to produce a forward electrostatic force; however, this is not pure levitation, as the second comb must remain connected to the function generator.

(a) First configuration with a glass plate on the stage.

(b) Second configuration with comb electrodes on the stage.

Figure 1.2: Two configurations tested in [24].

### 1.3.4. Diamagnetic Electromagnetic Movement Stage

Long-range actuation in diamagnetic systems was first demonstrated in [24], using an additional magnetic force. As shown in Figure 1.3, a ferromagnetic rod is levitated using diamagnetism and actuated by a separate electromagnetic coil.

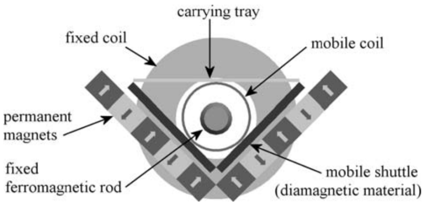

Figure 1.3: A magnetic array placed in V-shape [24].

Several studies [2], [3], [6]–[10] employ a $3 \times 3$ magnet array with pyrolytic graphite, where wires below generate a magnetic field (Figure 1.4). In [6], micro-robots with various end-effectors perform tasks such as collaborative tower building (Figure 1.5a). In [7], [8], a micro-robot manipulator is designed for microprocessing tasks. [2] uses the same robot for microfluidic handling (Figure 1.5b).

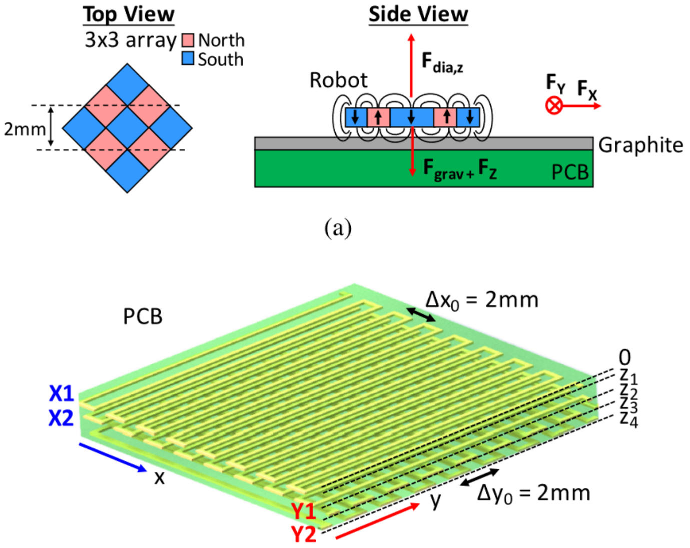

Figure 1.4: A magnetic array levitated above diamagnetic plate [2].

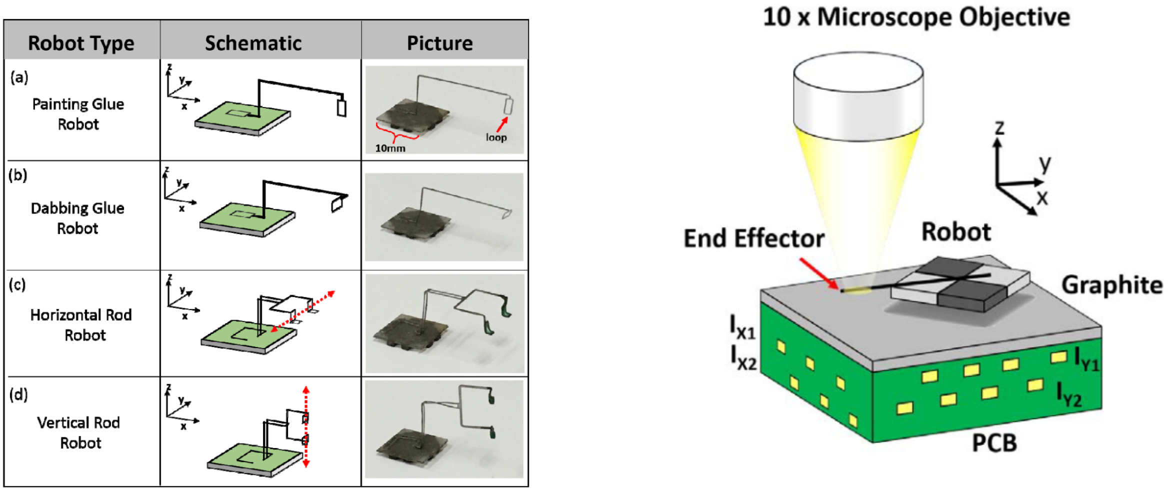

(a) Micro-robots with different end-effectors [6].

(b) Micro-robot manipulator for micro-spheres [7].

Figure 1.5: Applications of micro-bots.

### 1.3.5. Characterization

In [23], the conductive properties of graphite are used in a novel three-plate conductor setup (Figure 1.6). A magnetic array provides 1D motion at the base. Two electrodes are placed on top of the magnets, and a pyrolytic graphite plate is levitated above them. When one electrode is charged, charges redistribute within the stage, creating a dipole. The resulting electrostatic attraction moves the stage.

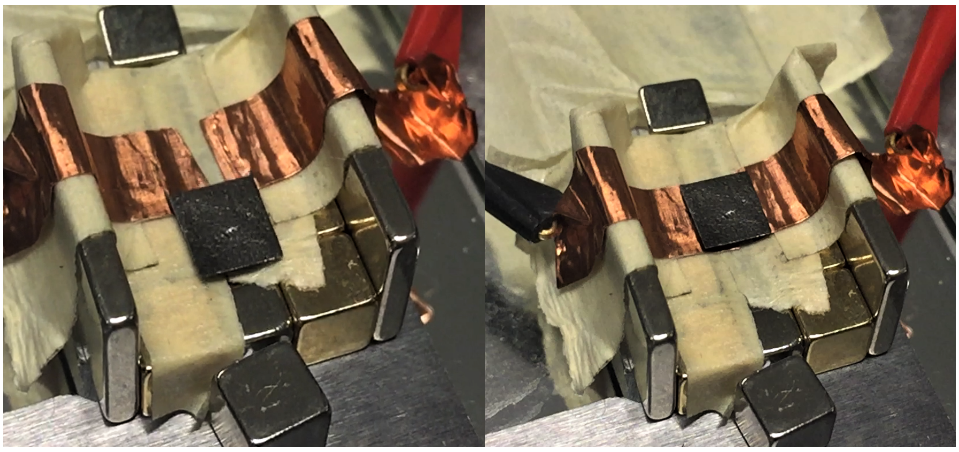

Figure 1.6: Three-plate electrostatic configuration [23].

### 1.3.6. Positioning Stage

In [4], two actuators with three degrees of freedom (DOF) each are combined to manipulate a single stage, enabling five-DOF movement (Figure 1.7a).

[27] introduces a micro-actuation configuration using electrostatic forces. The system starts with a $2 \times 2$ magnet array, followed by a thin PCB with electrode patterns (Figure 1.7b). The PCB can be isolated or open. Above it, a small HOPG plate, coated in gold for improved conductivity, is levitated. Two configurations are shown: the original setup does not separate lateral and rotational movement, while the improved design allows independent control.

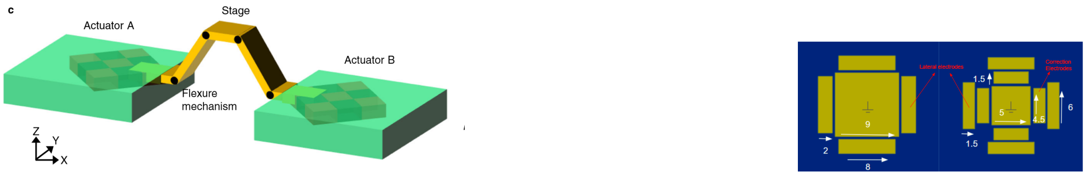

(a) Two actuators controlling a single stage [4].

(b) Left: original design; Right: improved design [27].

Figure 1.7: Two examples of positioning stages.

## 1.4. Project Proposal

The article [24] demonstrated a 1D motion actuator using electrostatic force, but it was tethered by cables, so it cannot be classified as pure levitation. The article [27] demonstrates a similar but distinct method to create a positioning stage. The stage is charged by the charged electrode and discharged by the ground electrode, with the resulting charge differential between the electrodes pulling the stage, as first illustrated in [23]. This method could enable a motion stage using the conductivity of graphite, which so far has only been employed for positioning stages, not for longe range motions.

A motion stage made using HOPG, levitated using permanent magnets and actuated by electrostatic force, has been demonstrated as feasible. However, moving this stage over large distances has not yet been achieved. Such long distance stages could be used to develop micro-bots, similar to those actuated by electromagnetic force. These micro-bots could transport micro-scale liquids or potentially connect modular lab equipment. Additionally, they may have applications in manufacturing, as they can function in vacuum, cryogenic, and heated environments (up to the Curie temperature).

### Research Question

The research question for this thesis is as follows:

**What would be an optimal design for a long range actuator to create maximum movement range using diamagnetic levitation to eliminate contact friction and electrostatic force as propulsion method using only feedforward control, while keeping the cost low?**

To answer this question the following sub-questions are defined:

- What is the optimal design for the electrode design?
- What is the optimal design for the magnet array?
- What is the optimal design for the HOPG stage?
- What do different control strategies provide in terms of control and movement range?
- What are necessary costs of different parts of the movement stage?

# 2

# Background Theory

The following sections present the theoretical foundations used for the design process. First, the properties of diamagnetic levitation are discussed, along with previously developed magnet arrays. Next, electrostatics is explored using the parallel plate model, including its implications on the design and a review of earlier implementations.

## 2.1. Diamagnetism

This section covers the theoretical background of diamagnetism relevant to the motion stage design. It begins with an overview of suitable materials, followed by analytical formulas for the diamagnetic force. Then, stability requirements for levitation are briefly discussed, and finally, magnetic arrays found in literature are reviewed.

### 2.1.1. Diamagnetic Materials

Diamagnetic materials are non-ferromagnetic and exhibit negative magnetic susceptibility. This means that when placed in an external magnetic field, the material becomes magnetized in the opposite direction.

Using Ansys Granta EduPack [28], all diamagnetic elements were plotted in Figure 2.1, where the x-axis represents density and the y-axis shows the negative magnetic susceptibility on a logarithmic scale. To maximize diamagnetic lift and minimize gravitational pull, materials with high (negative) susceptibility and low density are preferred—i.e., materials located in the top-left corner of the graph. From equation 2.7, the term $\frac{\chi V}{\mu_0}$ indicates that materials following a line of slope 1 (on a log-log plot) offer the same levitation force-to-weight ratio. Carbon appears to be the most favorable, followed by thallium and hydrogen, and to a lesser degree, germanium and beryllium.

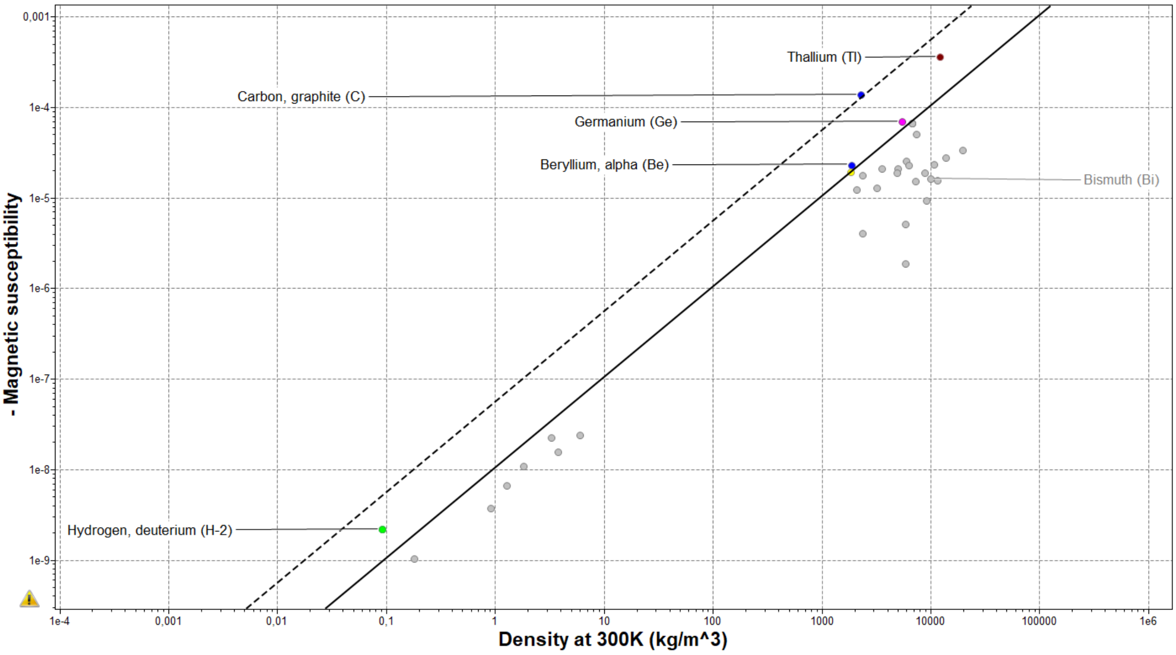

Figure 2.1: Material selection: density vs. magnetic susceptibility (log scale). Line indicates a constant $\frac{\chi}{\rho}$ ratio.

Although carbon is an ideal elemental candidate, its performance is enhanced when structured as graphite (carbon arranged in hexagonal crystals), particularly in its pyrolytic form (graphite with precisely aligned layers). Pyrolytic graphite was first identified as a diamagnetic material in [29] and was used in early zero-contact bearing systems ([30]).

A more refined form, highly oriented pyrolytic graphite (HOPG), is produced by applying tension during the pyrolytic process. This alignment enhances its susceptibility in one direction while reducing it in others. Tables below show the relevant properties.

| **Property** | **Value** |
|---|---|
| Density | 2070 [kg/m$^3$] |
| Magnetic Susceptibility (Perpendicular) | -450 $\times 10^{-6}$ |
| Magnetic Susceptibility (Parallel) | -85 $\times 10^{-6}$ |

Table 2.1: Properties of highly oriented pyrolytic graphite (HOPG).

Both materials are commonly used in diamagnetic levitation systems. Pyrolytic graphite is used in works such as [23], [31]–[33], among others. HOPG is used in [17], [27], [34]–[36].

### 2.1.2. Diamagnetic Levitation

The problem with passive magnetic levitation, as stated by Earnshaw's theorem, is that every stable point of a point charge in a magnetic field is a saddle point ([23], [37]). A workaround used for Earnshaw's theorem in achieving stable magnetic levitation involves using diamagnetic materials. A negative magnetic susceptibility means that these materials always become magnetized in the direction opposite to the applied magnetic field. This property enables stable magnetic levitation.

#### Diamagnetic Force

The magnetization in the diamagnetic material is calculated using Equation eq. 2.1. Here $\vec{M}$ is the magnetization vector and $\vec{B}$ is the magnetic flux density vector. $\chi$ is the magnetic susceptibility, and $\mu_0$ is the permeability of free space.

$$\vec{M} = \frac{\chi}{\mu_0} * \vec{B} \tag{2.1}$$

The co-energy [38] of diamagnetic materials in a magnetic field is calculated using eq. 2.2. For simplicity the magnetic field is taken as a constant, for precise calculations this should be kept as a volume integral. Here $E'$ is the co-energy and V is the volume. $\nabla$ is the gradient operator.

$$E' = -\frac{1}{2} * \int_V \vec{M} \cdot \vec{B} dV = -(\frac{\chi * V}{2 * \mu_0}) * ||\vec{B}||^2 \tag{2.2}$$

Now, the force vector is calculated using the negative derivative of the co-energy eq. 2.3 resulting in eq. 2.4.

$$\vec{F_B} = -\nabla E' \tag{2.3}$$

$$\vec{F_B} = \frac{1}{2} \nabla \int_V \vec{M} \cdot \vec{B} \mathrm{d}V = (\frac{\chi * V}{2 * \mu_0}) * \nabla \cdot ||\vec{B}||^2 \tag{2.4}$$

The force vector in the z-direction is calculated from eq. 2.4 by taking only the z-component of $Grad(||\vec{B}||^2)$. This gives eq. 2.5. Here it can be seen that the force generated would depend on both on the magnetic field and its gradient.

$$F_{B,z} = (\frac{\chi * V}{\mu_0}) * \vec{B} \cdot \frac{\vec{B}}{dz} \hat{k} \tag{2.5}$$

To balance out gravity. $F_{B,z} = F_g = m * g * \hat{k}$ results in eq. 2.6. Here $m$ is the mass, $g$ is the acceleration due to gravity and $\hat{k}$ is the directional unit vector in the z (upward) direction.

$$(\frac{\chi * V}{\mu_0}) * \vec{B} \cdot \frac{d\vec{B}}{dz} \hat{k} = m * g * \hat{k} \tag{2.6}$$

Eq. 2.6 can be used to make eq. 2.7. In this equation $\rho$ is the density. The formula can be split into three parts $\vec{B} \cdot \frac{d\vec{B}}{dz}$, $\frac{\chi}{\rho}$ and $\mu_0 * g * \hat{k}$. The first part shows the relevance of both the strength of the magnetic field and the change in the magnetic field. The second part shows the effect of the material properties. The third part represents the constants.

$$(\frac{\chi}{\rho}) * (\vec{B} \cdot \frac{d\vec{B}}{dz} \hat{k}) = \mu_0 * g * \hat{k} \tag{2.7}$$

**Stable levitation**

For static stability, the co-energy of the diamagnetic effect and the potential energy of gravity should be considered, as shown in eq. 2.8.

$$E' = -(\frac{\chi * V}{2 * \mu_0}) * ||\vec{B}||^2 + m * g * z \tag{2.8}$$

To make an equilibrium stable, the Hessian matrix 2.9 needs to be positive definite.

$$H = \begin{pmatrix} \frac{\partial^2 E'}{\partial x^2} & \frac{\partial^2 E'}{\partial x \partial y} & \frac{\partial^2 E'}{\partial x \partial z} \\ \frac{\partial^2 E'}{\partial y \partial x} & \frac{\partial^2 E'}{\partial y^2} & \frac{\partial^2 E'}{\partial y \partial z} \\ \frac{\partial^2 E'}{\partial z \partial x} & \frac{\partial^2 E'}{\partial z \partial y} & \frac{\partial^2 E'}{\partial z^2} \end{pmatrix} \tag{2.9}$$

Given that $\chi < 0$, $V > 0$ & $\mu_0 > 0$, eq. 2.10 needs to hold true for the Hessian matrix to be positive definite [37]. This implies that the magnetic field needs to get stronger in all directions for a stable equilibrium. The possible configurations found in the literature can be seen in Section 2.1.3.

$$\frac{\partial^2 B^2}{\partial x^2} > 0, \frac{\partial^2 B^2}{\partial y^2} > 0, \frac{\partial^2 B^2}{\partial z^2} > 0 \tag{2.10}$$

### 2.1.3. Magnetic Arrays

To achieve stable levitation, various magnet array configurations have been used in previous studies. In all cases, north and south poles can be swapped, provided the configuration is consistent.

#### Checkerboard Magnet Array

One of the most widely used magnet arrays is the checkerboard array, as shown in Figure 2.2. In this design, square magnets are placed in an alternating pattern, with north and south poles facing upwards in a checkerboard-like arrangement. This array is commonly used in [2], [3], [6]–[10], [27].

At the intersection points where two north poles and two south poles meet, local magnetic field minima are formed, which provide stable levitation points. Due to the symmetry of this configuration, it offers equal stability in both in-plane directions, making it especially suitable for 2D motion. Additionally, using a larger diamagnetic stage helps smooth out local field variations. Since the diamagnetic force is the result of an integral over the entire volume, the stage averages the field, resulting in more uniform behavior.

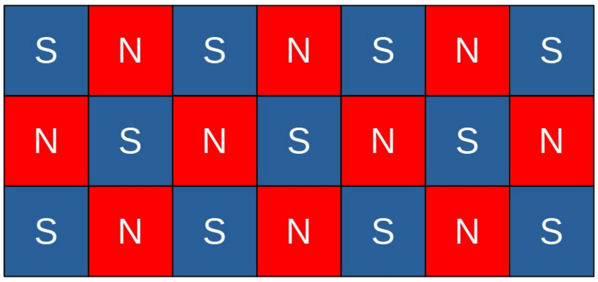

Figure 2.2: Theoretic top view of checkerboard magnet array.

#### 3 Long Magnet Array

A simpler alternative is the 3 long magnet array, which uses a narrow central local minimum for levitation. It consists of three long bar magnets: the middle one with its north pole facing up, and the two outer magnets with south poles facing up, aligned parallel and close to the central magnet (Figure 2.3a).

This creates a narrow region in the middle of the magnets where the magnetic field gradient allows for stable levitation. The design can be modified by adding stopper magnets at the ends of the array. These slightly increase the local field gradient, improving levitation stability and making the setup process easier. This configuration is used in [23], as illustrated in Figure 2.3b.

(a) Without stopper magnets.

(b) With stopper magnets.

Figure 2.3: Theoretic top views of 3 long magnet arrays, without and with stopper magnets.

### Halbach Magnet Array

A Halbach array works similarly to the checkerboard configuration but includes a special arrangement of magnet orientations. A typical implementation requires a minimum of five magnets in width, with some placed sideways to create a one-sided magnetic field. This field is concentrated above the array, with the magnetic field below being weaker.

The Halbach array can also be used in 1D setups similar to the 3 long magnet array. However, it is less commonly used due to increased manufacturing complexity, and it does not gain new field characteristics over simpler designs, only magnetic field strength. It is employed in setups like [39].

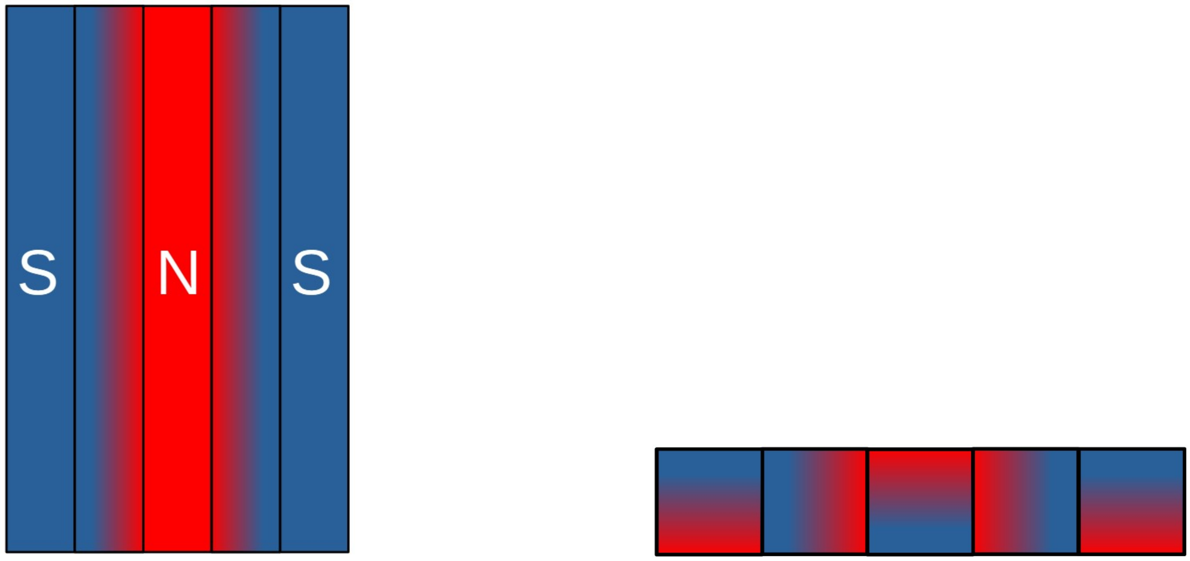

(a) Top view.

(b) Front view.

Figure 2.4: Theoretic Halbach magnet array.

### Railroad Magnet Array

First proposed in [23], the railroad array combines a central long magnet with multiple smaller magnets to generate multiple local minima. The central magnet is placed with its north pole facing up, while smaller magnets on both sides have their south poles facing up, forming “rails” (Figure 2.5a).

This configuration creates multiple small magnetic potential wells, which can enhance lateral stability. The array can be assembled in different ways. As without any extra constraints the side magnets repel each other, which leads to them not being able to be placed against each other, this can be seen in Figure 2.5a. A form of constraint is a steel plate, that is used to hold the magnets in place via magnetic attraction. Alternatively, tape or other mechanical constraints can be used to maintain the array’s structure, as seen in Figure 2.5b.

(a) Without steel floor.

(b) With steel floor.

Figure 2.5: Theoretic top views of railroad magnet arrays, without and with steel floor.

## 2.2. Electrostatics

The electrostatic force was selected as the propulsion method for its potential for high efficiency and precision. The governing equations for the electrostatic forces and co-energy are derived from the parallel plate capacitor theory to better understand their characteristics. This is followed by a brief overview of electrode designs from the literature.

### 2.2.1. Electrostatic Force

The double capacitor is circuit is presented in Figure 2.6.

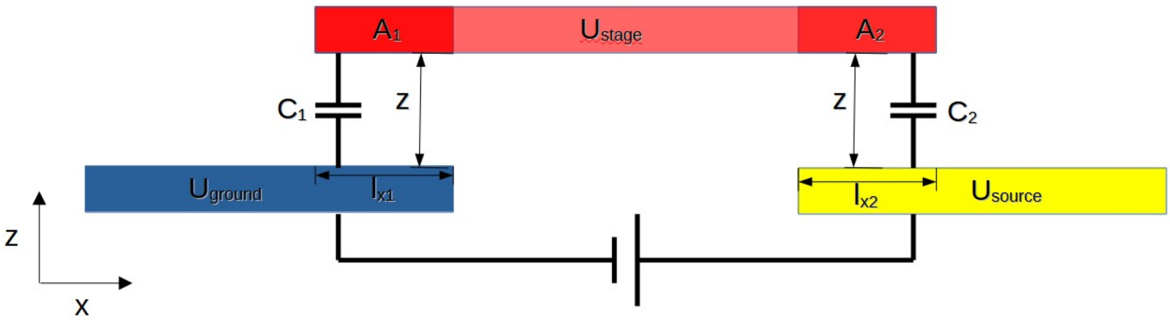

Figure 2.6: the Electrical circuit. Common covered length and voltage in the $x$ and $z$ directions are shown. Blue: ground electrode, red: stage, yellow: charged electrode.

The charge on the stage can be calculated using the following equations, where $Q$ is charge, $C$ is capacitance, $U$ is voltage:

$$Q_{stage,ground} = C_1(U_{stage} - U_{ground}) \tag{2.11}$$

$$Q_{stage,source} = C_2(U_{source} - U_{stage}) \tag{2.12}$$

$$Q_{stage,ground} = Q_{stage,source} \tag{2.13}$$

This leads to the voltage on the stage:

$$U_{stage} = \frac{C_2}{C_1 + C_2} * U_{source} \tag{2.14}$$

the total co-energy is given by eq. 2.15:

$$E' = -\frac{Q^2_{stage,ground}}{2C_1} - \frac{Q^2_{stage,source}}{2C_2} \tag{2.15}$$

Substituting eq. 2.14 into eq. 2.15 results in:

$$E' = -\frac{U^2_{source} C_1 C_2}{2(C_1 + C_2)} \tag{2.16}$$

The capacitance of the air between the source and ground, and the stage can be given by eq. 2.18 and eq. 2.17. Here, $\epsilon$ is the vacuum permittivity, $A_{stage,ground}$ & $A_{stage,source}$ are the surface areas, expressed as $l_{x1} * l_{y1}$ and $l_{x2} * l_{y2}$, as can be seen in Figure 2.7 and Figure 2.6.

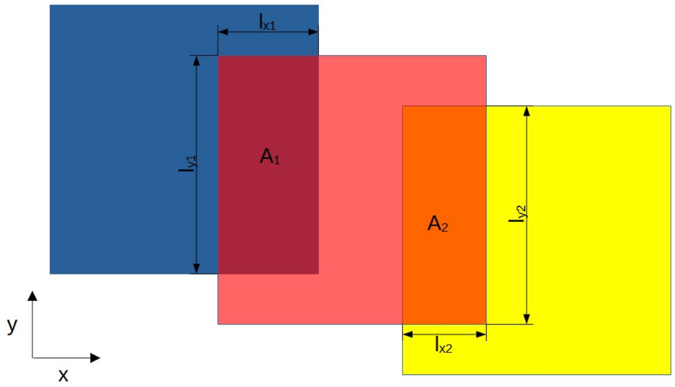

Figure 2.7: Common covered length and area in the $x$ and $y$ directions. Blue: ground electrode, red: stage, yellow: charged electrode.

$$C_1 = \frac{A_{stage,ground}\epsilon}{z} = \frac{(l_{x1}l_{y1})\epsilon}{z} \tag{2.17}$$

$$C_2 = \frac{A_{stage,source}\epsilon}{z} = \frac{(l_{x2}l_{y2})\epsilon}{z} \tag{2.18}$$

Further substituting eq. 2.18 and eq. 2.17 into eq. 2.16 results in eq. 2.19.

$$E' = -\frac{U^2_{source}\epsilon_0 l_{x1}l_{y1}l_{x2}l_{y2}}{2z(l_{x1}l_{y1} + l_{x2}l_{y2})} \tag{2.19}$$

Solving these derivatives leads to the following expressions for the force in each direction:

$$\vec{F} = -\nabla * E' = \begin{pmatrix} -dE'/dx \\ -dE'/dy \\ -dE'/dz \end{pmatrix} \tag{2.20}$$

Solving this vector gives the following universal force equations:

$$F_x = \frac{U^2_{source}\epsilon_0}{2z} * \frac{A_1^2\frac{dA_2}{dx} + A_2^2\frac{dA_1}{dx}}{(A_1 + A_2)^2} \tag{2.21}$$

$$F_y = \frac{U^2_{source}\epsilon_0}{2z} * \frac{A_1^2\frac{dA_2}{dy} + A_2^2\frac{dA_1}{dy}}{(A_1 + A_2)^2} \tag{2.22}$$

$$F_z = -\frac{U^2_{source}\epsilon_0}{z^2} * \frac{A_1A_2}{(A_1 + A_2)} \tag{2.23}$$

### 2.2.2. Electrode Shape

Since the use of electrostatic force of a stage is novel, there is limited prior work directly related to it. However, three references from the literature served as inspiration for the electrode design:

- **Jin et al. (1998)** [26]: As shown in Figure 1.1, a 1D linear motion is achieved by placing multiple rectangular electrodes adjacent to each other. The stage is locally charged and pulled toward the next electrode via controlled switching.
- **Keskekler et al. (2018)** [23]: Figure 1.6 illustrates a design where the stage is pulled toward a charged and grounded electrode pair for repositioning.
- **Karbache et al. (2024)** [27]: In Figure 1.7b, movement is achieved using only the charged electrode. A central grounded electrode serves as a return path for the stage.

# 3

# Design and Methodology

This chapter discusses the design decisions that led to the final system. It starts with a brief overview of each component, followed by detailed explanations. First, the magnetic array design is explored, then the electrode design, and finally the stage design. The chapter concludes by describing how all these elements come together in the final setup.

## 3.1. Methodology

The initial design was based on background theory and the literature review. Subsequent designs were developed through trial and error to identify new problems, which were then solved or bypassed using gained insights. To maximize efficiency, individual components were tested in parallel. These separate tests ultimately led to the final design, as discussed in Section 3.6.

## 3.2. Fundamental Setup

To achieve long-range motion, three key components are required: a magnetic array, a set of electrodes, and a diamagnetic plate. The magnetic array provides levitation and defines the stable levitation points. The use of a printed circuit board (PCB) enables precise fabrication of electrodes for electrostatic control. The diamagnetic plate functions as a stage, designed to interact with both diamagnetic and electrostatic forces.

## 3.3. Designing Permanent Magnet Array

To achieve levitation, as discussed in section 2.1, the derivative of the magnetic flux density squared must be greater than zero. In simpler terms, the magnetic flux density must increase in all directions. Different magnet arrays restrict different types of motion, some are better suited for rotation, others for translation. Arrays with local minima inhibit all motion to varying degrees, while arrays without minima allow movement in at least one direction. Various configurations of magnet arrays and pyrolytic graphite enable different characteristic movements, which could provide valuable insights.

### Checkerboard Magnet Array

The checkerboard array, as seen in Section 2.1.3, was tested using both 10 mm and 5 mm square magnets. Both configurations proved stable, but the array was ultimately not used. With 10 mm magnets, the local minima were too steep; with 5 mm magnets, the levitation height was too low. Additionally, the array induced unwanted movement in the y-direction. The magnet array using smaller magnets can be seen in Figure 3.1a.

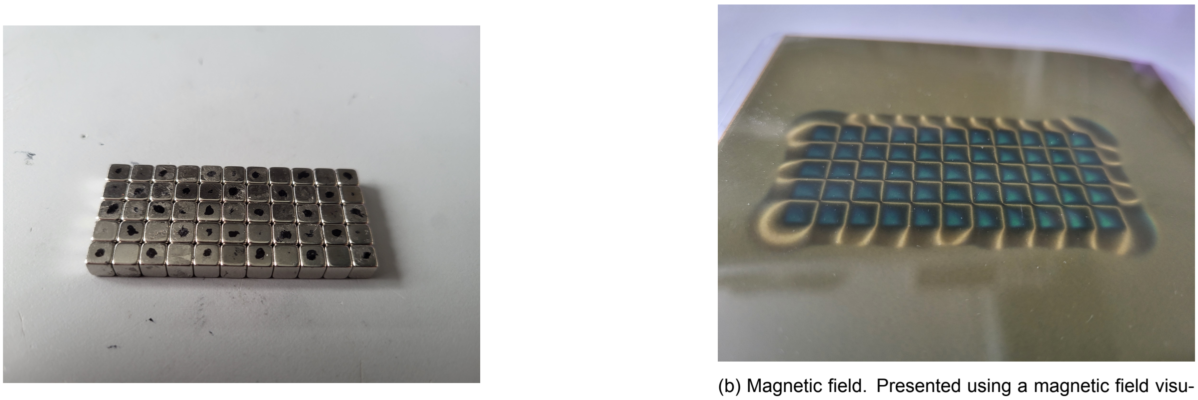

(a) Physical top view.

(b) Magnetic field. Presented using a magnetic field visualization sheet.

Figure 3.1: Experimental checkerboard magnet array and its magnetic field.

**3 Long Magnet Array**

This array, as discussed in Section 2.1.3, performs best when equipped with ”stopper magnets” at both ends. These increase the steepness of the local minima slightly making the setup process easier. A drawback is that stopper magnets limit the potential to extend the array. Without them, the array only has one very small local minimum and on both ends very steep magnetic field leading to the stage falling of the array, or if the array is prolonged by another three magnets a very steep local minima. (when the magnet array is made longer the new three magnets need to be turned upside down to form an array otherwise the twee 3 magnet arrays do not combine).

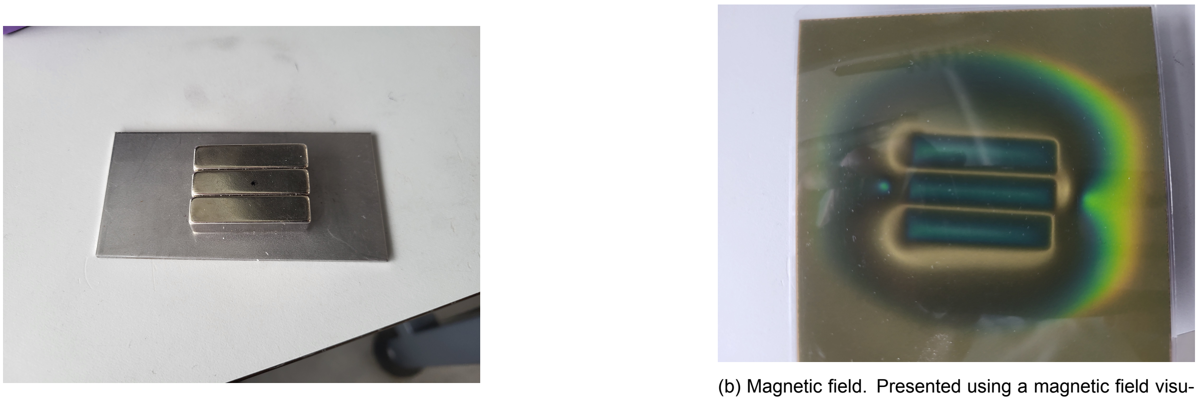

(a) Physical top view.

(b) Magnetic field. Presented using a magnetic field visualization sheet.

Figure 3.2: Experimental 3 long magnet array and its magnetic field.

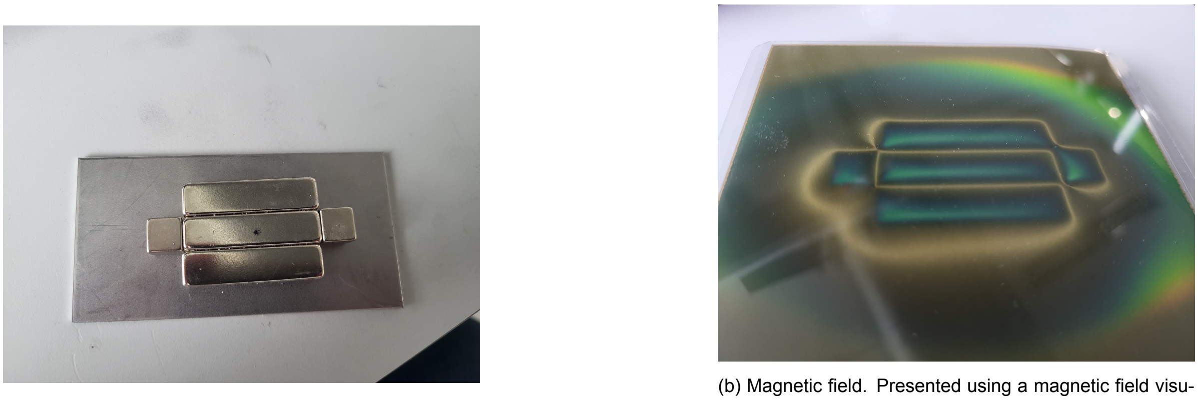

(a) Physical top view.

(b) Magnetic field. Presented using a magnetic field visualization sheet.

Figure 3.3: Experimental 3 long magnet array with stopper magnets and its magnetic field.

### Brick Magnet Array

The brick array consists of multiple long magnets arranged similarly to the 3-magnet array. The top and bottom magnets are offset halfway from the center, and this pattern is repeated. Since this setup connects north to north and south to south poles, a magnetic base is required, in this case, a 2 mm iron plate. While this configuration showed potential due to its repeatability, the local minimum created by the center magnet was too low to provide sufficient levitation force. This suggests that the middle magnet is the dominant contributor to the levitation height.

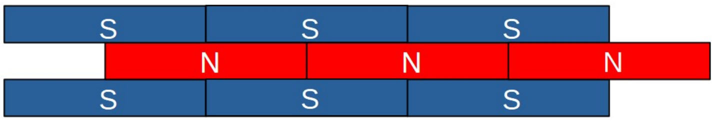

Figure 3.4: Top view of brick magnet array.

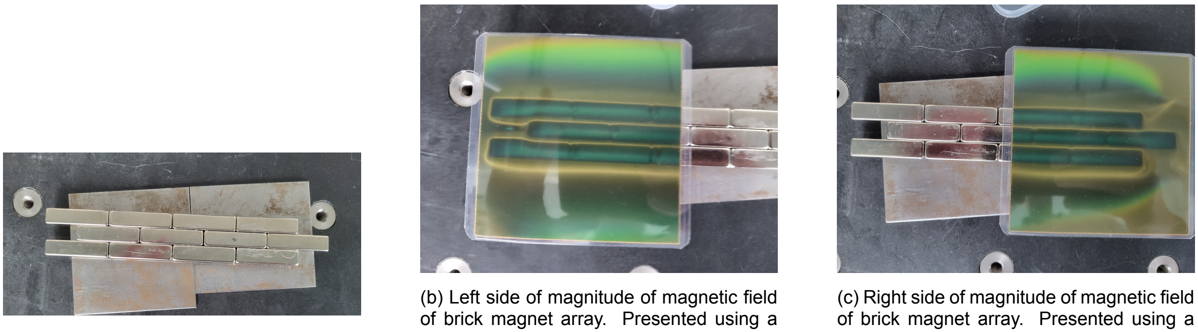

(a) physical top view of brick magnet array.

(b) Left side of magnitude of magnetic field of brick magnet array. Presented using a magnetic field visualization sheet.

(c) Right side of magnitude of magnetic field of brick magnet array. Presented using a magnetic field visualization sheet.

Figure 3.5: Three top views of checkerboard magnet array.

### Railroad Magnet Array

Following Section 2.1.3, this array was first constructed using using a 10×10×40 mm magnet and 5×5×5 mm magnets, first without steel as seen in Figure 3.6a and then with steel as seen in Figure 3.7a. Two layers of small magnets were used to raise their surface to the level of the larger central magnet. Without this extra layer, the small magnets would be attracted to the center of the larger magnet.

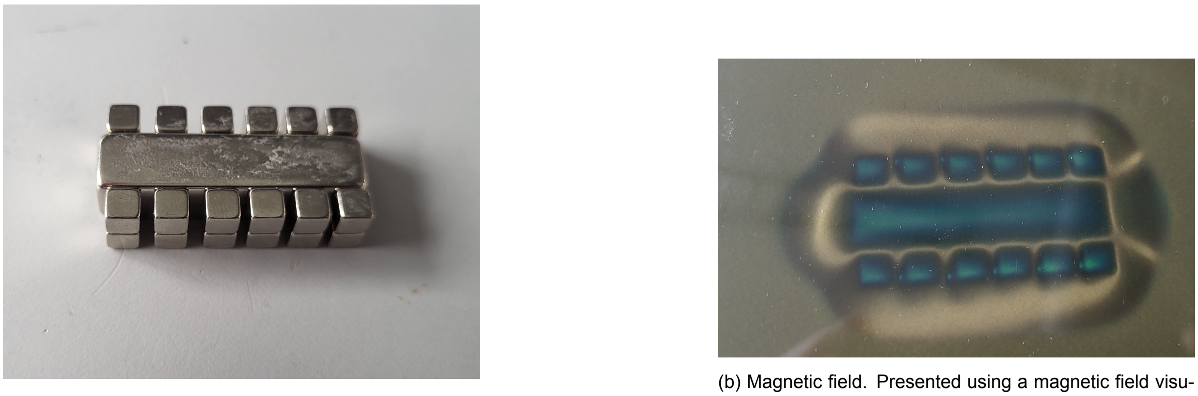

(a) Physical top view.

(b) Magnetic field. Presented using a magnetic field visualization sheet.

Figure 3.6: Experimental railroad array without steel floor and its magnetic field.

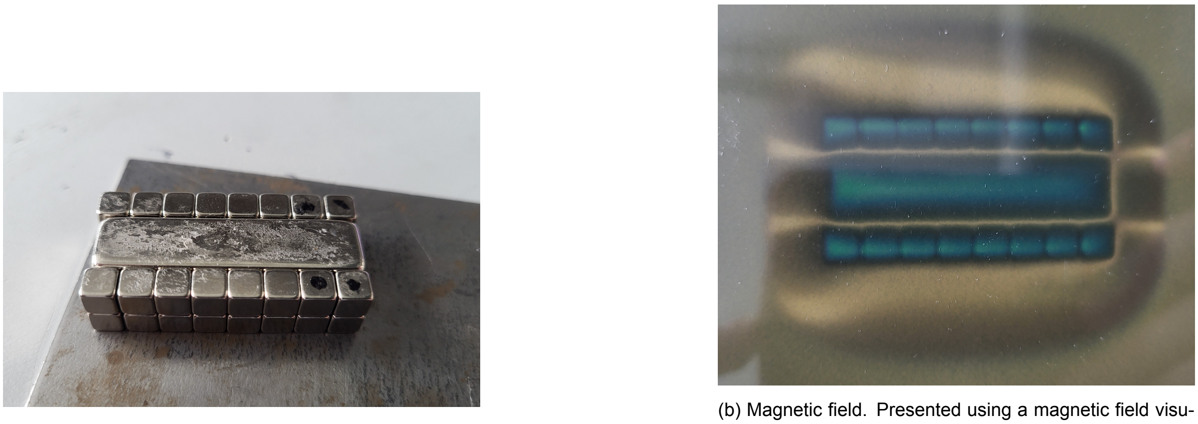

(a) Physical top view.

(b) Magnetic field. Presented using a magnetic field visualization sheet.

Figure 3.7: Experimental railroad array with steel floor and its magnetic field.

To improve this array, it was finally constructed using a long 10×10×80 mm magnet, combined with either small (5×5×5 mm) or large (10×10×10 mm) square magnets. This magnet array is shown in Figure 3.8. Testing showed that the smaller magnets did not generate sufficient force to create multiple local minima and were therefore not pursued further. The larger magnets, however, successfully created multiple local minima, separated by relatively shallow saddle points. During testing, the use of high voltage caused short circuits. To prevent this, isolation tape was applied, as shown in Figure 3.8b. Tape was only placed on parts where no levitation occurred. If sufficiently strong tape is used, the iron plate becomes unnecessary for the array.

(a) Without isolation tape.

(b) With isolation tape.

Figure 3.8: The railroad magnet array with the longer middle magnets and larger side magnets.

## 3.4. Designing Electrode Setup

As previously shown, the electrostatic force is greatest when there is a large change in surface area. However, this is limited by the electrostatic field generated by smaller electrode surfaces.

### 3.4.1. Phases

To achieve movement beyond the size of a single stage, multiple phases must be incorporated into the system. A two-phase system using square electrodes does not work when transitioning from one static equilibrium to the next, as illustrated in Figure 3.9.

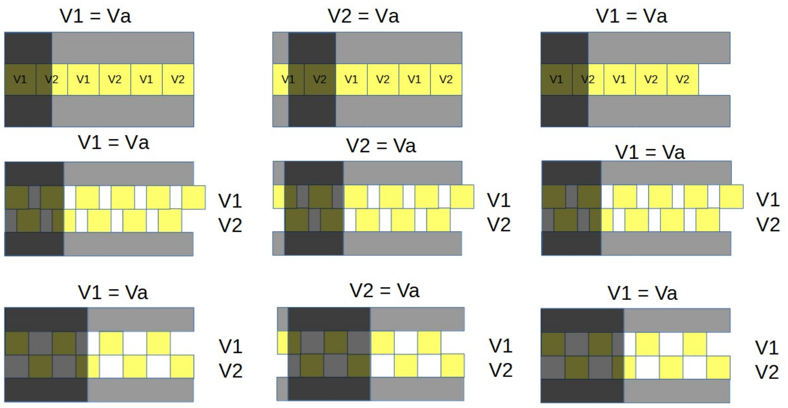

Figure 3.9: Three configurations of two-phase systems in equilibrium. The electrodes are shown in yellow, insulation in gray, and the stage in transparent black.

By introducing a third phase, backward pulling of the stage is prevented. As the stage will move to the charged electrode closest to it. This configuration is shown in Figure 3.10.

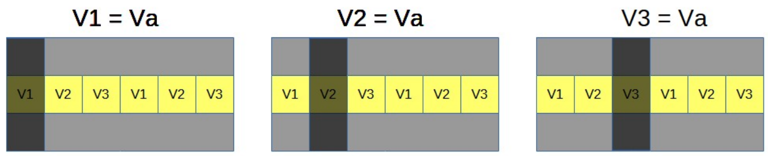

Figure 3.10: Three-phase configurations. The electrodes are shown in yellow, insulation in gray, and the stage in transparent black.

By grounding the uncharged electrodes, the top and bottom parts of the setup can be removed. However, this requires the stage to overlap with four electrodes. Insulation must be added between all electrodes to prevent short circuits. Furthermore, to avoid charge leakage to the stage, as observed in [23], [27], insulation should also be applied on top of the electrodes. These modifications result in the configuration shown in Figures 3.11a and 3.11b.

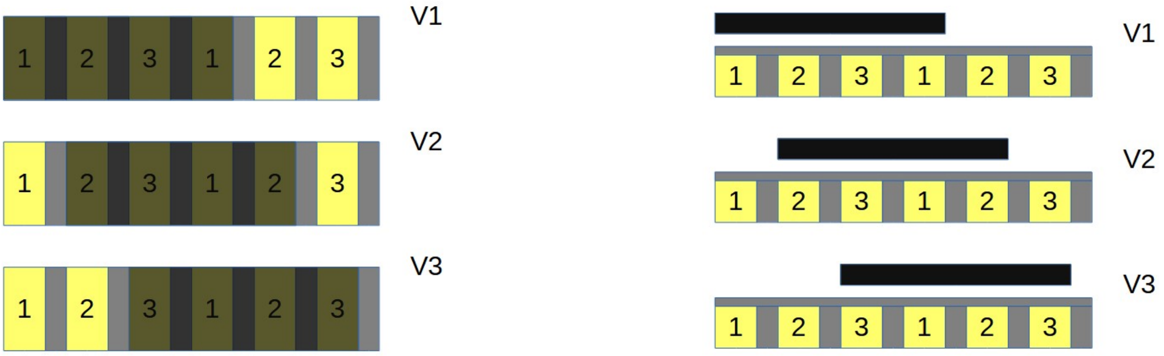

(a) Top view of the planned electrode setup.

(b) Side view of the planned electrode setup.

Figure 3.11: New four-phase configurations. The electrodes are shown in yellow, insulation in gray, and the stage in transparent black.

### 3.4.2. Shape

To design a suitable electrode layout, the following requirements must be met:

1. The pattern must be repeatable to enable movement beyond a single electrode set.
2. The pattern must not introduce y-direction movement.
3. Electrodes must not touch; otherwise, they would act as a single electrode.

These requirements led to the following three designs:

#### 4 phase Rectangle Design

As discussed earlier, a static determined controllable electrode setup requires the stage to cover at least four rectangles. The maximum change in surface area occurs when the electrodes are aligned and squares. By maximizing the electrode size, a stronger electrostatic field is achieved. This increased force proved necessary when using thinner PCBs, as discussed later in this section. This PCB can be seen in Figure 3.12

(a) Picture of the PCB.

(b) Schematic of PCB in easyEDA, the backside is highlighted in blue.

Figure 3.12: The 4 phase PCB.

#### Smaller 10 phase Rectangle Design

For finer control, smaller electrodes can be used. Although this reduces the electrostatic field strength, it can be compensated by increasing the applied voltage. For static determined control, the number of electrodes should follow the formula $3n + 1 =$ number of electrodes. Considering PCB manufacturing constraints, $n = 3$ was chosen, resulting in a design where the stage must cover 10 electrodes, as shown in Figure 3.13. This design was modeled and tested, but the added control proved unnecessary for this research, since the main focus was on extending the movement range. The more uniform effect is best observed in simulations using the electrostatic COMSOL model (see Section 4.4), with results shown in Figure 3.14. These findings were verified by measuring the maximum movement range, which will be discussed in Section 8.3.

(a) Picture of the PCB.

(b) Schematic of PCB in easyEDA, the backside is highlighted in blue.

Figure 3.13: The 10 phase PCB.

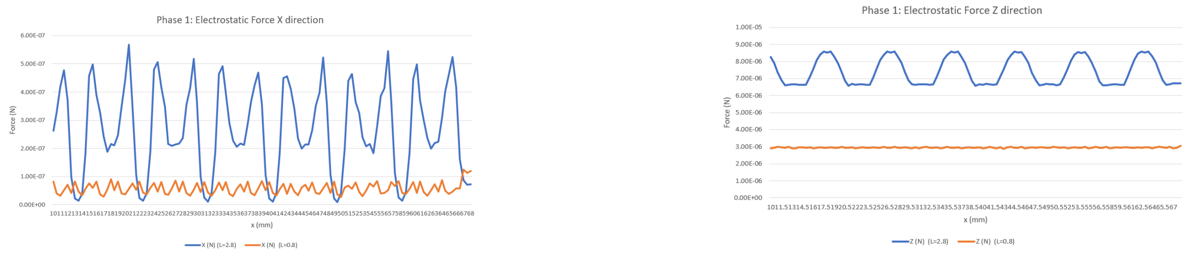

(a) Electrostatic force in x-direction (phase 1).

(b) Electrostatic force in z-direction (phase 1).

Figure 3.14: Comparison of electrostatic force in phase 1 for different electrode sizes. Blue: 2.8 mm, Orange: 0.8 mm.

### Side-Rail Design

By abandoning the four-phase concept and considering the design as shown in Figure 3.10, a design was developed in which the grounded area remains constant. The middle electrodes are switched, while two long grounded electrodes run along the sides. This PCB design can be seen in Figure 3.15. This allows the electrodes to be longer, though narrower, resulting in a slightly weaker but more uniform electrostatic field. This configuration was not finally used, as it neither provided the required force nor offered additional control. However, it has the potential to be more stable compared to the other two designs. This was also verified as seen in Section 8.3.

(a) Picture of the PCB.

(b) Schematic of PCB in easyEDA, the backside is highlighted in blue.

Figure 3.15: The side-Rail PCB.

## 3.4.3. Thickness of PCB

Since PCBs were used, thickness options were discrete. Initially, a 0.6 mm FR-4 PCB was chosen, as it is a standard thin and affordable option, easy to attach to magnets. However, levitation occurs around 1 mm, leaving only 0.4 mm of levitation height. To gain levitation height from the electrode the PCB would need to be thinner. The thinnest option is a flex-PCB, available at 0.11 mm thickness. However, as the name suggests, flex-PCBs are not rigid and cannot be mounted with screws like FR-4 boards. Therefore, they require adhesive for assembly to the magnet array.

# 3.5. Designing HOPG Stage

The design of the HOPG stage allows manipulation of both the experienced diamagnetic and electrostatic forces.

### Impact of Diamagnetism on Stage Behavior

As shown previously in Section 2.1.2, the diamagnetic force is expressed as a volume integral. The first observation is that if the magnetic field $\vec{B} \cdot \frac{d\vec{B}}{dz}$ is uniform, increasing the thickness of the plate increases both the diamagnetic and gravitational forces. Consequently, as long as the magnetic field gradient is consistent, the average levitation height remains unchanged, while the absolute levitation height decreases by approximately half the added thickness.

The second observation is that the magnetic field varies in the $x$ and $y$ directions. By modifying the shape of the stage, one can expose it to specific parts of the field. For example, decreasing material in the middle shifts the influence toward the side magnets and away from the central magnets, altering the distribution of the diamagnetic force.

**Impact of Electrostatic Forces on Stage Dynamics**

As discussed in Section 2.2.1, the electrostatic force arises from changes in the overlapping surface area between charged and grounded electrodes.

Two key design constraints must be considered:

For steady-state control, the stage must cover four electrodes in the $x$ direction.

To prevent undesired rotation or translation in the $y$ direction, the stage must be symmetric.

### 3.5.1. Stage Designs

The considerations above lead to the following stage designs:

(a) Square Plate.

(b) H Plate.

(c) O Plate.

Figure 3.16: Different stage designs: Square, H, and O plates.

**Square Plate**

A basic and commonly used design, except when integrated into a composite stage, as seen in [4], [10]. This design is a simple square plate of uniform thickness. Its primary advantages are:

- Ease of modeling: The geometry is simple and straightforward to simulate.
- Ease of manufacturing: The shape requires minimal cutting, typically just four straight cuts.

**H Plate**

The H-shaped stage is formed by cutting out square sections from the top and bottom of a square plate.

**Advantages:**

- Reduces volume in the middle, thereby decreasing the diamagnetic force contributed by the central magnet.
- Improves the ability of the stage to move over local minima caused by the middle magnet.
- Enhances stability in the $y$ direction, since lateral movement would require crossing over the central magnet.

**Disadvantages:**

- The central magnet significantly contributes to levitation; reducing its influence also reduces overall levitation height.
- The removed middle section does not contribute to the double capacitor effect, thereby reducing the electrostatic force.

Through testing it was seen that the disadvantages did not outweigh the advantages so this stage was not further used.

**O Plate**
The O-shaped stage is a square plate with a hole in the center.

**Advantages:**

- Capable of spanning a local maximum, provided two local minima exist on either side, which can create an extra-stable levitation point.
- Like the H-shape, removing material from the center reduces the influence of the middle magnet.

**Disadvantages:**

- Similar to the H-shape: lower levitation due to reduced central magnet influence, and weaker electrostatic force due to a smaller effective capacitor area.
- Additionally, it is less stable in rotation within the $x$-$y$ plane.

Through testing it was found that when a local minima is reached by one side this would create tilt which made this stage much more susceptible to the electrostatic force overcoming the diamagnetic force, this would in turn pull the whole stage against the PCB. Therefore, this stage was not used.

## 3.6. Final Design

This section outlines the final design choices based on the experimental results and theoretical considerations discussed previously.

### 3.6.1. Final Magnet Array

A key requirement for the magnet array is the ability to generate multiple local minima, which are essential for stable levitation and controlled movement. Among the configurations tested, the railroad magnet array best meets this requirement. The square magnets in this setup create multiple local minima, while the central long magnet provides the necessary levitation height. As such, the railroad array was selected for the final design.

### 3.6.2. Final PCB

Through simulation and experimental validation, it was determined that the side-rail design did not produce a stronger electrostatic force than the 4 phase rectangle design. Additionally, although the 10 phase rectangle design offered finer control, it required significantly higher voltage—beyond what was practical, considering the already high voltage requirements of the 4 phase rectangle design. Therefore, the 4 phase rectangle layout was selected for the final PCB.

During testing, it was observed that increasing the applied voltage enhanced the electrostatic force. However, this also increased the downward force, which in some cases exceeded the diamagnetic repulsion and caused the stage to be pulled into contact with the PCB. As can be seen in Section 2.2.1, the $z$ (eq. 2.23) and $x$ (eq. 2.21) components of the electrostatic force scale differently: both increase quadratically with voltage, but their dependence on levitation height differs, $F_z$ scales quadratically, while $F_x$ scales linearly. This asymmetry highlighted the need for a larger gap between the electrodes and the stage to preserve levitation. To achieve this, a flex-PCB with a thickness of only 0.1 mm was used, to maximize the lateral force and minimize the downwards force.

### 3.6.3. Final Stage

A simple square plate was chosen for the stage design. When used in combination with the thinner flex-PCB, the lateral ($x$-direction) component of the electrostatic force became more significant. To maximize this force, the change in overlapping surface area must be maximized during actuation. The square plate satisfies this condition most effectively, making it the optimal choice for the final stage design.

# 4

# Analytical Model and Finite Element Method Simulations

## 4.1. Analytical Magnetism Model

Using the analytical approach presented in [40], a model was developed to estimate the magnetic field and resulting diamagnetic forces for the final magnet array design. The implementation of this model is provided in Appendix A.

The model parameters were as follows:

- 3D grid: length $120$ mm, width $40$ mm, height $5$ mm, and spatial resolution $0.05$ mm, defining the region above the magnet array.
- Material properties: vacuum permeability $\mu_0 = 4\pi \times 10^{-7}$ H/m, magnetization $1.3 \times 10^6$ A/m, magnetic susceptibility $-40.9 \times 10^{-5}$.
- Stage: volume $12 \times 12 \times 0.5$ mm$^3$, positioned $1$ mm above the magnet array.
- Central magnet: length $80$ mm, thickness $10$ mm, height $10$ mm, centered in both $x$ and $y$, with the top surface magnetized as a north pole.
- Side magnets: length $10$ mm, width $10$ mm, height $10$ mm, magnetized so the top surface is a south pole. Their centers are offset $\pm 10.1$ mm in the $y$-direction. Along $x$, magnets are placed starting $35$ mm from the central magnet, spaced every $11$ mm, for a total of eight magnets on each side.

The resulting magnet array configuration is shown in Figure 4.1.

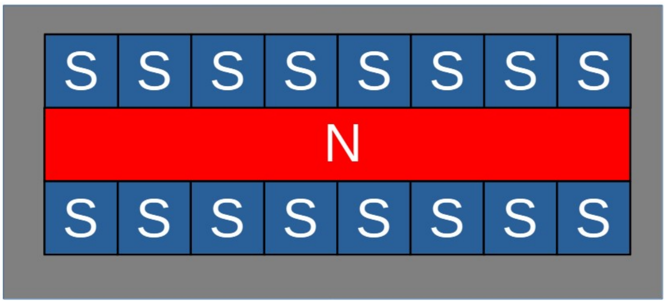

Figure 4.1: Modeled railroad magnet array.

The analytically computed magnetic field components are presented in Figure 4.2.

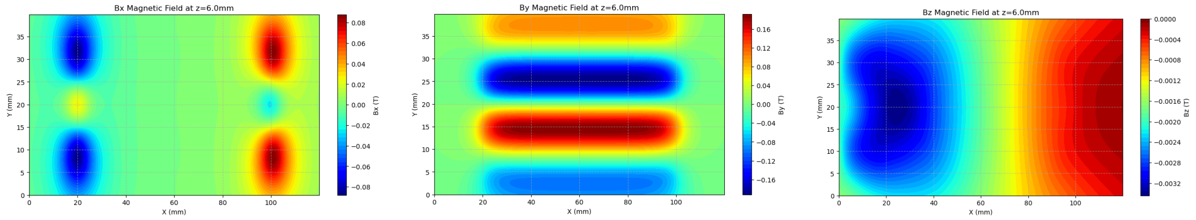

(a) $B_x$: $x$-component. (b) $B_y$: $y$-component. (c) $B_z$: $z$-component.

Figure 4.2: Components of the analytically calculated magnetic field.

The corresponding force field for the diamagnetic force, derived from equation 2.4, is shown in Figure 4.3.

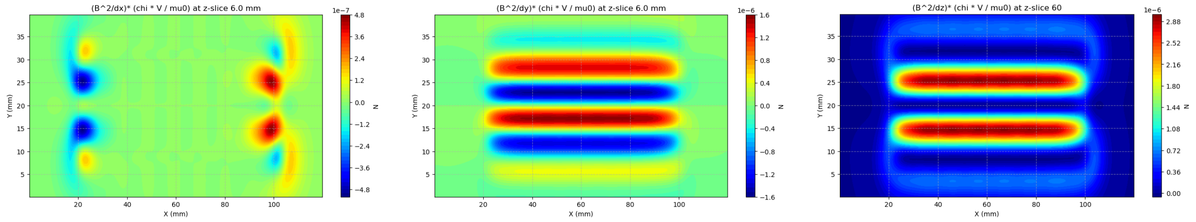

(a) $x$-direction force field. (b) $y$-direction force field. (c) $z$-direction force field.

Figure 4.3: Components of the analytically calculated diamagnetic force field $\nabla(B^2)$.

To estimate the net diamagnetic force on the stage, a discrete volume integral was performed over the stage geometry, yielding the total force in both $x$- and $z$-directions as a function of position.

Figure 4.4 shows the $z$-component of the diamagnetic force as the stage is displaced along the $x$-axis.

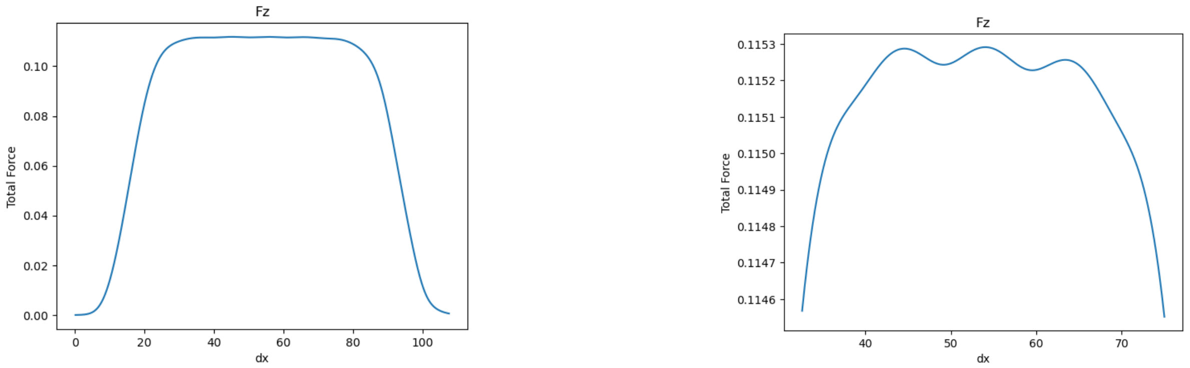

(a) Total $F_z$ on the stage. (b) Zoomed view, $x$ = 32–75 mm.

Figure 4.4: $z$-component of the diamagnetic force as the stage moves along $x$.

Similarly, the $x$-component of the diamagnetic force is shown in Figure 4.5.

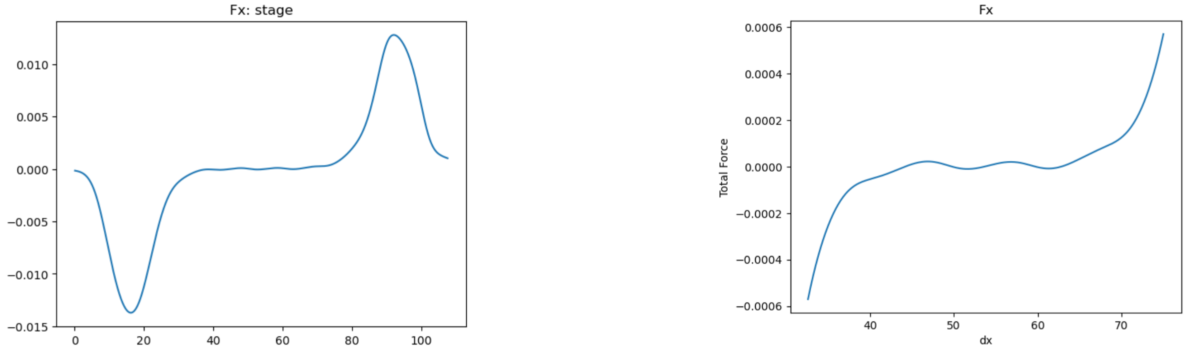

(a) Total $F_x$ on the stage.

(b) Zoomed view, $x = 32$–$75$ mm.

Figure 4.5: $x$-component of the diamagnetic force as the stage moves along $x$.

Both force components exhibit small local minima, consistent with the designed magnet array. In the z-component, these minima appear as valleys, while in the x-component they are indicated by the force being positive to the left of a point and negative to the right. The gravitational force on the stage was calculated to be approximately $1.24 \times 10^{-3}$ N, while the maximum diamagnetic lift force from the model was about $1.10 \times 10^{-3}$ N. The small difference is likely due to the idealized magnet shapes in the analytical model not fully matching the actual physical geometries.

## 4.2. Analytical Electrostatic Model

An analytical model was developed to estimate the electrostatic forces acting on a moving stage. This model is based on the equations presented in Section 2.2, which relate the overlap between the stage and the electrodes to the resulting electrostatic forces.

The model computes the overlapping areas between the stage and each electrode for every phase configuration. It then evaluates how these areas change as the stage moves, using this data to compute the resulting electrostatic forces in both the $x$- and $z$-directions. The model also identifies which electrode phase contributes most significantly to the total force at each position.

The following parameters were used to do the calculations: First the constants permittivity is defined as $8.85418781 88e - 12$ and eta as $1e - 9$, eta is used when to prevent divide by zero. Too calculate the area a mesh grid is defined as 2D with length 120 mm, width 20 mm and a resolution of 0.1 mm. The stage is defined as in the mesh grid as a 12 mm square. The electrodes are defined as 3 separate sets of electrodes all the same size of length of 2.8 mm width of 14 mm with a gap between these of 0.2 mm. The last two variables are the distance between the stage and the electrodes, here chosen as 0.5 mm and a activation of voltage of 1200 V.

The full implementation of the model is written in Python and included in Appendix B. The code calculates the overlapping areas, their spatial derivatives, and applies the force equations to provide position-dependent force estimates.

The overlapping area and its derivative with respect to position are shown in Figure 4.6, where the $x$-axis represents the stage position in the $x$-direction, and the $y$-axis shows the area and its rate of change.

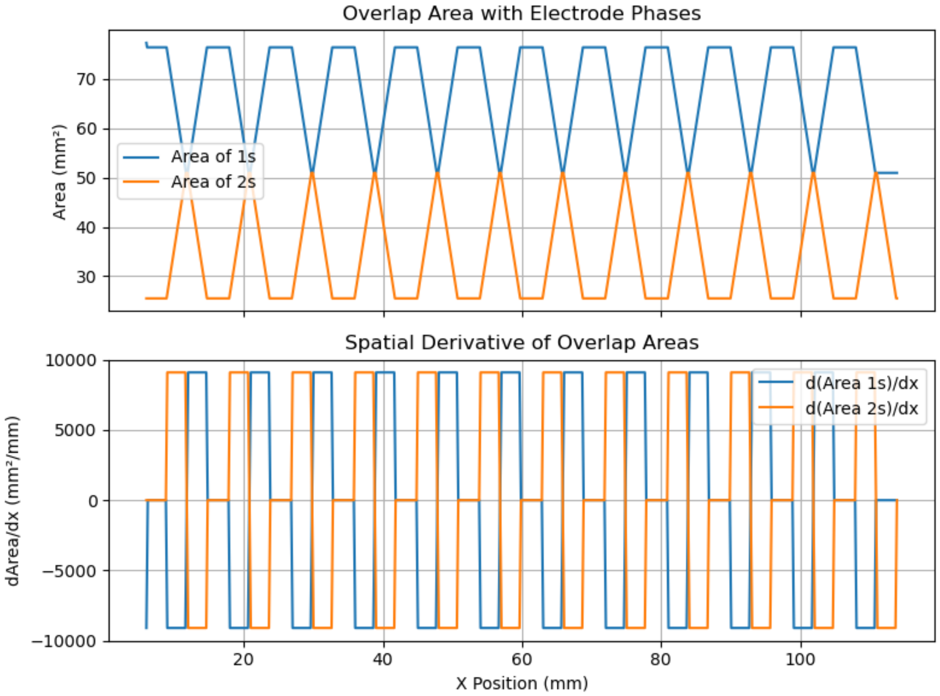

Figure 4.6: Overlap area and its spatial derivative between the stage and electrodes as a function of stage position.

Performing this calculation for each individual phase yields the electrostatic forces shown in Figure 4.7.

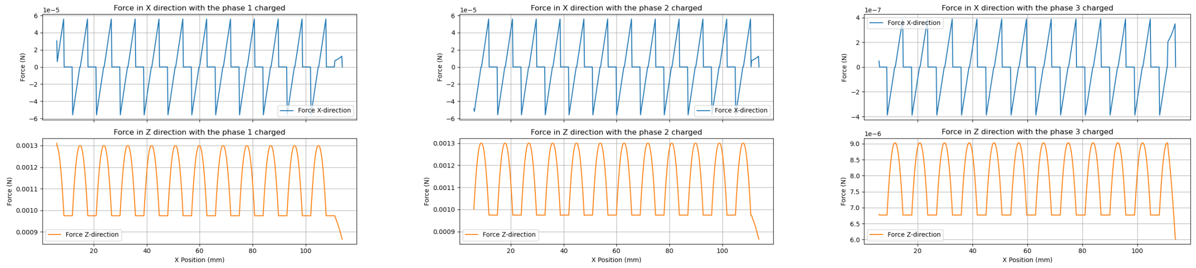

(a) Force from charging electrode 1.

(b) Force from charging electrode 2.

(c) Force from charging electrode 3.

Figure 4.7: Calculated electrostatic forces for each phase configuration.

In this analytical model, reducing electrode size does not significantly affect the computed magnitude of the electrostatic force. However, in practice, smaller electrodes produce weaker fields.

## 4.3. FEM Magnetism and Electrostatic

Finite element modeling (FEM) was carried out using COMSOL. Both diamagnetism and electrostatics were modeled in 3D. For electrostatics, the y-direction is not relevant, which would allow a 2D model. However, to simplify integration with the magnetic model, it was also implemented in 3D. These models were used in designing the magnet array and the PCB, where different parameters were varied to study their effects and guide design choices.

## 4.4. Electrostatic Model

The electrostatic simulation was initially performed in 2D. However, for the previously stated reason, the final model was developed in 3D.

**Physics Toolbox Electrostatic Model**
The Electrostatics interface from the AC/DC – Electric Field and Currents group was used.

**Geometry Electrostatic Model**
The following geometry was used:

- Stage: length 12 mm, width 12 mm, thickness 0.5 mm, positioned at the center of the y-axis and 0.5 mm above the electrodes.
- Electrodes: box with length 2.8 mm, width 14 mm, thickness 0.2 mm.
- Air domain: box with length 90 mm, width 28 mm, height 5.7 mm, including 2 mm above and below the system.

The electrodes were arranged in three 1D arrays spaced $3 \times 0.2 + 3 \times 2.8 = 9$ mm apart. To make selecting boundaries easier for these arrays, all phases and the stage are made their own ”domain” (to do this select under ’selection of resulting entities’ the cumulative selection function). The geometry is shown in Figure 4.8. The stage starts at the back of the electrodes and is displaced along $dx$.

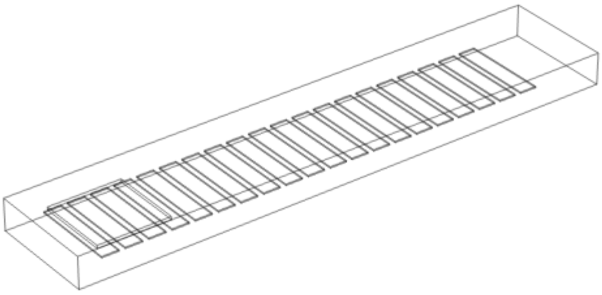

Figure 4.8: Geometry overview showing stage, electrodes, and air box.

**Materials Electrostatic Model**
Since electrostatics are primarily surface effects, the stage and electrodes were defined using the difference function. Air was modeled as a material with relative permittivity $\epsilon_r = 1$.

**Physics Electrostatic Model**
To define the electrostatic interactions, the **Electrostatics** interface was used. The primary feature is **Charge Conservation**, which enforces the equation:

$$\nabla \cdot \mathbf{D} = \rho_{\text{free}}$$

where $\mathbf{D}$ is the electric displacement field and $\rho_{\text{free}}$ is the free charge density.

**Boundary Conditions:**

- **Outer Boundaries:** Set to zero charge, represented by the condition:

  $$\mathbf{n} \cdot \mathbf{D} = 0$$

  where $\mathbf{n}$ is the unit normal vector to the boundary surface.
- **Initial Potential:** Set to 0 V across the entire domain.
- **Stage:** Defined as a **Floating Potential**, meaning it is an unconnected conductor that can acquire potential from non-floating features or behave like a terminal if connected to a circuit.
- **Electrodes:** Split into three groups (Phase 1, 2, 3), each assigned an electric potential of either 0 V or 200 V.

**Mesh and Study Electrostatic Model**
Mesh was generated using COMSOL, with finer elements defined by the Electrostatics interface. The resulting mesh can be seen in Figure 4.9

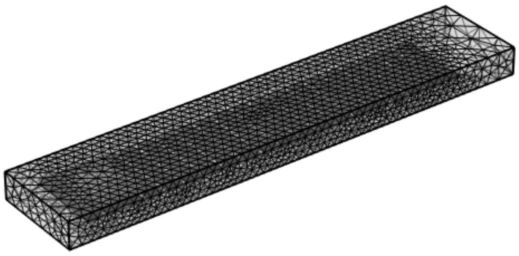

Figure 4.9: Mesh used in electrostatic FEM analysis in COMSOL.

A parametric study varied dx from 10 mm to 68 mm in steps of 0.5 mm to evaluate the stage positions.

**Results Electrostatic Model**
The electrostatic force was calculated using ([41]):

$$F = \int_A \frac{\sigma^2}{2\epsilon_0}\, dA \tag{4.1}$$

where

- $F$: total electrostatic force on the surface.
- $\sigma$: surface charge density.
- $\epsilon_0$: permittivity of free space.
- $A$: surface area.

Forces in the x and z directions were evaluated, as seen in Figure 4.10. Combining these results can help one to create a more smooth feedback controller, but that is not done in this paper. These results were used to design the PCB, only the final designs model is presented.

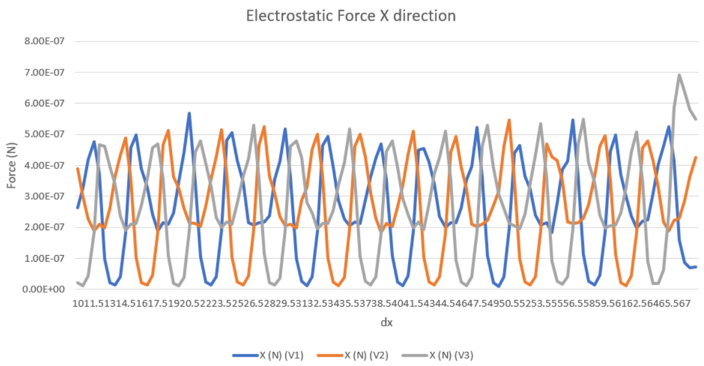

(a) Force in the x direction.

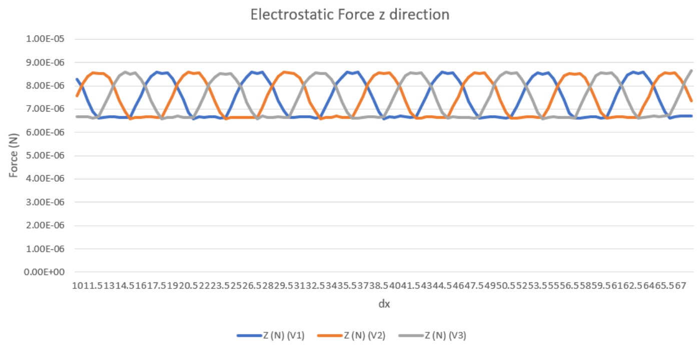

(b) Force in the z direction.

Figure 4.10: Results calculated in electrostatic FEM analysis in COMSOL.

(a) Electric potential XY-plane, with phase 1 active.

(b) Electric potential XZ-plane, with phase 1 active.

Figure 4.11: Results calculated in electrostatic FEM analysis in COMSOL.

## 4.5. Magnetic Model

As the magnetic field requires 3D, only a 3D model was made for the diamagnetism.

### Physics Toolbox Magnetic Model

For this the Magnetic Fields, No Currents physics interface from AC/DC - Magnetic Fields, No Currents group is used.

**Geometry Magnetic Model**

The geometry for the magnetic model was carefully constructed to represent the experimental setup. The air surrounding the magnets and the stage was modeled as a cube with dimensions 110 mm by 60 mm and a height of 40 mm. The middle magnet was represented as a cube measuring 80 mm by 10 mm by 10 mm, centered in the x and y directions. The z-position of the magnet was 10 mm. On either side of the middle magnet, eight smaller cube magnets of size 10 mm × 10 mm × 10 mm were placed in the y direction. All magnets were given a chamfer of 0.5 mm radius to better represent physical rounding. The stage was modeled as a small cube with dimensions 12 mm × 12 mm × 0.5 mm, positioned centrally along the y-axis and at the back in the x-axis, floating 0.6 mm above the top surface of the magnet array.

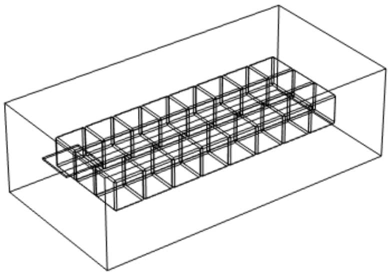

Figure 4.12: Geometry used in electrostatic FEM analysis in COMSOL.

**Materials Magnetic Model**

The materials used in the simulation were selected to approximate the physical properties of the real system. Air was modeled using the built-in material with relative permeability of 1. The permanent magnets were modeled using a built-in magnet material N50 (sintered NdFeB) also with relative permeability of 1. The stage was modeled as a blank material, assigning anisotropic relative permeability values to approximate pyrolytic graphite: $\mu_x = 85 \times 10^{-6}$ and $\mu_y = 450 \times 10^{-6}$.

**Physics Magnetic Model**

To define the magnetic interactions, the **Magnetic Fields, No Currents** interface was used. The primary feature is **Magnetic Flux Conservation**, which enforces the equation:

$$\nabla \cdot \mathbf{B} = 0$$

This equation ensures that the magnetic flux density $\mathbf{B}$ has zero divergence, indicating that magnetic field lines neither originate nor terminate but form continuous loops or extend to infinity.

The relationship between the magnetic flux density $\mathbf{B}$ and the magnetic field strength $\mathbf{H}$ is given by:

$$\mathbf{B} = \mu\mathbf{H}$$

where $\mu$ is the magnetic permeability of the material.

**Magnetic Insulation** boundary conditions were applied to all exterior boundaries, setting the tangential component of the magnetic potential to zero:

$$\mathbf{n} \times \mathbf{A} = 0$$

where $\mathbf{A}$ is the magnetic vector potential, and $\mathbf{n}$ is the unit normal vector to the boundary surface.

The initial magnetic field was set to zero across the entire domain:

$$\mathbf{H}(0) = 0$$

For the permanent magnets, the magnetization vector $\mathbf{M}$ was specified as 1.0265E6 (This gives a magnetic flux density of 1.3 T) along the z-axis:

$$\mathbf{M} = M_z \hat{z}$$

where $M_z$ is the magnitude of the magnetization along the z-axis, and $\hat{z}$ is the unit vector in the z-direction.

**Mesh and Study Magnetic Model**
The mesh was created in COMSOL, using fine elements defined by the physics interface to ensure accurate resolution of the magnetic field gradients. The resulting mesh can be seen in Figure 4.13

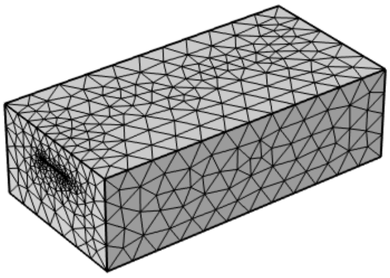

Figure 4.13: Mesh used in electrostatic FEM analysis in COMSOL.

A parametric study was done where dx was varied from 10 to 68 with steps of 0.5 mm to see the effects of the different location of the stage

**Results Magnetic Model**
The results are shown in Figures 4.14 and 4.15. It can be seen that the stage likely levitates slightly higher than what is shown here. However, this simulation was run as an exploration of the railroad array for the design and was not investigated further. Its primary purpose was to gain a better understanding of the magnetic field.

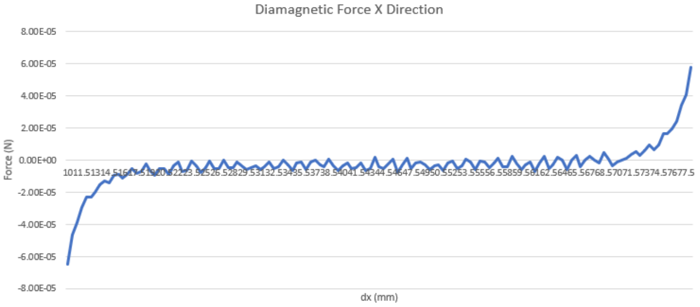

(a) Force in the x direction.

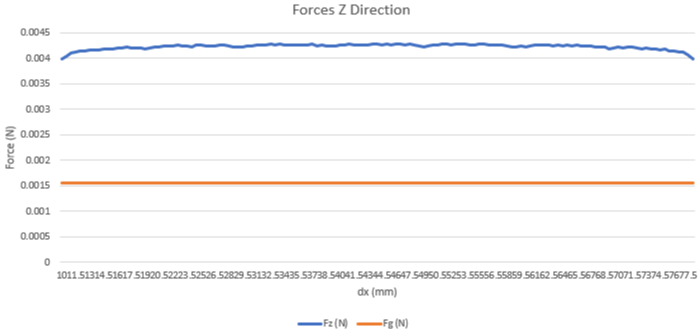

(b) Force in the z direction.

Figure 4.14: Results calculated in electrostatic FEM analysis in COMSOL.

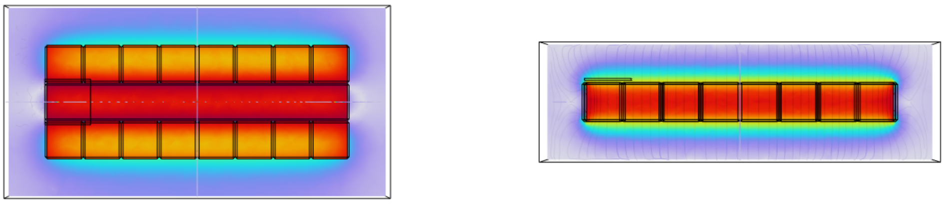

(a) Electric potential XY-plane, with phase 1 active.

(b) Electric potential XZ-plane, with phase 1 active.

Figure 4.15: Results calculated in electrostatic FEM analysis in COMSOL.

# 5

# Experimental Setup

This chapter outlines the configuration, instrumentation, and procedures used to conduct the experiments described in this work. It details the physical arrangement of the system, environmental control measures, and both low- and high-voltage driving setups. The aim is to provide sufficient technical detail to ensure reproducibility.

## 5.1. Mechanical Mounting and Environmental Isolation

The final system design, described in earlier chapters, was mounted on a tip–tilt stage to compensate for uneven supporting surfaces. Despite this adjustment, achieving perfect leveling remained difficult.

To reduce environmental disturbances, the setup was enclosed within a protective housing to shield it from airflow. Although not airtight and still susceptible to active disturbances such as direct air currents, the enclosure was effective in blocking passive airflow caused by drafts, ventilation, or people walking nearby.

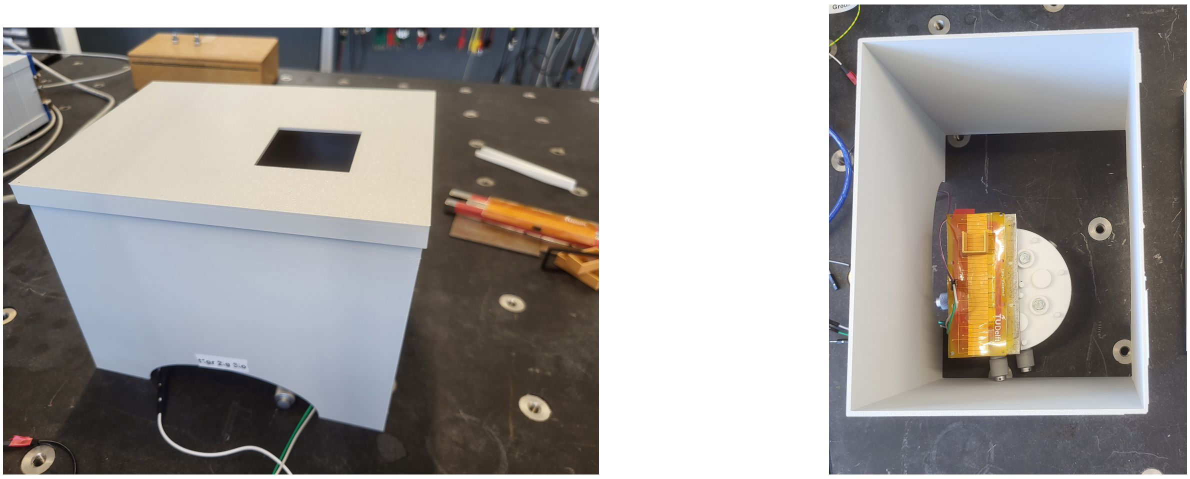

(a) Enclosure from side view.

(b) Enclosure open from top view.

## 5.2. Measurement

Accurate position tracking proved challenging due to the thin profile of the levitating stage. Which limits measurement techniques that can be used.

A smartphone camera (iPhone 11) was used to record the stage at a resolution of 1440x1080 pixels and a frame rate of 10 fps.

Captured footage was processed in MATLAB using the Computer Vision Toolbox. The Kanade–Lucas–Tomasi feature-tracking algorithm was used to extract positional data for further analysis (see Appendix C for the processing code).

## 5.3. Low-Voltage Driving Configuration

The low-voltage system combined:

- A Delta Elektronika E0300-0.1 power supply (0–300 V, 0–100 mA)
- A HV56264 Quad High-Voltage Amplifier Array EVB
- An Arduino Uno microcontroller
- An Adafruit MCP4728 I²C Quad DAC

This configuration (Figure 5.2) enabled millisecond-level timing control with voltage outputs from 0 to 250 V per phase independently from the other phases.

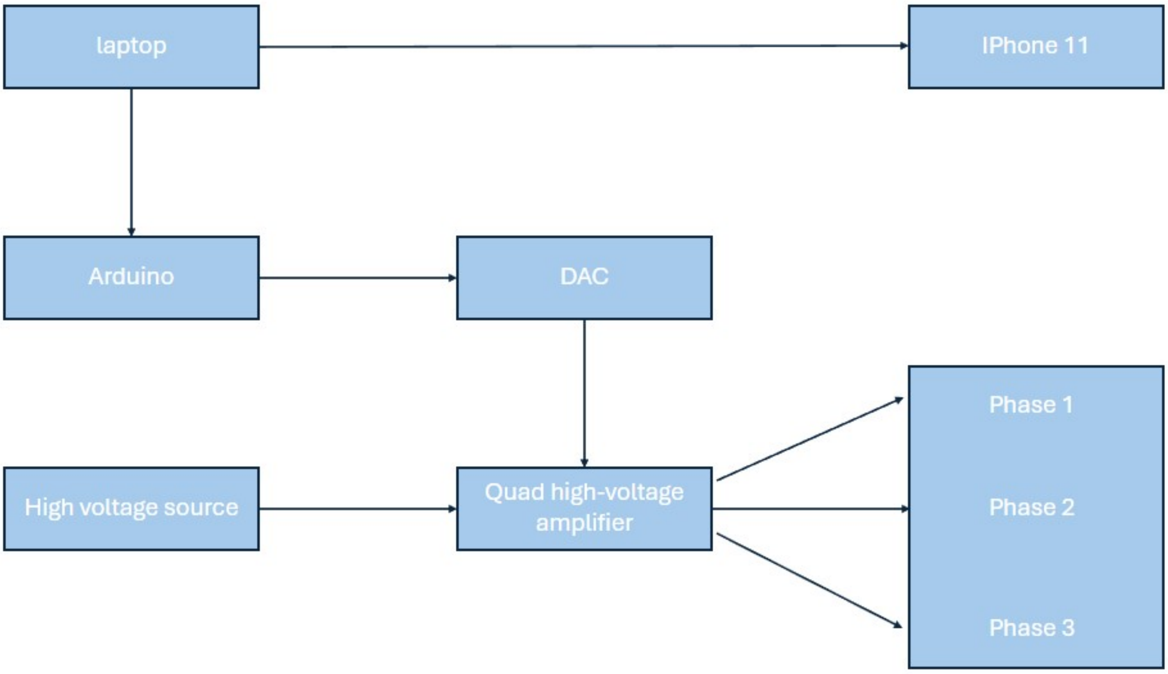

Figure 5.2: Cable connection schematic for the low-voltage configuration.

## 5.4. High Voltage Setup

High-voltage operation was achieved using a linear high-voltage controller (Senseg HV Driver C1). This allowed for single-phase actuation from 0 to 1200 V, while the remaining phases were grounded. This limited the tests to the response of a single phase, it did allow a much wider voltage range for analysis.

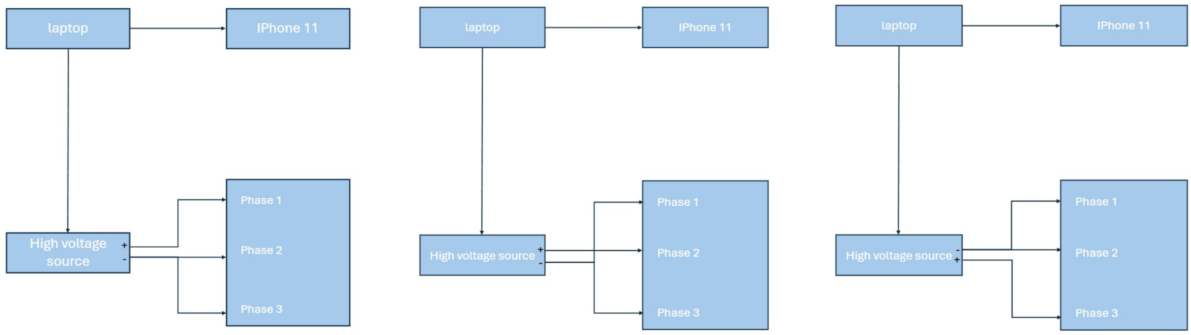

(a) Phase 1 electrodes connected.

(b) Phase 2 electrodes connected.

(c) Phase 3 electrodes connected.

Figure 5.3: Cable connection schematics for the high-voltage configurations.

# 6

# Results - System Characterization

This chapter explores the characteristics of the railroad array without considering the electrostatic force to better understand its inherent behavior. First, the system's response to external vibrations such as airflow is examined to assess its general sensitivity. Next, the stiffness and damping coefficient of the most prominent local minimum are determined, which help identify the system's resonance for maximizing its motion. Then, the effect of multiple local minima is analyzed to understand the behavior when the stage transitions between these minima. Finally, the impact of different stage angles on the stable equilibria is discussed.

## 6.1. External Vibrations and Noise

Due to the system's low stiffness and damping, introduced vibrations take a long time to dissipate, making it damp external noise poorly. As mentioned earlier, passive airflow was assumed to be blocked by shielding, leaving vibrations from the base of the setup as the primary disturbance. This was tested, as shown in Figure 6.1, since the camera is not perfectly aligned with the PCB, both the x and y positions are considered. Here, one pixel equals 0.082 mm; disturbances from passive airflow and walking near the system caused displacements up to 4 pixels (0.33 mm), while blowing on the device caused displacements up to 7 pixels (0.58 mm).

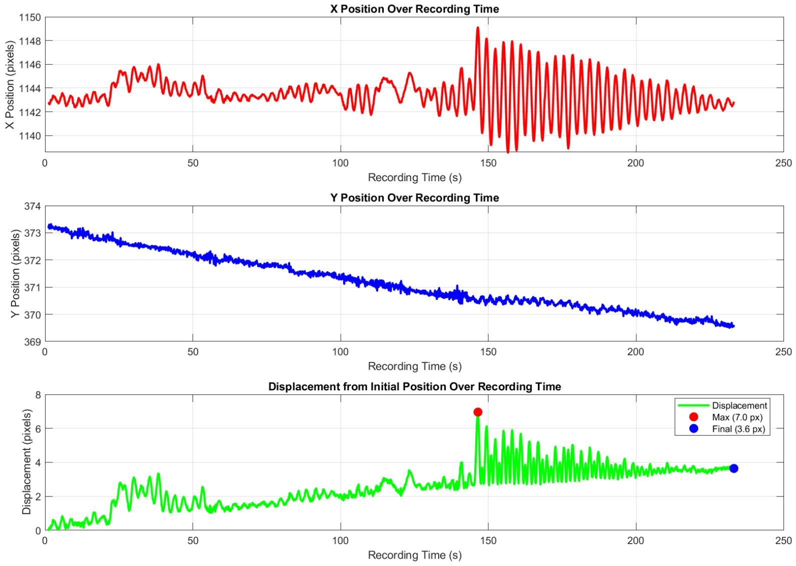

Figure 6.1: X and Y coordinates with displacement $\sqrt{X^2 + Y^2}$. One pixel equals 0.08 mm. From 0–50s: no activity; 50–120s: walking near the device; 150s–end: blowing on the shielded device.

## 6.2. Impulse Response

Short voltage pulses of varying amplitude were applied to the system to examine its eigenfrequency without the influence of electrostatic forces. This allowed characterization of the stage and magnetic field independently from electrostatics. An example is shown in Figure 6.2, which also illustrates the need to consider both x and y due to the camera being misaligned.

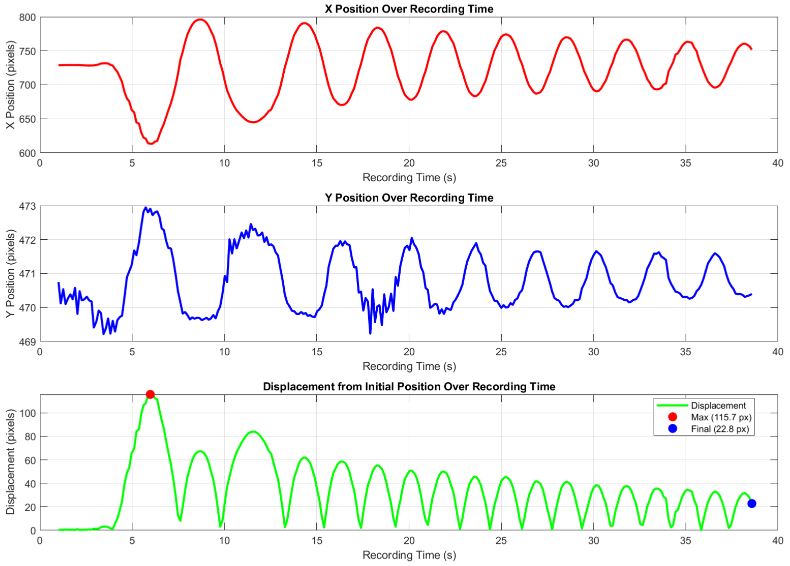

Figure 6.2: An example the data gained from the impulse experiment. In this case the experiment was 360 V impulse.

### 6.2.1. Initial Results of Impulse Test

The system is modeled as a damped mass-spring system, focusing on linear behavior as described in [42]. The general motion is given by Equation 6.1:

$$y = Ae^{-\frac{c}{2m}t}\cos(\omega t + \phi_0) \tag{6.1}$$

The variables in this equation are: $y$ for position, $A$ for amplitude, $c$ for the damping coefficient, $m$ for mass, $t$ for time, $\omega$ for frequency, and $\phi_0$ for phase shift. From this, the natural angular frequency is estimated by:

$$\omega_n = \frac{2\pi}{t_{\text{top2}} - t_{\text{top1}}} \tag{6.2}$$

In this equation, $t_{\text{top2}}, t_{\text{top1}}$ are the times of the first and second maxima, respectively. Using the calculated mass (Equation 6.4), the stiffness is found as:

$$k = m\omega_n^2 \tag{6.3}$$

$$m = 2200 \times 12 \times 10^{-3} \times 12 \times 10^{-3} \times 0.5 \times 10^{-3} = 1.5840 \times 10^{-4}\ \text{kg} \tag{6.4}$$

An envelope function was used to determine the damping coefficient by analyzing the peaks and troughs of the motion

$$y = Ae^{-\frac{c}{2m}t} \tag{6.5}$$

An example of this fitting can be seen in Figure 6.3. First, the data points are plotted (Figure 6.3a). Next, the envelope function is determined and plotted (Figure 6.3b). Finally, by plotting the dynamic function with the estimated values, the fitting can be observed (Figure 6.3c). From this example, the damping coefficient is estimated to be $1.0746 \times 10^{-5}$ N·s/m and the stiffness is estimated to be $5.9386 \times 10^{-4}$ N/m. In this case, an impulse of 600 V was applied to phase 2.

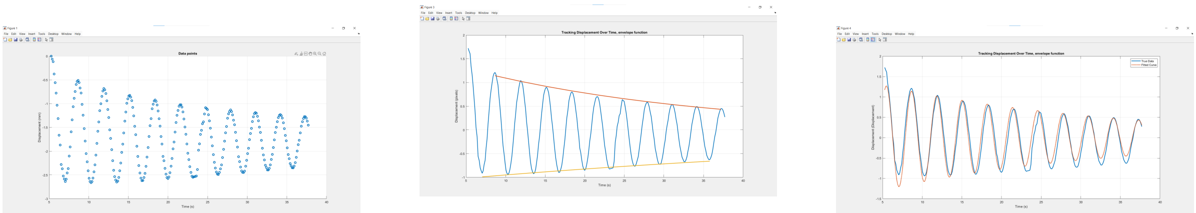

(a) Displacement data over time.

(b) Envelope functions fitted to upper and lower bounds.

(c) Dynamic model compared with data.

Figure 6.3: Fitting Equation 6.1 to impulse response with 600 V applied to phase 2.

To filter out nonlinear effects, the average and standard deviation of stiffness values were calculated. For a linear system, stiffness remains constant, so large deviations suggest nonlinear behavior. There are two main damping factors: air resistance and eddy currents[32]. As seen by the high standard deviation, the damping is not linear, which suggests that it is majorly damped by eddy currents, as this is dependent on the magnetic field.

This analysis yielded a stiffness of $6.37 \cdot 10^{-4}$ N/m with a standard deviation of $5.52 \cdot 10^{-5}$ N/m, and a damping coefficient of $8.37 \cdot 10^{-6}$ N·s/m with a standard deviation of $2.18 \cdot 10^{-6}$ N·s/m.

### 6.2.2. Multiple Local Minima

With sufficient initial motion, the stage's motion becomes nonlinear as it moves between multiple local minima. Fully characterizing this proved difficult, as not every local minimum behaves the same. Additionally, the orientation of the base, affected by the tilt angle of the stage and the floor, also influences the local minima.

#### Nonlinear Approach to Characterization of Multiple Local Minima

Further investigation of system dynamics using speed and acceleration is shown in Figure 6.4. Three behaviors can be recognized: First, oscillations occur over two local minima (the large initial oscillation, Figure 6.4a, Part A). Second, a short transition period follows, during which the motion slows down, visible as a peak where velocity decreases before accelerating again (Part B). Third, oscillations take place around a single minimum, visible as the smaller oscillations at the end (Part C).

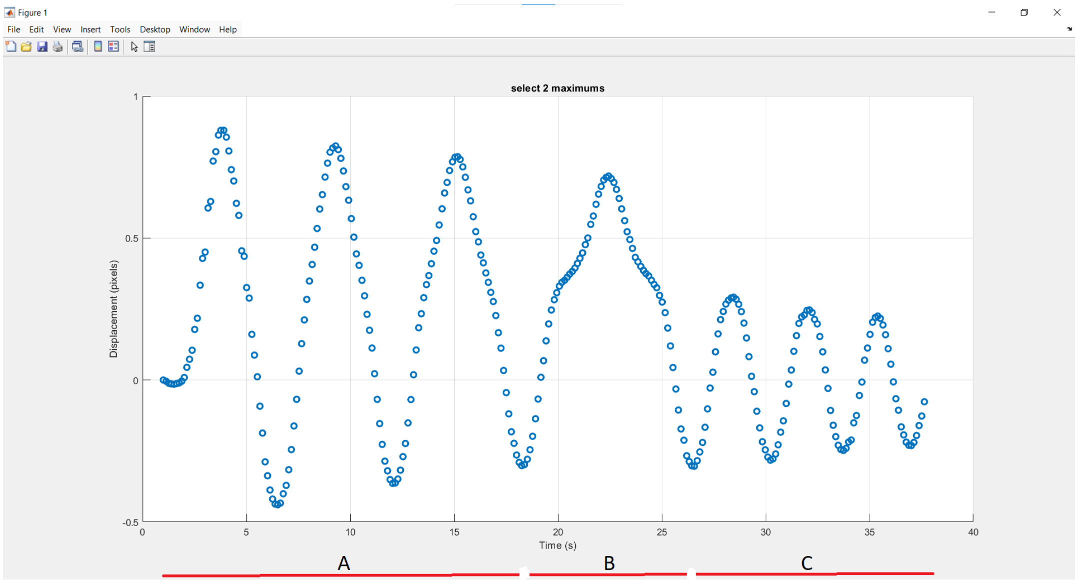

(a) Displacement over time. Three motion phases: oscillation between two minima (A), transition phase (B), and oscillation around a single minimum (C).

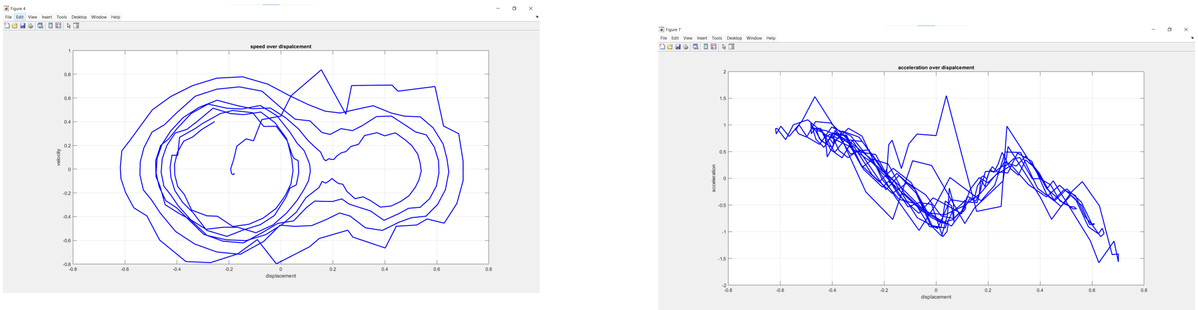

(b) A phase diagram. A plot showing how velocity changes with displacement.

(c) Plot showing how acceleration changes with displacement.

Figure 6.4: Here the impulse response is shown in three different ways.

In the Figures 6.4b and 6.4c. From left to right, the plots indicate a minimum, a saddle point, and another minimum in the co-energy. The acceleration curve (Figure 6.4c) resembles a cubic function of displacement, indicating a nonlinear spring typical of a Duffing oscillator. The velocity-displacement plot (Figure 6.4b) also supports this, showing two unequal minima (or attractors, per Duffing theory). The standard Duffing oscillator is described by:

$$\ddot{x} + \delta\dot{x} + \alpha x + \beta x^3 = \gamma\cos(\omega t) \tag{6.6}$$

Where:

- $\ddot{x}$: acceleration
- $\dot{x}$: velocity
- $\delta$: damping coefficient
- $\alpha$: linear stiffness coefficient
- $\beta$: nonlinear stiffness coefficient
- $\gamma\cos(\omega t)$: external periodic forcing

The observed behavior most closely resembles an inverted Duffing oscillator. This is characterized by an negative $\delta$ and an negative $\beta$. Using the following values :$\dot{x}_0 = 1$,$x_0 = 0,5$, $\delta = -0.1$, $\alpha = 0.4$, $\beta = -1.2$, $\gamma\cos(\omega t) = 0$

A Python model of a Duffing oscillator was developed; its motion closely matches the observed system behavior shown in Figure 6.5.

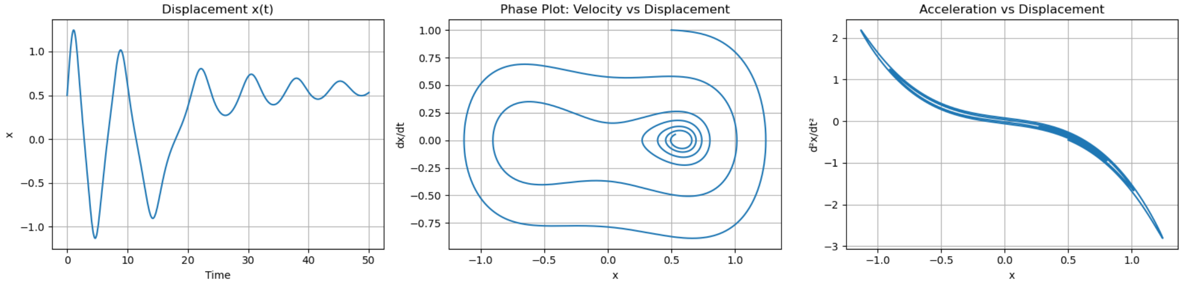

Figure 6.5: Python model of a Duffing oscillator showing displacement over time, velocity over displacement, and acceleration over displacement.

Due to the strong influence of tilt, further modeling was not performed, as it would apply only to this specific experimental setup.

## 6.3. Influence of Stage Tilt

As previously noted, the tilt of the stage strongly affects the system's characteristics. Slowly tilting the stage results in changes to the location and number of minima. Tilt compensates for lateral forces; tilting the stage to the right creates a local minimum on the left side and vice versa. A second local minimum appears when the stage is tilted further.

Figure 6.6: Three different stable equilibrium points with varying tilts. These correspond to the minimum (Figure 6.4a), saddle point (Figure 6.4b), and another minimum (Figure 6.4c) observed in the nonlinear dynamics analysis.

This behavior is believed to result from the energy function resembling Equation 6.7, plotted in Figure 6.7a. When the function is tilted, saddle points can become minima and vice versa. For illustration, the function tilted by 10 degrees is shown in Figure 6.7b, where the small minimum and saddle point on the right side both become minima.

$$y = -\frac{x^2}{50} + 0.5\cos(x) \tag{6.7}$$

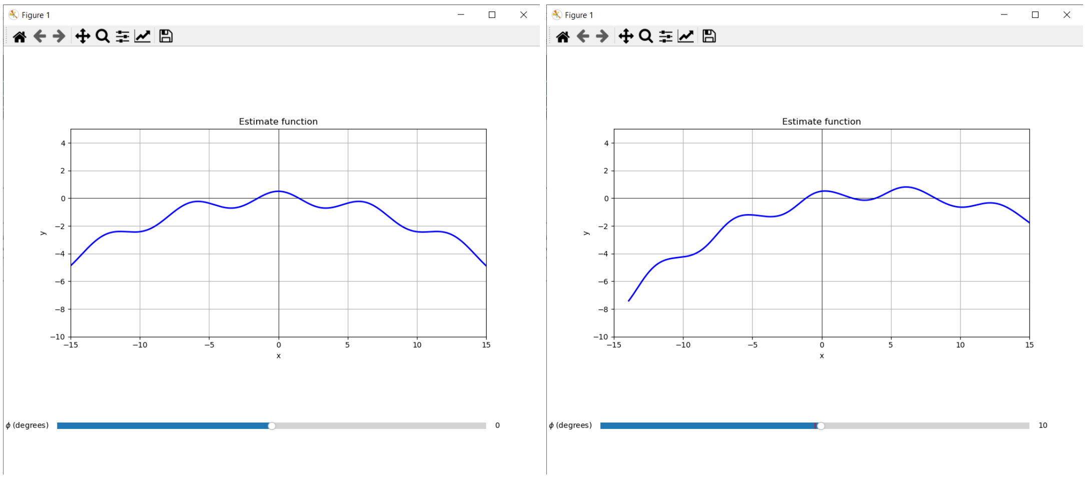

(a) Function from Equation 6.7 plotted with 0-degree tilt.

(b) Function from Equation 6.7 plotted with 10-degree tilt.

Figure 6.7: An example function showing an exaggerated illustration of how the force might vary depending on the stage position, with the X-axis representing the stage position and the Y-axis representing the force experienced by the stage.

# 7

# Results - Displacement Through Electrostatics

To investigate the movement capabilities of the system, several actuation strategies were tested. Low-voltage actuation was examined first, as this setup allows greater control over individual electrodes. In this regime, both steady-state movement and actuation using block functions at different frequencies were tested. A variant of this strategy was also explored in which a second phase was partially charged to create a more continuous pulling force.

High-voltage actuation was tested next, using the following approaches: 1. Instantaneous switching to full voltage. 2. A slow voltage ramp-up. 3. Single-phase actuation at different frequencies.

Finally, several dynamic behaviors were analyzed, including transitions between local minima of the co-energy for larger displacements.

## 7.1. Low Voltage

The low-voltage configuration allows for more precise and complex actuation modes. In these experiments, the voltage range was between 0 and 244 V.

### Low Voltage Steady State movement

The slow ramp-up method was first applied in the low-voltage setup. Results are shown in Figure 7.2, with the shared starting position given in Figure 7.1.

What can be seen here is that the movement never goes beyond external vibration levels. But here it can be seen that phase 1, effectively damps the vibrations and moves the stage very little. A smaller effect was observed for Phase 2, while Phase 3 showed no measurable influence.

This is consistent with the analytical electrostatic model (see Section 2.2), which shows that greater force is generated when electrode overlap and area change are maximal. Phase 1 has the highest overlap, resulting in the strongest effect. The next phase 2 electrode barely contacts the stage, producing less influence. The next phase 3 electrode has zero overlap, explaining its negligible effect, as seen the outside vibration only gets middle damped when the force was at its maximum.

Figure 7.1: Starting position of the low-voltage ramp-up experiments. Electrodes are labeled by phase.

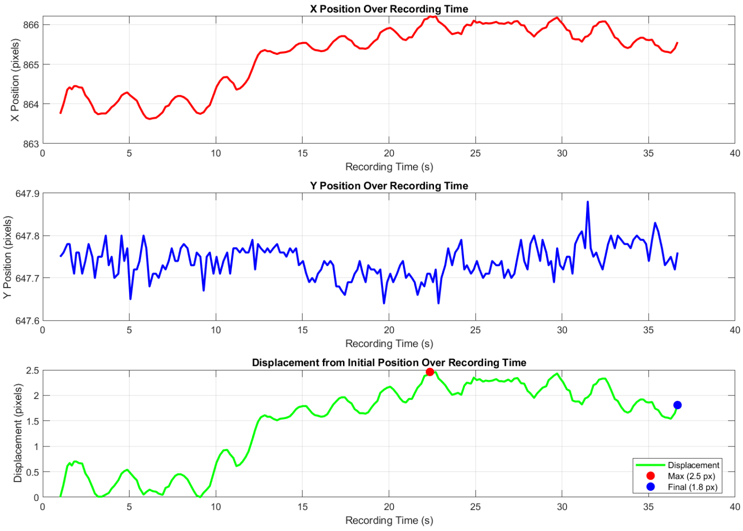

(a) Response to slow ramp-up in Phase 1.

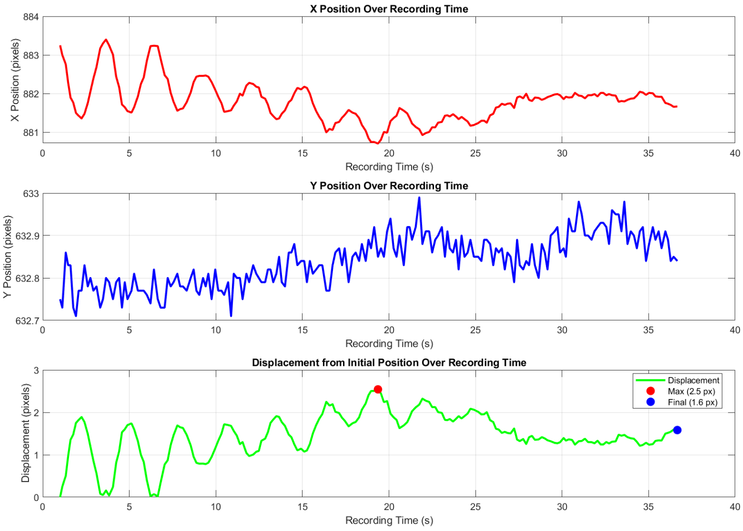

(b) Response to slow ramp-up in Phase 2.

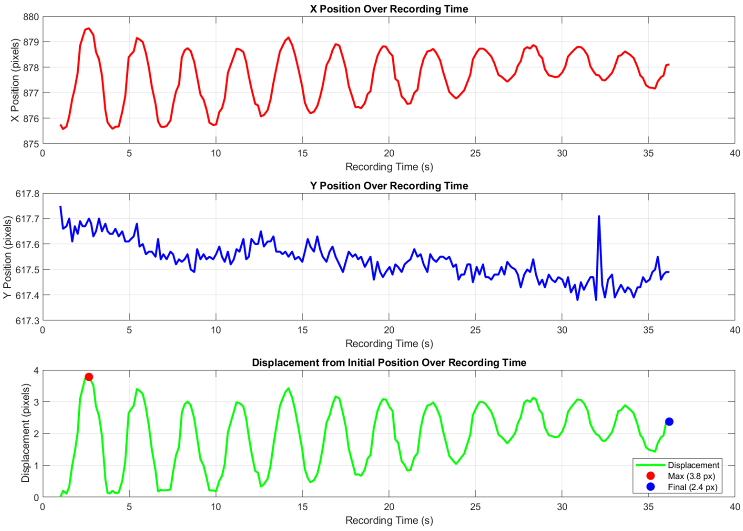

(c) Response to slow ramp-up in Phase 3.

Figure 7.2: Response to charging different phases at low voltage (0-240 V). Red: X-coordinate; Blue: Y-coordinate; Green: total displacement from starting position.

### 7.1.1. Low-Voltage Dynamic Actuation

Dynamic actuation at selected frequencies can exploit the system's natural dynamics to create larger displacements, similar to a swing gaining momentum. Two variations were tested: 1. Sequential phase activation to create a continuous pulling force. 2. Sequential activation combined with partial charging of an additional phase for an even more continuous force.

**Sequential Phase Activation**

By cycling through Phases 1, 2, and 3, the pulling force becomes continuous enough to move the stage beyond a single electrode. As the stage shifts, it is successively attracted to the next electrode in sequence. This effect is shown in Figure 7.3.

When operated near resonance, a frequency response curve can be measured, as shown in Figure 7.4.The code to control the Arduino for different frequencies is provided in Appendix D.

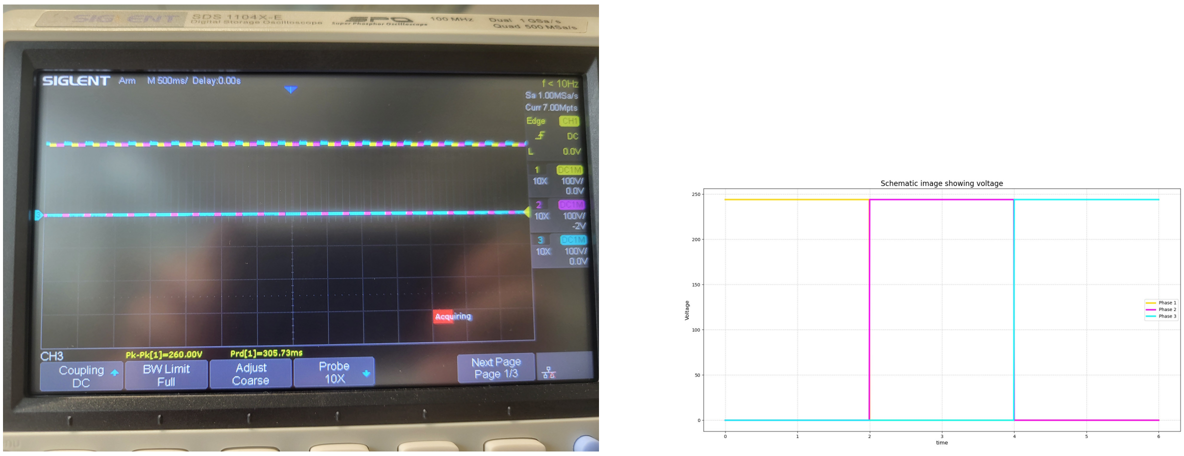

(a) Oscilloscope.

(b) Theoretic control.

Figure 7.3: Electrode charged to 244 V. Yellow: Phase 1; Pink: Phase 2; Blue: Phase 3. In this example, only one electrode is charged at a time.

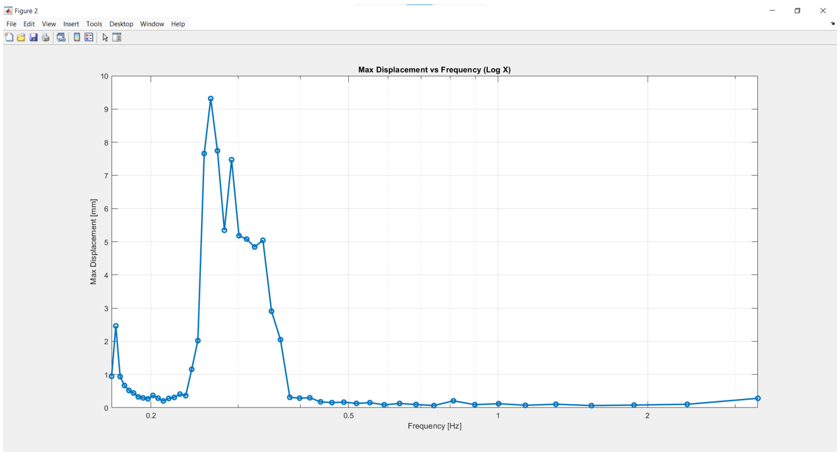

Figure 7.4: Frequency response for combined-phase actuation at 244 V.

### Sequential Phase Activation with Partially Activation

Partially charging an additional phase produces a more uniform force profile, which can alter the resonance characteristics. The voltage on the electrodes is shown by the oscilloscope in Figure 7.5. In this setup, motion was slightly reduced, but a secondary resonance peak emerged (Figure 7.6).

In earlier experiments using an FR4 PCB and brick magnet array, this method produced the largest displacements, likely due to the more constant pulling force—even when the stage was not ideally positioned for the active electrode.

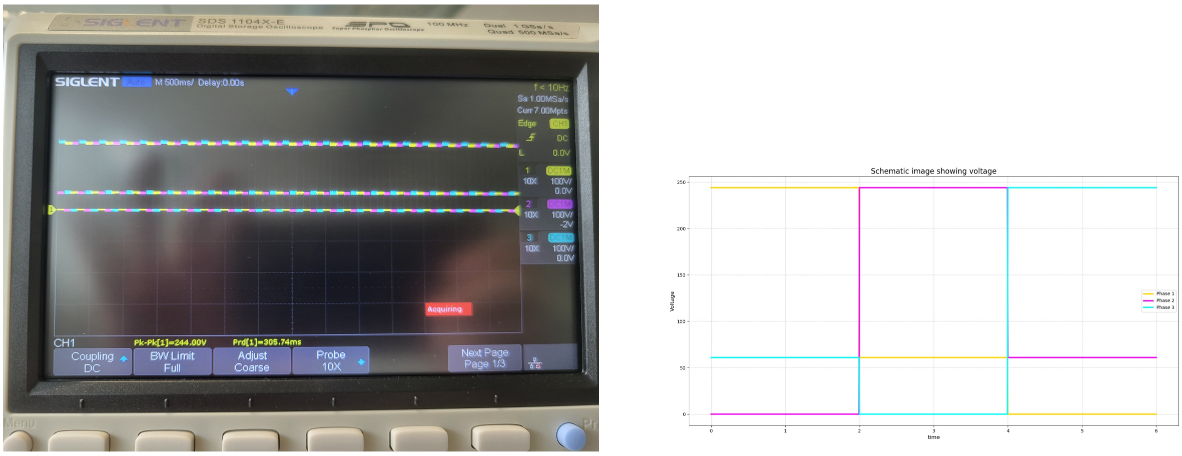

(a) Oscilloscope.

(b) Theoretic control.

Figure 7.5: Electrode charged to 244 V. Yellow: Phase 1; Pink: Phase 2; Blue: Phase 3. In this example, only one electrode is charged at a time.

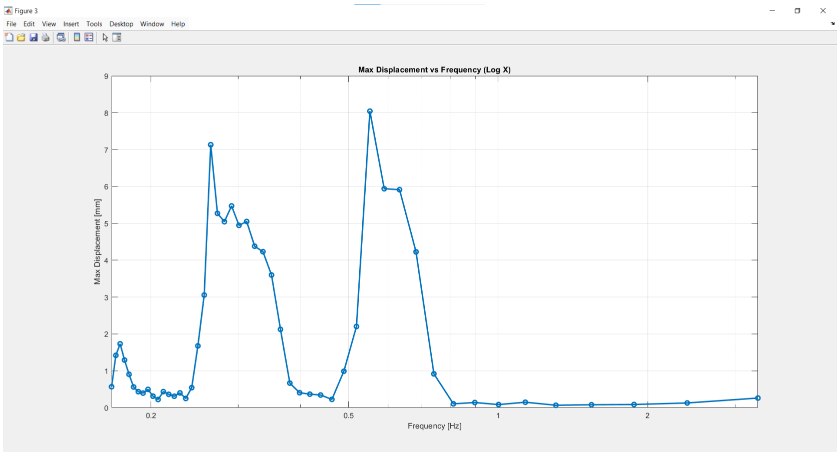

Figure 7.6: Frequency response for combined and partially charged actuation at 244 V.

### Dynamic Movement Control for Low Voltage

Further analysis of the low-voltage dynamic response is shown in Figure 7.7. The example at 0.248 Hz which falls below the resonance peak does not display a clear Duffing-type response. Although the mechanical system is nonlinear, the applied actuation at this amplitude and frequency does not supply sufficient momentum to drive the stage between distinct local minima or to strongly excite higher-order nonlinear behaviour. Instead, the measured displacement and velocity show an envelope consistent with a beat frequency between the system natural frequency and the electrode drive frequency. Figure 7.7 presents displacement, velocity and acceleration traces for the 0.248 Hz drive, with the velocity trace in Figure 7.7b highlighting the modulation caused by phase switching. The beat-like pattern is particularly clear in the 0.228 Hz example shown in Figure 7.8.

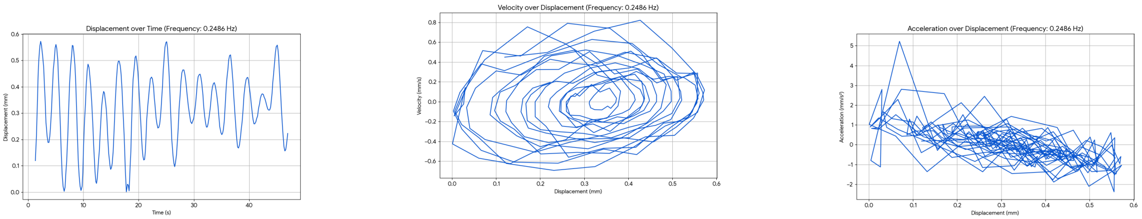

(a) Displacement over time.

(b) Velocity response during phase switching.

(c) Acceleration over the same interval.

Figure 7.7: The system response is shown in three different ways, with actuation at 244 V and a frequency of 0.2486 Hz.

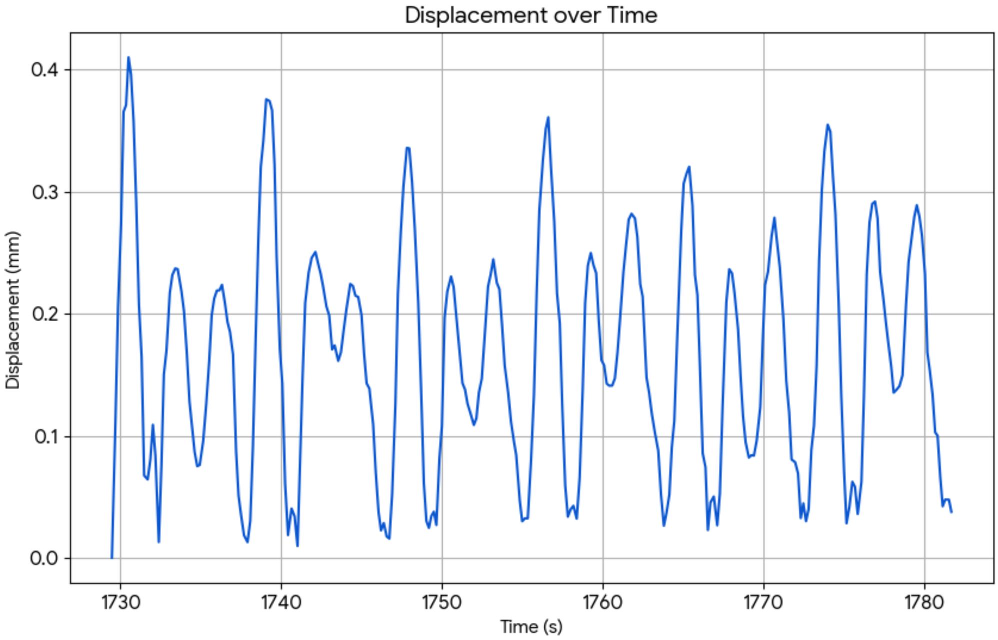

Figure 7.8: Displacement as a result of actuation at 0.228 Hz and 240 V, showing a clear repeating envelope consistent with a beat frequency.

## 7.2. High Voltage

The high-voltage setup provides a range from 0 to 1200 V but permits only one phase to be driven at a time. The following strategies were used to probe the system: instantaneous turn-on to full voltage, slow voltage ramp-up, and periodic (frequency) actuation of a single phase.

### 7.2.1. Turn On and Off

Turning on an electrode and letting it reach its resting position is the quickest way to test the system's capabilities. For this reason it was the first test performed.

In Figure 7.9 the stage's starting position is shown relative to the electrodes.

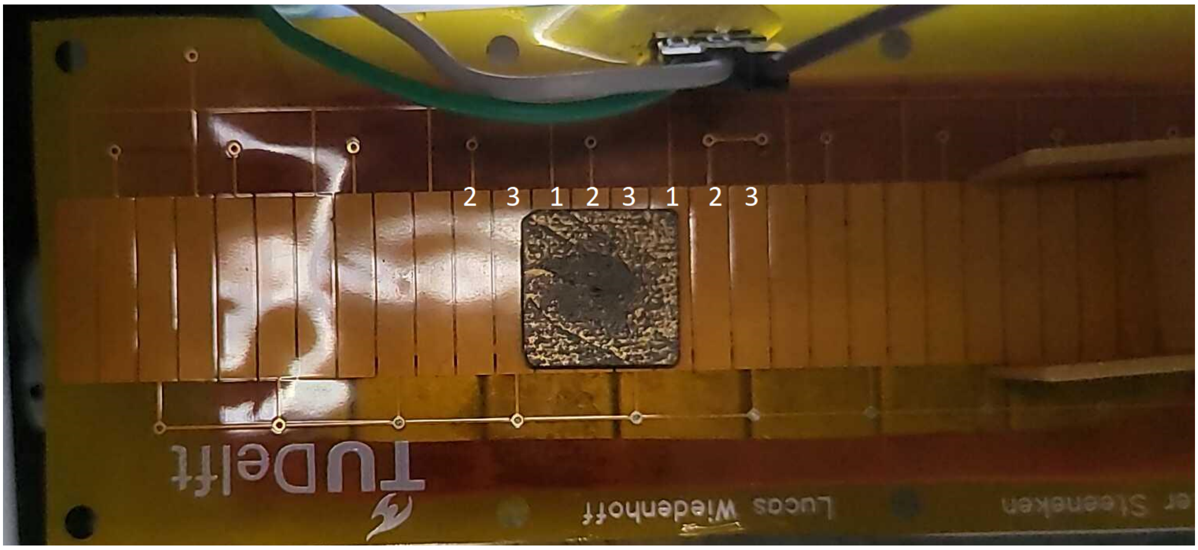

Figure 7.9: Starting position; electrodes are labeled with their respective phase.

The response to different electrodes being charged is shown in Figure 7.10. In this experiment the charged electrode was driven to 800 V. The y-axis is in pixels, where one pixel equals 0.08 mm.

Figure 7.10a shows that the electrode does not move the stage to a new position and only seems to reduce the amplitude of the initial motion. This is expected: as Figure 7.9 shows, the stage almost completely covers the first phase, so the electrostatic force acts as an additional spring toward the starting position. Figure 7.10b shows the stage moving forward by about 45 pixels (3.6 mm). Since a phase is 3 mm wide, this indicates a new stable equilibrium above the second phase. The effect is also visible, to a lesser degree, in Figure 7.10c, where the movement is backward by about 15 pixels (≈1.3 mm) when comparing the steady-state level of the green line between $t = 140$ and $t = 200$; this is consistent with the starting position already slightly overlapping the third phase.

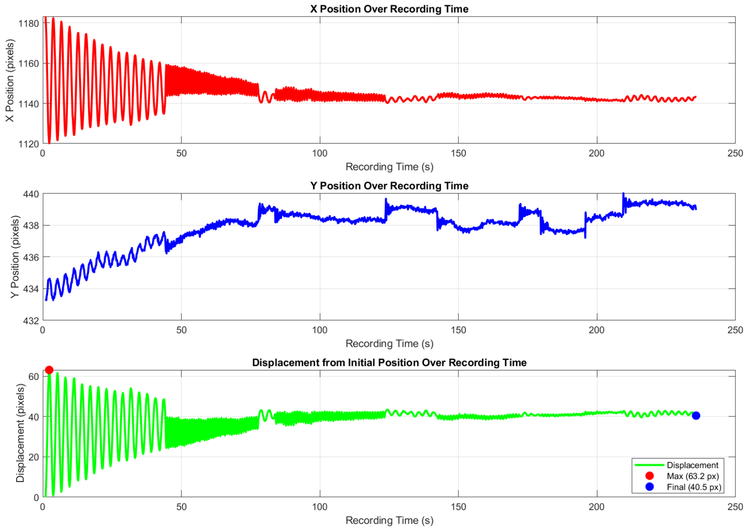

(a) Response to turning phase 1 on (45 s), off (120 s), on (130 s), off (190 s).

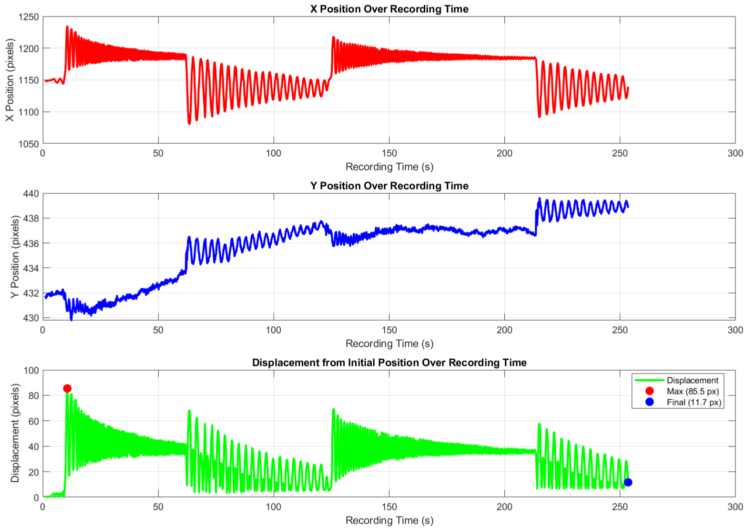

(b) Response to turning phase 2 on (10 s), off (60 s), on (125 s), off (210 s).

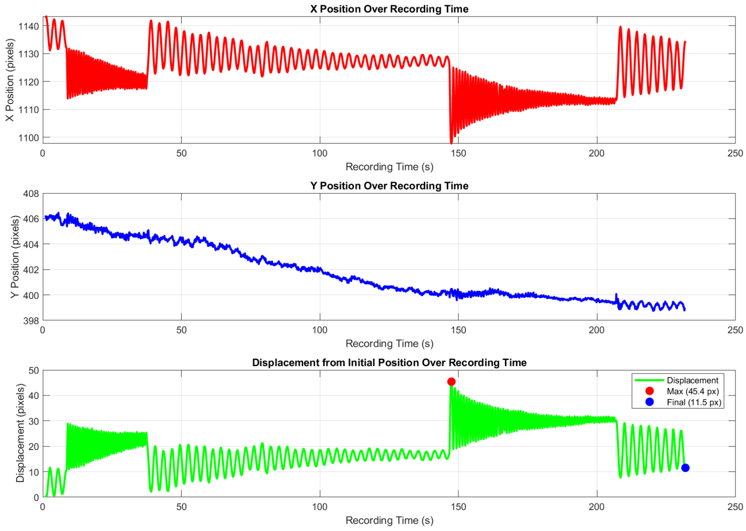

(c) Response to turning phase 3 on (10 s), off (40 s), on (150 s), off (210 s).

Figure 7.10: Response to charging three different phases. Red: X coordinate; Blue: Y coordinate; Green: combined displacement from the starting position (Pythagoras).

### 7.2.2. Steady State

By slowly ramping up the voltage the system remains near steady state, which reduces nonlinear behavior. Using this method, a similar displacement was reached (see Figure 7.11). This is without leaving local minima and transition to a new local minima. Here a movement of 3.5 mm was achieved in steady state, so this would mean just beyond a single stage.

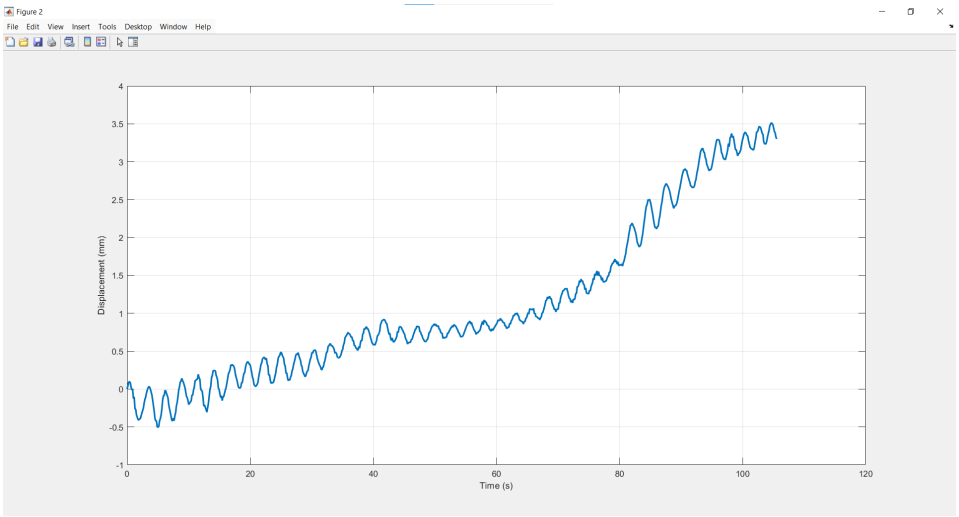

Figure 7.11: Displacement resulting from a slow ramp-up to 1200 V.

### 7.2.3. Dynamic Movement Control for High Voltage

By actuating the stage at a certain frequency, the system can accumulate momentum, enabling larger movements. These movements can overcome the maxima of the magnetic array, pulling the stage past a maximum so that it falls off the array. This behavior is illustrated in Figure 7.12a, where the stage was actuated at 600 V with a frequency of 1 Hz.

The effect was found to depend on two factors: the tilt of the stage (which changes the system response) and the specific electrode actuated. For another phase with the same settings, the effect did not occur (Figure 7.12b), nor did it occur when a different frequency was used (Figure 7.12c).

These results show that resonance can enable a wider range of motion at reduced voltages. Overall, while this method could be used to generate enough momentum to pull the stage off the magnetic array in many configurations, it would require voltages of 1200 V.

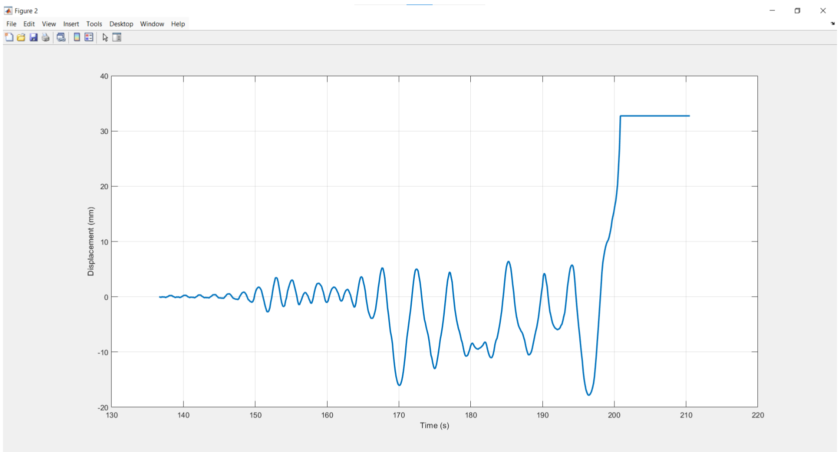

(a) Fall from magnet array due to 600 V at 1 Hz on phase 1 electrodes.

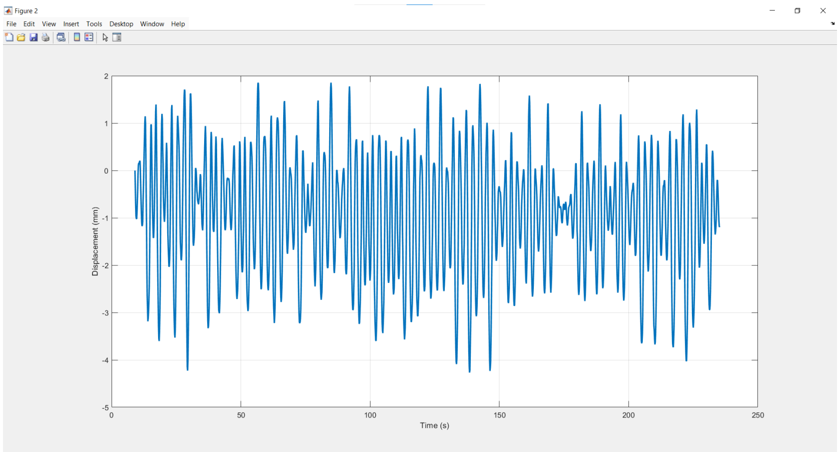

(b) No fall from magnet array with 600 V at 1 Hz on phase 3 electrodes.

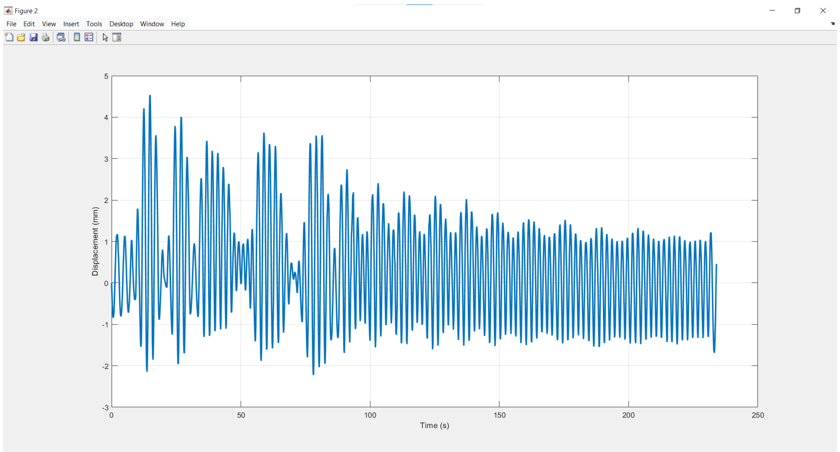

(c) No fall from magnet array with 600 V at 0.5 Hz on phase 1 electrodes.

Figure 7.12: Three different actuation results.

# 7.3. Escape from Local Minima

## 7.3.1. Crossing a Saddle Point

As stated earlier in Chapter 6, there are two nearby local minima separated by a saddle point. The difficulty of crossing the saddle depends strongly on the stage tilt, but transitions have been achieved using the following strategies: an impulse (Figure 7.13a) and a slow ramp-up (Figure 7.13b).

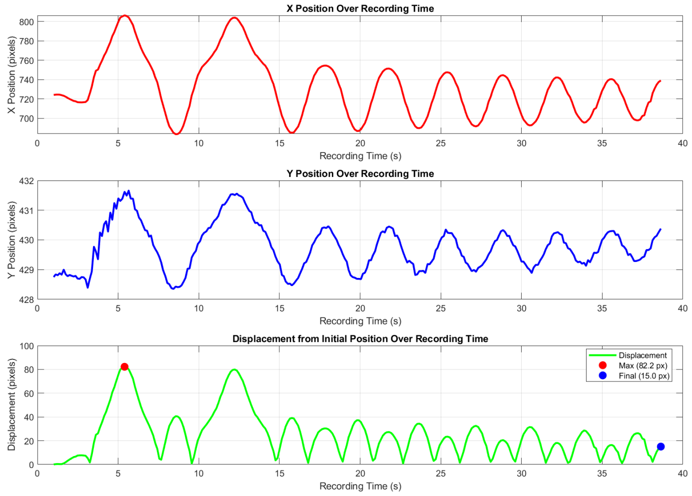

(a) Nonlinear response associated with transposition between minima caused by a 720 V pulse.

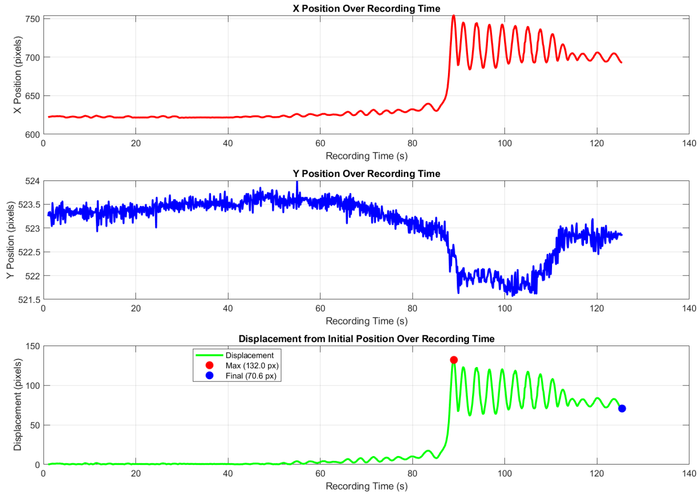

(b) A jump to another local minimum after a slow ramp-up to 840 V; the movement settles at a different location.

Figure 7.13: Two methods for achieving crossover. Red: X coordinate; Blue: Y coordinate; Green: combined displacement from the starting position.

### 7.3.2. Falling Off the Magnet Array

In certain cases, the stage was pulled beyond the boundary of a local minimum, resulting in it falling off the magnet array. An example is shown in Figure 7.14a, where a short impulse of 920 V imparted enough momentum for the stage to escape the local minimum and leave the array. A similar outcome was achieved with a slow voltage ramp-up, as shown in Figure 7.14b, where the full 1200 V was applied to overcome the potential barrier. As noted earlier, periodic actuation at high voltage was also highly effective in consistently pulling the stage from a local minimum.

As discussed in Section 6, the tilt of the magnet array strongly influences the formation of multiple local minima as well as the forces required to transition between them. Achieving this experimentally was challenging due to the level of control needed. In contrast, pulling the stage away from the array could be accomplished by applying sufficient voltage with the right control methods. As long as the stage was not pulled against the PCB by the electrostatic force, pulling the stage off the magnet array was always possible.

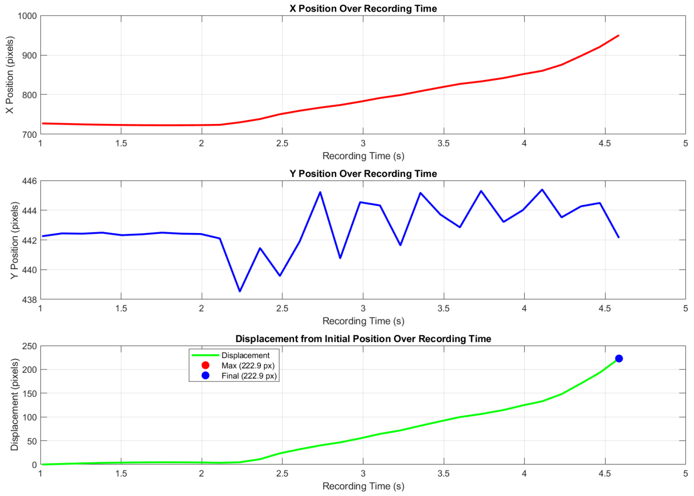

(a) Pull-off from magnet array using a 920 V impulse.

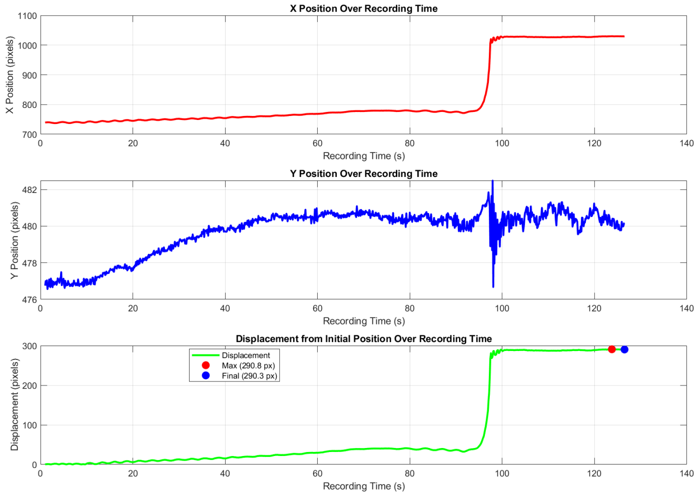

(b) Pull-off from the magnet array using a slow ramp to 1200 V.

Figure 7.14: Two methods that pull the stage out of the local minimum. Red: X coordinate; Blue: Y coordinate; Green: combined displacement from the starting position.

# 8

# Discussion

## 8.1. Insights and Challenges

In this section, the main insights and challenges encountered during the development of the motion stage are presented.

### 8.1.1. Magnet Array

**Railroad Array**

This magnet array was tested with both larger and smaller side magnets. It was observed that smaller side magnets created a more even field but made the configuration resemble the 3-magnet setup, because the middle magnet's influence dominates. Increasing the size of the side magnets mitigates this effect, but at the cost of reducing the number of local minima due to space constraints (80 mm / 10 mm = 8).

The railroad array used in this work could be characterized as a Duffing oscillator, whose characteristics depend strongly on tilt. This means that, to design a controller, the system must be characterized first. Since a Duffing oscillator is a non linear system, predictions are difficult for longer durations, which limits the usefulness of feedforward controllers.

**Brick Array**

For magnet arrays repeatability is the largest challenge, as with all magnet arrays where both the middle and side magnets end in the same place, the point where both the middle and side magnets end will have a strong local minima. This necessarily requires an magnet array like the brick array to be able to move beyond the middle magnet, as the side magnets are required to provide the levitation at the end of the middle magnet.

In this research it was found that the local minima of the middle magnets were still too deep to escape, or could not provide enough height for levitation. These effects could be reduced by adding side magnets in combination with thinner magnets, but as seen with the smaller checkerboard array this does reduce the levitation height overall.

### 8.1.2. Electrodes

As noted before, the main design choice with electrodes is their width: smaller electrodes allow more precise control but produce less force. This can be compensated by increasing the voltage, something not possible with larger electrodes due to “pull-in” effects.

The pull-in phenomenon occurs when the electrostatic downward force, which increases quadratically as the levitation height decreases, causes the stage to collapse onto the PCB once it levitates below a certain threshold height. This can happen due to momentum, tilt or external vibrations. To mitigate this, a flex PCB was used, since lateral force decreases only linearly with height, allowing for higher voltages to be applied for stronger lateral control. As levitation height increases, the ratio of lateral to vertical force becomes more favorable, as further discussed in Section 8.1.3.

In this work, the maximum applied voltage was 1200 V, which occasionally caused pull-in. This suggests that while higher voltages could improve performance, they would also require greater levitation height to avoid collapse. Higher levitation height could be achieved through bigger magnets, thinner stage or a more diamagnetic material. Using smaller electrodes could allow for higher voltages without triggering pull-in.

### 8.1.3. Scaling

When scaling, both diamagnetic forces and gravity scale cubically. Two other scaling effects must be considered:

**Magnetic field scaling**

The surface magnetic field strength of a permanent magnet remains constant regardless of size, but the gradient depends on magnet dimensions. Smaller magnets produce steeper (more negative) gradients, which generate stronger local diamagnetic forces at close range but also cause the force to decay more rapidly with distance. This is illustrated in Figure 8.1, where the magnet size is plotted against the vertical ($F_z$) force for various distances. Larger magnets produce a more uniform force distribution. As a result, they generate a stronger diamagnetic force than smaller magnets at greater distances, but a weaker force when very close to the magnet's surface.

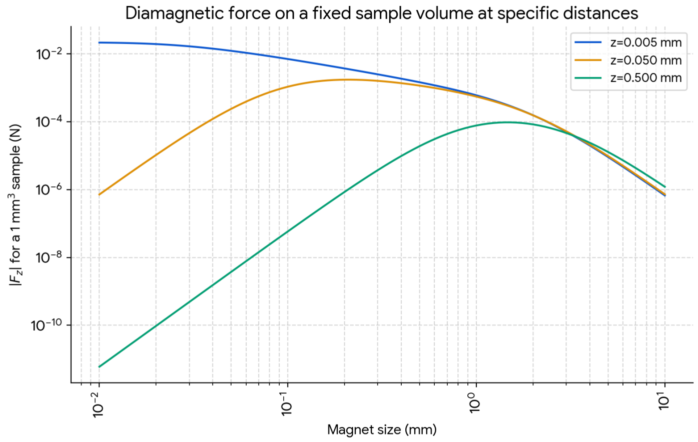

Figure 8.1: Magnet size versus vertical force density for various distances.

**Electrostatic force scaling**

Electrostatic force scales with electrode surface area, and therefore quadratically. Firstly, when scaling up, its relative significance decreases compared to cubic-scaling forces (gravity and diamagnetism); when scaling down, its relative significance increases. Second, as the levitation height decreases, the vertical (z) component of the electrostatic force increases, leading to a greater downward pulling force.

A comparison was done using the previous model and this has been plotted in Figure 8.2 (here maximum forces are compared). The following aspects were tested; half levitation height, double levitation height and half size of the stage (scaling the electrodes accordingly). As preciously said the total force scales quadratically with levitation height and area.The primary cause is the force in the z-direction. This is best illustrated by the force in the x-direction $F_x$, where a lower height led to a doubling rather than a four-fold increase.

By comparing the ratio between $F_x$ and $F_z$ it can be seen that indeed the ratio halves when levitating lower and doubling when at double height. The final observation is that a smaller stage decreases the ratio of $F_x$ to $F_z$, similar to the effect of doubling the levitation height. This occurs because the electrodes necessarily also need to scale down to allow the four-phase system to function. This caps the maximum area but not the change in area, leading to $F_z$ scaling down further than $F_x$, which also depends on the change in area.

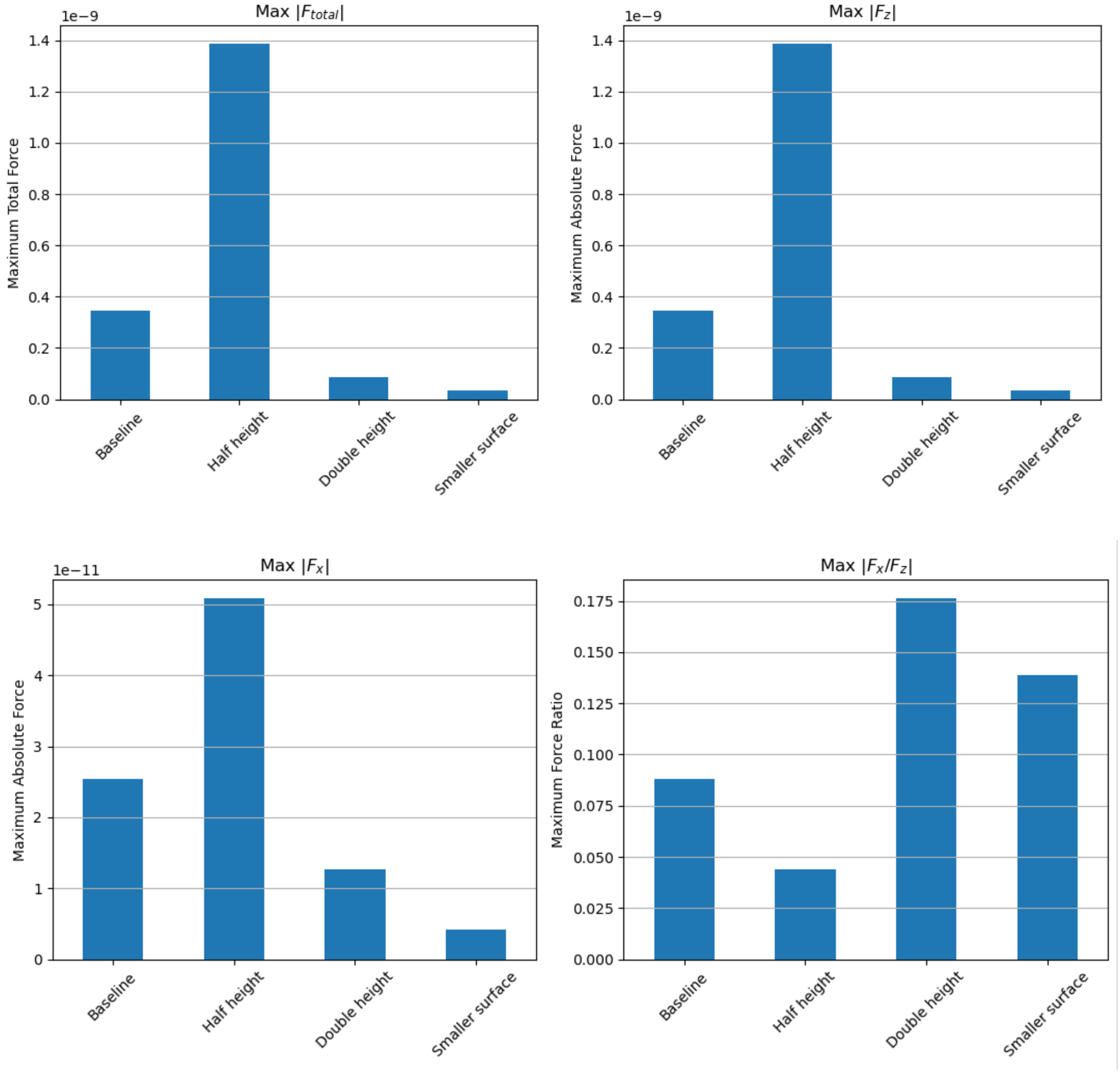

Figure 8.2: Comparison of total force magnitude, vertical ($z$) component, lateral ($x$) component, and $F_x/F_z$ ratio.

To summarize, when scaling down:

- The downward gravitational force decreases cubically.
- Electrostatic force decreases quadratically, with a proportionally larger vertical component at lower levitation heights.
- Diamagnetic force also decreases cubically, but smaller magnets increase $\nabla\vec{B}^2$ at low heights, strengthening local diamagnetic forces.

## 8.2. Cost Analysis

For this project the potential costs of such a device was also an important consideration. The total project costs can be divided into design costs and electronics costs. Since two setups were used (low-voltage and high-voltage), electronics costs are further split into shared components and setup-specific components.

- Flex-PCB electrodes – Ordered from JLCPCB in batches of 10 for €53.80 total (€5.38 each).
- HOPG stage material – A recycled stage was used for most tests, but new “H” and “O” stages were manufactured from Highly Oriented Pyrolytic Graphite purchased for €7.91 per piece.
- Square magnets – Purchased from supermagnete for €1.56 each; 16 magnets are required for a single array, totaling €24.96.
- Long magnets – Purchased from HKCM for €21.54 each; one is required per array.

Subtotal (design): €59.79. These costs assume only one stage and one magnet array are produced. Larger-scale production would reduce the per-unit cost, but prototyping remains relatively expensive.

These items were used in both the low- and high-voltage setups:

- Tip-tilt stage – Prices range from €150 to €1000 depending on precision and build quality.
- Image tracking system – In this study, an iPhone 11 was used (~€700), but comparable devices (e.g., Pixel 9a) are available for ~€500. With surface finish improvements for tracking visibility, a lower-cost camera could be used.

Estimated shared electronics cost: ~€650 (mid-range assumption).

- Arduino Uno – €29.03
- Adafruit MCP4728 Quad DAC – €7.50
- ADM01007 HV56264 Quad High Voltage Amp Array EVB – €64.89
- High-voltage power supply (300 V) – Commercial options range from €150 to €2000; the low-end estimate is used here.

Subtotal (low voltage): ~€250 (using lower estimate cost).

- High-voltage power supply (SenseG) – No longer commercially available, but equivalent units cost ~€1000 or more.

Subtotal (high voltage): ~€1000.

| Category | Estimated Cost (€) | Notes |
|---|---:|---|
| Design (magnets, PCB, HOPG) | 59.79 | One array + one stage |
| Shared electronics | ~650 | Tip-tilt stage + camera |
| Low-voltage setup | ~250 | Arduino + DAC + HV amp + PSU |
| High-voltage setup | ~1000 | Single HV PSU |
| Total (low-voltage) | ~960 | Design + shared + low-voltage setup |
| Total (high-voltage) | ~1710 | Design + shared + high-voltage setup |

These costs can still be reduced as follows:

- Image tracking – Current setup relies on a high-quality smartphone camera, which is a major cost driver. Cheaper options can be used if surface finish or optical markers are added to the stage.
- Voltage supply – High-voltage components dominate the electronics budget. Reusing existing supplies or designing a custom supply could greatly reduce costs.
- Bulk production – Scaling up production would reduce per-unit costs for PCBs, magnets, and mechanical components.

## 8.3. Movement Range

### 8.3.1. Smaller 10 phase Rectangle Design and Side-Rail Design Verification

To verify that the other electrodes were functioning as expected, the switching on and off experiments were also conducted on the 10 phase and side-rail designs. This experiment was chosen because, for the 4 phase design, it provided the largest movement range. The results of these experiments can be seen in Appendix E.

In these tests, the maximum movement for the 10 phase design was 6.9 pixels (Figure E.1), corresponding to a movement range of 0.56 mm. The side-rail design had a maximum movement of 2.7 pixels (Figure E.4), or 0.22 mm. As expected, these values are lower than those of the 4 phase electrode design. The 10 phase design was significantly limited by the fact that each phase was only 0.8 mm long, constraining the maximum movement range.

The side-rail design performed worse than expected, likely due to boundary effects, which strengthen the electrostatic force in the x direction. These effects are enhanced by longer electrodes and weakened by shorter electrodes. This effect is expected to already be near its maximum in the 4 phase design. Consequently, the side-rail design reduces the force because its smaller width decreases the change in area, thereby reducing $F_x$, as explained in Section 2.2.1.

### 8.3.2. Final Design Movement Range

By using a slow voltage ramp to cross the saddle point, stable, controlled motion of 5.5 mm was achieved (Figure 7.13b) at a top speed of 8.5 mm/s. This motion is highly dependent on stage tilt, which significantly influences the presence of local minima.

Larger movements are possible, but in this study they were only achieved by pulling the stage out of the array. If a magnet array could be made repeatable, similar to the brick array, but with sufficient levitation height, the same technique could potentially achieve controlled motion over distances exceeding 20 mm.

# 9

# Conclusion and recommendations

## 9.1. Conclusion

The research question of this thesis is: What would be an optimal design for a long range actuator to create maximum movement range using diamagnetic levitation to eliminate contact friction and electrostatic force as propulsion method using only feedforward control, while keeping the cost low?

To answer this question, all sub-questions formulated in Section 1 are answered below based on the results of the research conducted for this thesis.

### The Optimal Electrode PCB Design

Among the tested electrode designs, the 4 phase rectangle design proved to be the most effective in generating electrostatic force. Incorporating the height-scaling effect by using a thinner PCB further improved the design significantly. This 4 phase rectangle electrode pattern was fabricated and tested, demonstrating optimal performance for statically determined control. The 4 phase design was able to generate 5.5 mm movement compared to the 10 phase and side-rail design which have respectively 0.56 mm and 0.22 mm movement. The minimum electrode width should match the width of the stage, while a wider electrode does not hinder the electrostatic force. A voltage between 800 V and 1200 V generated sufficient force to overcome the saddle point. Higher voltages, combined with increased levitation height, may further enhance lateral force.

### The Optimal Magnet Array Design

An optimal magnet array design was not identified. But through research, modeling and testing two promising arrays were found:

- Railroad array – Provided two local minima for stage switching when properly tiled, but lacked repeatability and retained steep local minima at the ends.
- Brick array – Potentially more repeatable, but one local minimum was too weak to sustain high levitation.

The railroad array was further characterized and proven to be best described as a Duffing oscillator. In this case, one of the local minima is weaker than the other, and these are highly dependent on the tilt of the magnet array. For the stronger local minima, the stiffness and damping coefficient are calculated to be $6.37 \cdot 10^{-4}$ N/m and $8.37 \cdot 10^{-6}$ N·s/m, Respectively.

### The Optimal Stage Design

The stage's shape significantly affects stability within the magnetic field. Three designs were considered, revealing that reducing the influence of the middle magnet row decreased levitation height, since that row contributed strongly to the magnetic field. Stage shape also influenced susceptibility to electrostatic forces: because the PCB electrodes were rectangles, non-square stages had parts acting mainly as connecting beams rather than active surfaces. Considering stability, levitation, and electrode compatibility, a square stage was determined optimal for this setup.

**Control Strategies and Movement Range**
Different control strategies are presented with their respective movement ranges and behaviors.

First, we will examine the stable movements achieved with various control strategies.

The most basic strategy involved instantly applying maximum voltage. This produced a quick burst of movement before the stage stabilized in a new location. This method achieved a movement range of approximately 55 pixels (4.3 mm).

By slowly charging the electrode, the stage lacked the momentum to reach a more distant electrode, which resulted in a lower movement range of 3.5 mm.

Only the ramp-up strategy could achieve a crossover to a new, smaller local minimum and maintain a steady state. This resulted in a larger motion of 5 to 8 mm. While a short impulse could also achieve this crossover, it generated too much momentum, causing the stage to cross back over and settle in the original local minimum.

Next, we look at the extended range movement of the stage.

The stage was also made to fall from the magnet array. This achieved a significantly larger movement of at least 23.4 mm. This result was accomplished using multiple strategies, including a short impulse, a slow ramp-up, and an actuation using a periodic on/off frequency. However, this strategy is not ideal because the stage becomes stuck in an inescapable minimum.

**Necessary Cost and Reduction Potential**
In summary, the cost analysis shows that the device can be realized with a total estimated expense of around €960 for the low voltage setup and €1710 for the high voltage setup. A clear distinction emerges between the mechanical design components (magnets, stages, and PCBs), which remain relatively inexpensive, and the electronics, which account for the majority of the overall cost. The largest cost drivers are the image tracking system and the high voltage power supply. While prototyping remains relatively expensive, several strategies such as using lower cost imaging solutions, reusing or custom designing voltage supplies, and leveraging bulk production could significantly reduce costs in future iterations, making the system more scalable and economically viable.

**Final Answer to the Research Question**
To conclude the main research question: The costs are high, mainly due to the intrinsic expense of high-voltage equipment and image tracking. These could be reduced by using alternative tracking methods or if the device already operates with a high-voltage supply.

The optimal electrode and stage design found in this study proved to be the square stage with the rectangular 4 phase electrode design. Using square flex-PCB electrodes in a 4 phase design together with a square HOPG stage gave stable movement of 5.5 mm at 840 V. At 1200 V the stage could be completely pulled from the array, although it then needed to be manually repositioned.

For the magnet array, both the brick and railroad configurations showed potential, each with trade-offs between stability and levitation height.

While feedforward control can handle short-term actuation, the inherently nonlinear and multi-stable behavior of the system causes accuracy to degrade over time. For long-term reliable operation, a feedback control system is necessary.

## 9.2. Recommendations

Given the challenges identified in this study, several recommendations are suggested to improve the experimental design and guide subsequent research.

### 9.2.1. Using Ring Magnets

Using ring magnets, a track can be constructed that enables 1D motion without saddle points to overcome. If the stage is larger than the central magnets, rotors can be created that levitate at the center and rotate. Conversely, making the stage smaller than the ring magnets enables the creation of a "track" in which the stage floats on a local minimum. The limitation of this system is that the stage can only move along the circular path of the magnet.

### 9.2.2. Using Magnets with Sharp Edges

To make the magnetic field created by magnet arrays more uniform, the edge radius of the magnets can be decreased. This requires the magnets to be fabricated accordingly, since post-processing of magnets is strongly discouraged. By combining this with multiple 3 magnet arrays, one can create an array that is almost equivalent to an infinitely long magnet array.

### 9.2.3. Compliant Stage

As shown in [10], compliant beams can be used to connect multiple stages. This approach could smooth out local minima in the magnetic field, making the overall field experienced by the stage more uniform. The beams would need to be lightweight and conductive to avoid hindering levitation while also enabling electrostatic force actuation.

### 9.2.4. Feedback Control

In this study, a rudimentary feedforward control method was implemented, which proved sufficient to achieve a much larger range of motion. However, this control scheme does not provide accurate control and can not deal with the non linearity. Incorporating feedback control could combine this extended range with the ability to position the stage more precisely at specific locations.

### 9.2.5. Nanometer-Level Tracking

Previous research has demonstrated that nanometer-scale motion is achievable using electrostatic actuation. As the experimental setup used in this study could not measure nano-level measurements, a similar study as previously done could be conducted with the design presented in this paper to characterize its capability for nanometer-level movement in 1D. Such precision may only be achievable at specific locations on the magnet array, making it important to identify and test these regions to determine their specific performance limits. In addition, effective vibration isolation would be critical to ensure reliable nanometer-scale characterization and operation.

### 9.2.6. a Halbach Brick Array

To make the brick array viable for the use of a motion stage the local minima of the middle magnets need to be elevated. This might be possible by combining a Halbach array with a brick array, which could merge the enhanced magnetic strength of the Halbach configuration with the local minima separation provided by the brick array. However, assembling such a hybrid would be challenging, as both Halbach and brick arrays are already complex to construct individually, and combining them could further increase the difficulty.

# A

# Appendix A: Magnetic Field Calculation

```
import matplotlib.pyplot as plt
import numpy as np

# Define the air side length (in mm)
Length = 120
Width = 40
Height = 5
Ms = 1.3*10**6
mu0 = 4 * np.pi * 1e-7  # vacuum permeability

# Define grid resolution (e.g., 100 µm steps)
step_mm = 0.05  # 10 µm = 0.01 mm

# Create 1D arrays for each axis
x = np.arange(0, Length, step_mm)
y = np.arange(0, Width, step_mm)
z = np.arange(0, Height, step_mm)

# Create 3D grid
X, Y, Z = np.meshgrid(x, y, z, indexing='ij')

print(f”Grid shape: {X.shape}”)
Bx, By, Bz = 0, 0, 0
decimal= 5
m2mm = 10**-3 #convert m to mm
eta = 10**-9 #used to prevent devided by zero

#Functions too caculate the magnetic flux density as result of magnets
def F_mag( X, Y, Z, x, y1, y2, z,):
    # Compute squared distances to avoid repeated computation
    dx = np.round(X - x, decimals=decimal)
    dz = np.round(Z - z, decimals=decimal)

    r1 = np.sqrt(dx**2 + (Y - y1)**2 + dz**2+eta)
    r2 = np.sqrt(dx**2 + (Y - y2)**2 + dz**2+eta)

    F = (Y - y1 + r1) / (Y - y2 + r2)
    return F*m2mm

def Bx_mag(X, Y, Z, x, y, z, l, b, h, Ms):
    prefactor = mu0 * Ms / (4 * np.pi)

    xm_vals = [x - l/2, x + l/2]
    zk_vals = [z - h/2, z + h/2]
    y1 = y + b/2
    y2 = y - b/2

    result = np.zeros_like(X, dtype=np.float64)

    for k in range(2):
        for m in range(2):
            sign = (-1) ** (k + m)
            xm = xm_vals[m]
            zk = zk_vals[k]
            F_val = F_mag(X, Y, Z, xm, y1, y2, zk)
```

```
            result += sign * np.log(F_val+eta)

    return prefactor * result

def H_mag( X, Y, Z, y, x1, x2, z,):
    # Compute squared distances to avoid repeated computation
    dy = np.round(Y - y, decimals=decimal)
    dz = np.round(Z - z, decimals=decimal)

    r1 = np.sqrt(dy**2 + (X - x1)**2 + dz**2+eta)
    r2 = np.sqrt(dy**2 + (X - x2)**2 + dz**2+eta)

    H = (X - x1 + r1) / (X - x2 + r2)
    return H*m2mm

def By_mag(X, Y, Z, x, y, z, l, b, h, Ms):
    prefactor = mu0 * Ms / (4 * np.pi)

    ym_vals = [y - b/2, y + b/2]
    zk_vals = [z - h/2, z + h/2]
    x1 = x + l/2
    x2 = x - l/2

    result = np.zeros_like(X, dtype=np.float64)

    for k in range(2):
        for m in range(2):
            sign = (-1) ** (k + m)
            ym = ym_vals[m]
            zk = zk_vals[k]
            H_val = H_mag(X, Y, Z, ym, x1, x2, zk)
            result += sign * np.log(H_val+eta)

    return prefactor * result

def G_mag( X, Y, Z, x, y, z,):
    # Compute squared distances to avoid repeated computation
    dx = X-x #np.round(X - x, decimals=decimal)
    dy = Y-y #np.round(Y - y, decimals=decimal)
    dz = Z-z #np.round(Z - z, decimals=decimal)

    G = (1) / np.sqrt(dx**2 + dy**2 + dz**2+eta)
    return G*m2mm

def Bz_mag(X, Y, Z, x, y, z, l, b, h, Ms):
    prefactor = mu0 * Ms / (4 * np.pi)

    xn_vals = [x - l/2, z + l/2]
    ym_vals = [y - b/2, y + b/2]
    zk_vals = [z - h/2, z + h/2]


    result = np.zeros_like(X, dtype=np.float64)

    for k in range(2):
        for n in range(2):
            for m in range(2):
                sign = (-1) ** (k + m + n)
                xn = xn_vals[n]
                ym = ym_vals[m]
                zk = zk_vals[k]
                Gval = G_mag(X, Y, Z, xn, ym, zk)
                Value = Gval * ((X-xn)*(Y-ym)/(Z-zk+10**-11))
                result += sign * np.arctan(Value+eta)

    return prefactor * result

#define new magnet X,Y,Z = grid, x,y,z = middle location, l,b,h = dimensions of new mag
def New_Magnet(X,Y,Z,Bx,By,Bz, x=0, y=0, z=0, l=40, b=10, h=10, Ms=9*10**5):
    Bx = Bx + Bx_mag(X, Y, Z, x, y, z, l, b, h, Ms)
    By = By + By_mag(X, Y, Z, x, y, z, l, b, h, Ms)
    Bz = Bz + Bz_mag(X, Y, Z, x, y, z, l, b, h, Ms)
    return Bx, By, Bz

#Define magnet array
#middle magnets
Bx, By, Bz = New_Magnet(X,Y,Z,Bx,By,Bz, 60, 20,-5,80,10,10,Ms)

step = 1 #prev 0.1
```

```
#top magnets
Bx, By, Bz = New_Magnet(X,Y,Z,Bx,By,Bz, 20+5, 30,-5,10,10,10,-Ms)
Bx, By, Bz = New_Magnet(X,Y,Z,Bx,By,Bz, 20+15+step, 30,-5,10,10,10,-Ms)
Bx, By, Bz = New_Magnet(X,Y,Z,Bx,By,Bz, 20+25+step*2, 30,-5,10,10,10,-Ms)
Bx, By, Bz = New_Magnet(X,Y,Z,Bx,By,Bz, 20+35+step*3, 30,-5,10,10,10,-Ms)
Bx, By, Bz = New_Magnet(X,Y,Z,Bx,By,Bz, 20+45+step*4, 30,-5,10,10,10,-Ms)
Bx, By, Bz = New_Magnet(X,Y,Z,Bx,By,Bz, 20+55+step*5, 30,-5,10,10,10,-Ms)
Bx, By, Bz = New_Magnet(X,Y,Z,Bx,By,Bz, 20+65+step*6, 30,-5,10,10,10,-Ms)
Bx, By, Bz = New_Magnet(X,Y,Z,Bx,By,Bz, 20+75+step*7, 30,-5,10,10,10,-Ms)

#bottom magnets
Bx, By, Bz = New_Magnet(X,Y,Z,Bx,By,Bz, 20+5, 10,-5,10,10,10,-Ms)
Bx, By, Bz = New_Magnet(X,Y,Z,Bx,By,Bz, 20+15+step, 10,-5,10,10,10,-Ms)
Bx, By, Bz = New_Magnet(X,Y,Z,Bx,By,Bz, 20+25+step*2, 10,-5,10,10,10,-Ms)
Bx, By, Bz = New_Magnet(X,Y,Z,Bx,By,Bz, 20+35+step*3, 10,-5,10,10,10,-Ms)
Bx, By, Bz = New_Magnet(X,Y,Z,Bx,By,Bz, 20+45+step*4, 10,-5,10,10,10,-Ms)
Bx, By, Bz = New_Magnet(X,Y,Z,Bx,By,Bz, 20+55+step*5, 10,-5,10,10,10,-Ms)
Bx, By, Bz = New_Magnet(X,Y,Z,Bx,By,Bz, 20+65+step*6, 10,-5,10,10,10,-Ms)
Bx, By, Bz = New_Magnet(X,Y,Z,Bx,By,Bz, 20+75+step*7, 10,-5,10,10,10,-Ms)

# #Run below when you already run and saved previous calculations
# data = np.load('meshgrids.npz')
# Bx = data['Bx']
# By = data['By']
# Bz = data['Bz']

#dis in mm
z_slice = int(np.round(1/step_mm)) # 5 mm hight

# Plot Bx field at the selected z-slice. Change Bx to By or Bz for respective magnetic
plt.figure(figsize=(10, 5))
plt.title(f'Bx Magnetic Field at z={z_slice*step_mm}mm')
contour = plt.contourf(X[:,:,z_slice], Y[:,:,z_slice], Bx[:,:,z_slice], 50, cmap='jet')
plt.colorbar(label='Bx (T)')
plt.xlabel('X (mm)')
plt.ylabel('Y (mm)')
plt.grid(True, linestyle='--', alpha=0.6)
plt.show()

B_mag = np.sqrt(Bx**2 + By**2 + Bz**2)
plt.figure(figsize=(10, 5))
plt.title(f'Magnetic Field Magnitude at z={z_slice*step_mm}mm')
contour = plt.contourf(X[:,:,z_slice], Y[:,:,z_slice], B_mag[:,:,z_slice], 50, cmap='je
plt.colorbar(label='|B| (mT)')
plt.xlabel('X (mm)')
plt.ylabel('Y (mm)')
plt.grid(True, linestyle='--', alpha=0.6)
plt.show()

def calculate_field_derivatives(Bx, By, Bz, step_mm):
    # Get dimensions of the field arrays
    nx, ny, nz = Bx.shape

    # Initialize derivative arrays (2 smaller in each dimension)
    dBx_dx = np.zeros((nx-2, ny-2, nz-2))
    dBx_dy = np.zeros((nx-2, ny-2, nz-2))
    dBx_dz = np.zeros((nx-2, ny-2, nz-2))

    dBy_dx = np.zeros((nx-2, ny-2, nz-2))
    dBy_dy = np.zeros((nx-2, ny-2, nz-2))
    dBy_dz = np.zeros((nx-2, ny-2, nz-2))

    dBz_dx = np.zeros((nx-2, ny-2, nz-2))
    dBz_dy = np.zeros((nx-2, ny-2, nz-2))
    dBz_dz = np.zeros((nx-2, ny-2, nz-2))

    # Create smaller grid for derivatives (excluding boundaries)
    X_new = X[1:-1, 1:-1, 1:-1]
    Y_new = Y[1:-1, 1:-1, 1:-1]
    Z_new = Z[1:-1, 1:-1, 1:-1]

    # Calculate derivatives using central difference method
    # For x-derivatives: (f(x+h) - f(x-h)) / (2h)
    # For Bx field
    dBx_dx = (Bx[2:, 1:-1, 1:-1] - Bx[:-2, 1:-1, 1:-1]) / (2 * step_mm*m2mm)
```

```
    dBx_dy = (Bx[1:-1, 2:, 1:-1] - Bx[1:-1, :-2, 1:-1]) / (2 * step_mm*m2mm)
    dBx_dz = (Bx[1:-1, 1:-1, 2:] - Bx[1:-1, 1:-1, :-2]) / (2 * step_mm*m2mm)

    # For By field
    dBy_dx = (By[2:, 1:-1, 1:-1] - By[:-2, 1:-1, 1:-1]) / (2 * step_mm*m2mm)
    dBy_dy = (By[1:-1, 2:, 1:-1] - By[1:-1, :-2, 1:-1]) / (2 * step_mm*m2mm)
    dBy_dz = (By[1:-1, 1:-1, 2:] - By[1:-1, 1:-1, :-2]) / (2 * step_mm*m2mm)

    # For Bz field
    dBz_dx = (Bz[2:, 1:-1, 1:-1] - Bz[:-2, 1:-1, 1:-1]) / (2 * step_mm*m2mm)
    dBz_dy = (Bz[1:-1, 2:, 1:-1] - Bz[1:-1, :-2, 1:-1]) / (2 * step_mm*m2mm)
    dBz_dz = (Bz[1:-1, 1:-1, 2:] - Bz[1:-1, 1:-1, :-2]) / (2 * step_mm*m2mm)

    # Create a dictionary to hold all derivatives
    derivatives = {
        'dBx_dx': dBx_dx, 'dBx_dy': dBx_dy, 'dBx_dz': dBx_dz,
        'dBy_dx': dBy_dx, 'dBy_dy': dBy_dy, 'dBy_dz': dBy_dz,
        'dBz_dx': dBz_dx, 'dBz_dy': dBz_dy, 'dBz_dz': dBz_dz,
        'X_new': X_new, 'Y_new': Y_new, 'Z_new': Z_new
    }

    return derivatives

#Calculate derivatives
derivatives = calculate_field_derivatives(Bx, By, Bz, step_mm)

X_new = derivatives['X_new']
Y_new = derivatives['Y_new']
Z_new = derivatives['Z_new']
dBx_dx = derivatives['dBx_dx']
dBx_dy = derivatives['dBx_dy']
dBx_dz = derivatives['dBx_dz']
dBy_dx = derivatives['dBy_dx']
dBy_dy = derivatives['dBy_dy']
dBy_dz = derivatives['dBy_dz']
dBz_dx = derivatives['dBz_dx']
dBz_dy = derivatives['dBz_dy']
dBz_dz = derivatives['dBz_dz']
Bx_new = Bx[1:-1, 1:-1, 1:-1]
By_new = By[1:-1, 1:-1, 1:-1]
Bz_new = Bz[1:-1, 1:-1, 1:-1]

B_mag = Bx_new + By_new + Bz_new
B2dx = (Bx_new*dBx_dx + By_new* dBy_dx + Bz_new* dBz_dx)
B2dy = (Bx_new*dBx_dy + By_new* dBy_dy + Bz_new* dBz_dy)
B2dz = (Bx_new*dBx_dz + By_new* dBy_dz + Bz_new* dBz_dz)

#Calculate diamagnetic force in all directions (anisotropy  not considered)
chi = -40.9* 10**-5
V = m2mm**3*step_mm
mu0 = 4 * np.pi * 1e-7
Fx_mag = B2dx * (chi * V / mu0)
Fy_mag = B2dy * (chi * V / mu0)
Fz_mag = B2dz * (chi * V / mu0)


#Plot force field in X direction. For other direction change Fx_mag to Fy_mag or Fz_mag
plt.figure(figsize=(10, 5))
plt.title(f'(B^2/dx)* (chi * V / mu0) at z-slice {z_slice*step_mm} mm')
contour = plt.contourf(X_new[:,:,z_slice], Y_new[:,:,z_slice], Fx_mag[:,:,z_slice], 50,
plt.colorbar(label='N')
plt.xlabel('X (mm)')
plt.ylabel('Y (mm)')
plt.grid(True, linestyle='--', alpha=0.6)
plt.show()

#Force calculation on the stage
# Choose the z-layer: one below the top
z_idx = 55

# Define size of rectangle (e.g., 10x10 in grid points)
rect_size = int(12/step_mm)
thickness = int(0.5/step_mm)
center_x = X_new.shape[0] // 2
center_y = Y_new.shape[1] // 2
```

```
x_start = center_x - rect_size // 2
x_end = center_x + rect_size // 2
y_start = center_y - rect_size // 2
y_end = center_y + rect_size // 2
# Extract region of force_x (or any other array)
region_force = Fz_mag[x_start:x_end, y_start:y_end, z_idx:z_idx+thickness]
# Sum over the region
total_force = np.sum(region_force)
print(f”Total magnetic force in selected region: {total_force:.4e} N”)
#gravitational force for comparison
masse = (rect_size * m2mm*step_mm)**2 * (thickness * m2mm*step_mm)* 2200
gravity = masse * 9.81
gravity

#moving the stage to evaluate the force in z direction for different stage positions
x_start = 1
x_end = 1+rect_size
y_start = center_y - rect_size // 2
y_end = center_y + rect_size // 2

total_force_z = np.zeros(len(X_new[:,1,1])-2-rect_size)
dx = np.zeros(len(X_new[:,1,1])-2-rect_size)
for n in range(len(total_force_z)):
    region_force = Fz_mag[x_start+n+1:x_end+n+1, y_start:y_end, z_idx:z_idx+thickness]
    total_force_z[n] = np.sum(region_force)
    dx[n] = (n+1)*step_mm
#plotting force in Z direction as result of stage location
plt.plot(dx, total_force_z)
plt.title(”Fz”)
plt.xlabel(”dx”)
plt.ylabel(”Total Force”)
plt.show()
np.max(total_force_z)
#moving the stage to evaluate the force in X direction for different stage positions
x_start = 1
x_end = 1+rect_size
y_start = center_y - rect_size // 2
y_end = center_y + rect_size // 2
total_force_x = np.zeros(len(X_new[:,1,1])-2-rect_size)
dx = np.zeros(len(X_new[:,1,1])-2-rect_size)
for n in range(len(total_force_x)):
    region_force = Fx_mag[x_start+n+1:x_end+n+1, y_start:y_end, z_idx:z_idx+thickness]
    total_force_x[n] = np.sum(region_force)
    dx[n] = (n+1)*step_mm
#plotting force in X direction as result of stage location
plt.plot(dx,total_force_x)
plt.title(f'Fx: stage')
plt.title(”Fx”)
plt.xlabel(”dx”)
plt.ylabel(”Total Force”)
plt.show()
np.max(total_force_x)
#only run to save data
np.savez('meshgrids.npz', Bx=Bx, By=By, Bz=Bz)
```

# B

# Appendix B: Electrostatic Force Calculation

```
%Define parameters
import matplotlib.pyplot as plt
import numpy as np

# Define the air side length (in mm)
Length = 120
Width = 20

# Define grid resolution (e.g., 100 µm steps)
step_mm = 0.1   # 10 µm = 0.01 mm

# Create 1D arrays for each axis
x = np.arange(0, Length, step_mm)
y = np.arange(0, Width, step_mm)

# Create 3D grid
X, Y = np.meshgrid(x, y, indexing='ij')

eta = 10**-9
m2mm = 10**-3

#Functions to define a meshgrid of electrodes and stage.
def stage_mesh(X, Y, x, y, l=12, w=12):
    stage_field = np.zeros_like(X)
    x_start = x - l / 2
    x_end = x + l / 2
    y_start = y - w / 2
    y_end = y + w / 2

    mask = (X >= x_start) & (X <= x_end) & (Y >= y_start) & (Y <= y_end)
    stage_field[mask] = 1
    return stage_field


def phase_mesh(X, Y, l=2.8, w=14, g=0.2, phase=1):
    V_list = [1, 1, 1]
    V_list[phase-1] = 2
    phase_field = np.zeros_like(X)

    y_middle = Y[-1, -1] / 2
    y_start = y_middle - w / 2
    y_end = y_middle + w / 2

    phase_length = l + g
    total_length = X[-1, -1]
    number_phases = int(total_length // (3 * phase_length))

    for i in range(number_phases):
        start = i * 3 * phase_length
        for j in range(3):
            s = start + j * phase_length
```

```
            e = s + l
            mask = (X >= s) & (X < e) & (Y >= y_start) & (Y <= y_end)
            phase_field[mask] = V_list[j]

    return phase_field
#Functions to calculate overlapping area and the change of the overlapping area
def calculate_area(X, Y, dx, w, l):
    count_ones = []
    count_twos = []

    for n in range(len(dx)):
        stage = stage_mesh(X, Y, dx[n], w / 2, l, w)
        surface = stage * electrode
        count_ones.append(np.count_nonzero(surface == 1))
        count_twos.append(np.count_nonzero(surface == 2))

    A1 = np.array(count_ones) * step_mm**2
    A2 = np.array(count_twos) * step_mm**2
    dA1_dx = np.gradient(A1, dx*m2mm)
    dA2_dx = np.gradient(A2, dx*m2mm)
    return A1, A2, dA1_dx, dA2_dx

def calculate_force(A1,A2, dA1_dx, dA2_dx,va,z):
    A1 = A1 * m2mm**2
    A2 = A2 * m2mm**2
    dA1_dx = dA1_dx * m2mm**2
    dA2_dx = dA2_dx * m2mm**2
    c_x = (permittivity*va**2)/(2*z)
    c_z = (permittivity*va**2)/(z**2)
    force_x = - c_x * (A1**2*dA2_dx+A2**2*dA1_dx) / (A1+A2)**2
    force_z = c_z * (A1*A2) / (A1+A2)
    return force_x, force_z

#calculate and plot an example of electrode, stage and overlap

electrode = phase_mesh(X,Y)
stage = stage_mesh(X,Y,6,10)

plt.figure(figsize=(8, 2))
plt.pcolormesh(X, Y, stage, shading='auto', cmap='cividis')
plt.xlabel('X')
plt.ylabel('Y')
plt.title('Stage')
plt.axis('equal')
plt.show()
plt.figure(figsize=(8, 2))
plt.pcolormesh(X, Y, electrode, shading='auto', cmap='cividis')
plt.xlabel('X')
plt.ylabel('Y')
plt.title('Electrode')
plt.axis('equal')
plt.show()


surface = stage* electrode

plt.figure(figsize=(8, 2))
plt.pcolormesh(X, Y, surface, shading='auto', cmap='cividis')
plt.xlabel('X')
plt.ylabel('Y')
plt.title('Electrode × Stage')
plt.axis('equal')
plt.show()
#Calculate Force depending on activated electrode over the different locations of stage
l = 12
w = 12
va = 1200
z = 0.5*m2mm
permittivity = 8.8541878188*10**(-12)
dx = np.linspace(l/2, X[-1, -1]-l/2, round((X[-1, -1]-l)/step_mm))

count_ones = []
count_twos = []

electrode = phase_mesh(X,Y,phase=1)
A1,A2, dA1_dx, dA2_dx   = calculate_area(X,Y,dx,w,l)
F_x_1, F_z_1 = calculate_force(A1,A2, dA1_dx, dA2_dx,va,z)
```

```
electrode = phase_mesh(X,Y,phase=2)
A1,A2, dA1_dx, dA2_dx    = calculate_area(X,Y,dx,w,l)
F_x_2, F_z_2 = calculate_force(A1,A2, dA1_dx, dA2_dx,va,z)

electrode = phase_mesh(X,Y,phase=3)
A1,A2, dA1_dx, dA2_dx    = calculate_area(X,Y,dx,w,l)
F_x_3, F_z_3 = calculate_force(A1,A2, dA1_dx, dA2_dx,va,z)

#plot overlapping area and change of overlapping area as result of location of stage wi
fig, axs = plt.subplots(2, 1, figsize=(8, 6), sharex=True)

# Overlap areas
axs[0].plot(dx, A1, label='Area of 1s', color='tab:blue')
axs[0].plot(dx, A2, label='Area of 2s', color='tab:orange')
axs[0].set_ylabel('Area (mm²)')
axs[0].set_title('Overlap Area with Electrode Phases')
axs[0].legend()
axs[0].grid(True)

# Derivatives of overlap areas
axs[1].plot(dx, dA1_dx, label='d(Area 1s)/dx', color='tab:blue')
axs[1].plot(dx, dA2_dx, label='d(Area 2s)/dx', color='tab:orange')
axs[1].set_xlabel('X Position (mm)')
axs[1].set_ylabel('dArea/dx (mm²/mm)')
axs[1].set_title('Spatial Derivative of Overlap Areas')
axs[1].legend()
axs[1].grid(True)

plt.tight_layout()
plt.show()

#Plot Force result of location of stage with third phase charged. Change F_x_3, F_y_3 t

#calculate maximum force on all locations of the stage
F_x_all = np.vstack([F_x_1, F_x_2, F_x_3])
F_z_all = np.vstack([F_z_1, F_z_2, F_z_3])

F_x_max = np.max(F_x_all, axis=0)
F_z_max = np.max(F_z_all, axis=0)

Phase_Fx_max = np.argmax(F_x_all, axis=0) + 1
Phase_Fz_max = np.argmax(F_z_all, axis=0) + 1

#plotting maximum force on all locations of the stage
fig, axs = plt.subplots(2, 1, figsize=(8, 6), sharex=True)

axs[0].plot(dx, F_x_max, label='Force X-direction', color='tab:blue')
axs[0].set_ylabel('Force (N)')
axs[0].set_title('Maximum force in X direction')
axs[0].legend()
axs[0].grid(True)

axs[1].plot(dx, F_z_max, label='Force Z-direction', color='tab:orange')
axs[1].set_xlabel('X Position (mm)')
axs[1].set_ylabel('Force (N)')
axs[1].set_title('Maximum force in Z direction')
axs[1].legend()
axs[1].grid(True)

plt.tight_layout()
plt.show()
```

# C

# Appendix C: Stage Tracking

```
%Define parameters
captureInterval = 1/10;
numImages = 10*30; %30 seconds per experiment
ipCamURL = 'http://192.168.1.1/video'; % Update to your IP

% Create unique session folder
sessionNumber = 1;
saveFolder = sprintf('Tracking_Only__%s_%d', datestr(now, 'mmdd'),
   sessionNumber);

while exist(saveFolder, 'dir')
    sessionNumber = sessionNumber + 1;
    saveFolder = sprintf('Tracking_Only__%s_%d', datestr(now, 'mmdd'),
       sessionNumber);
end

if ~exist(saveFolder, 'dir')
    mkdir(saveFolder);
end

% Initialize camera
fprintf('Connecting to IP camera...\n');
try
    cam = ipcam(ipCamURL);
    fprintf('Camera connected successfully.\n');

    % Test camera connection with a single snapshot
    fprintf('Testing camera connection...\n');
    testImg = snapshot(cam);
    fprintf('Camera test successful. Image size: %dx%d\n', size(testImg,
       1), size(testImg, 2));

catch ME
    fprintf('Error connecting to camera: %s\n', ME.message);
    fprintf('Please check:\n');
    fprintf('1. Camera URL is correct: %s\n', ipCamURL);
    fprintf('2. Camera is accessible from your network\n');
    fprintf('3. Camera is not being used by another application\n');
    error('Camera connection failed. Cannot proceed with capture.');
```

```
end

%% PHASE 1: IMAGE CAPTURE
fprintf('=== PHASE 1: IMAGE CAPTURE ===\n');

% Store capture information for later processing
captureInfo = struct();
captureInfo.numImages = numImages;
captureInfo.filenames = cell(numImages, 1);
captureInfo.recordingStartTime = datetime('now'); % Store recording start
   time
captureInfo.captureTimestamps = cell(numImages, 1); % Store individual
   capture timestamps

% Wait for camera to stabilize
pause(1);

% FAST CAPTURE LOOP - NO PROCESSING
for i = 1:numImages
    try
        % Capture precise timestamp
        captureTime = datetime('now');
        captureTimeStr = datestr(captureTime, 'HH:MM:SS.FFF');

        % Calculate recording time (time since recording started)
        diff_time = captureTime - captureInfo.recordingStartTime;
        recordingTime = seconds(diff_time);
        recordingTimeStr = sprintf('%.3f', recordingTime);
       % recordingTimeStr = strrep(recordingTimeStr, '.', '_'); % Replace
          . with _ for filename

        % Store the actual capture timestamp for later use
        captureInfo.captureTimestamps{i} = captureTime;

        % Capture image
        img = snapshot(cam);

        % Verify image was captured successfully
        if isempty(img)
            fprintf('Warning: Empty image captured at frame %d\n', i);
            continue;
        end

        % Create filename and save (clean filename without special
           characters)
        filename = sprintf('Image_%04d_of_%04d_Time_%s_RecTime_%ss.jpg', i
           , numImages, ...
            strrep(strrep(captureTimeStr, ':', ''), '.', '_'), strrep(
               recordingTimeStr, '.', '_'));
        fullFilename = fullfile(saveFolder, filename);
        imwrite(img, fullFilename);

        % Store filename for later processing
        captureInfo.filenames{i} = fullFilename;
```

```
        % Progress update
        if mod(i, 50) == 0 || i == 1
            fprintf('  Captured: %d/%d images\n', i, numImages);
        end

    catch ME
        fprintf('Error capturing image %d: %s\n', i, ME.message);
        continue;
    end

    % Add delay
    pause(captureInterval);
end

fprintf('=== IMAGE CAPTURE COMPLETE ===\n');
fprintf('Total images captured: %d\n', captureInfo.numImages);

% Cleanup camera connection after capture
clear cam;

%% PHASE 2: POST-PROCESSING WITH TRACKING
fprintf('\n=== PHASE 2: IMAGE TRACKING POST-PROCESSING ===\n');

% Function to format recording time as MM:SS.MMM
formatRecordingTime = @(timeInSeconds) sprintf('%02d:%06.3f', floor(
   timeInSeconds/60), mod(timeInSeconds, 60));

% Initialize tracking data file
trackingDataFile = fullfile(saveFolder, 'tracking_data.csv');
fileID = fopen(trackingDataFile, 'w');
fprintf(fileID, 'Capture Interval: %.2f seconds\n', captureInterval);
fprintf(fileID, 'Recording Start Time: %s\n', datestr(captureInfo.
   recordingStartTime, 'yyyy-mm-dd HH:MM:SS.FFF'));
fprintf(fileID, 'Image,Recording_Time_MM_SS_MMM,X,Y,Validity\n'); %
   Updated column headers

% Load first image for point selection
fprintf('Loading first image for point selection...\n');
firstImagePath = captureInfo.filenames{1};
initialFrame = imread(firstImagePath);

% Let user select point to track
figure('Name', 'Select Point to Track', 'Position', [100, 100, 800, 600]);
imshow(initialFrame);
title('Click on the point you want to track');
[x, y] = ginput(1);
close;

% Initialize point tracker
pointTracker = vision.PointTracker('MaxBidirectionalError', 2);
initialize(pointTracker, [x y], initialFrame);
currentPoint = [x y];

% Track through all captured images
totalImagesProcessed = 0;
trackingPoints = NaN(numImages, 2);
```

```
validityFlags = false(numImages, 1);

for i = 1:captureInfo.numImages
    try
        % Load the captured image
        imagePath = captureInfo.filenames{i};
        img = imread(imagePath);

        % Calculate recording time using stored timestamp
        if ~isempty(captureInfo.captureTimestamps{i})
            recordingTimeSeconds = seconds(captureInfo.captureTimestamps{i
               } - captureInfo.recordingStartTime);
            recordingTimeFormatted = formatRecordingTime(
               recordingTimeSeconds);
        else
            % Fallback to calculated time if timestamp is missing
            recordingTimeSeconds = (i - 1) * captureInterval;
            recordingTimeFormatted = formatRecordingTime(
               recordingTimeSeconds);
        end

        % Track point in this frame
        [trackedPoint, validity] = step(pointTracker, img);

        if validity
            currentPoint = trackedPoint;
            trackingPoints(i, :) = currentPoint;
            validityFlags(i) = true;
            validityStr = 'Valid';
        else
            % Keep last known point but mark as invalid
            validityStr = 'Invalid';
            validityFlags(i) = false;

            % Try to re-initialize if tracking fails early in sequence
            if i <= 5
                fprintf('  Re-initializing tracker at image %d\n', i);
                release(pointTracker);
                pointTracker = vision.PointTracker('MaxBidirectionalError'
                    , 2);
                initialize(pointTracker, currentPoint, img);
                [trackedPoint, validity] = step(pointTracker, img);
                if validity
                    currentPoint = trackedPoint;
                    trackingPoints(i, :) = currentPoint;
                    validityFlags(i) = true;
                    validityStr = 'Valid';
                end
            end
        end

        % % Create and save image with tracking marker
        % imgWithMarker = insertMarker(img, currentPoint, 'plus', 'color',
           'red', 'size', 10);
        %
        % % Save tracked version
```

```
        % trackedFilename = sprintf('tracked_image_%03d.jpg', i);
        % trackedFullPath = fullfile(saveFolder, trackedFilename);
        % imwrite(imgWithMarker, trackedFullPath);

        % Save tracking data to CSV with formatted recording time
        fprintf(fileID, '%d,%s,%.2f,%.2f,%s\n', i, recordingTimeFormatted,
            currentPoint(1), currentPoint(2), validityStr);

        totalImagesProcessed = totalImagesProcessed + 1;

        % Progress update
        if mod(totalImagesProcessed, 50) == 0
            fprintf('  Tracking progress: %d/%d images processed (%.1f%%)\
               n', ...
                totalImagesProcessed, numImages, 100*totalImagesProcessed/
                   numImages);
        end

    catch ME
        fprintf('Error processing image %d: %s\n', i, ME.message);
        continue;
    end
end
fprintf('=== TRACKING ANALYSIS COMPLETE ===\n');

%% Cleanup and Summary
fclose(fileID);
release(pointTracker);

fprintf('\n=== SUMMARY ===\n');
fprintf('Results saved to: %s\n', saveFolder);
fprintf('Original images: image_*.jpg\n');
fprintf('Tracked images: tracked_image_*.jpg\n');
fprintf('Tracking data: %s\n', trackingDataFile);
fprintf('Total images processed: %d\n', totalImagesProcessed);
```

# D

# Appendix D: Arduino Control

First, provide the Arduino code, followed by the MATLAB code that interacts with the Arduino. Note that both programs use the same port, and therefore cannot run simultaneously.

```
#define MAX_COMMAND_LENGTH 32
#include <Adafruit_MCP4728.h>
#include <Wire.h>
#include <Arduino.h>

Adafruit_MCP4728 mcp;
int max_vol = 2640; //Max voltage from the DAC to HVA
int Va = max_vol*0.01; //Starting voltage low but not zero to see it is functioning
int dt = 600;
char receivedCommand[MAX_COMMAND_LENGTH];
volatile bool commandReceived = false;
\\if partial control add 'int DP = 4;//partial phase'

//Collects a full command line from the serial input until a newline is received.
void serialEvent() {
  static uint8_t cmdIndex = 0;
  while (Serial.available()) {
    char inChar = Serial.read();
    if (inChar == '\n') {
      receivedCommand[cmdIndex] = '\0';
      commandReceived = true;
      cmdIndex = 0;
      break;
    }
    if (cmdIndex < MAX_COMMAND_LENGTH - 1) {
      receivedCommand[cmdIndex++] = inChar;
    }
  }
}

//Change value depending on input (DT:x to change activation time and VA:x to change vo
void processDTCommand() {
  // Check for DT: prefix
  if (strncmp(receivedCommand, ”DT:”, 3) == 0) {
    float newDT = atof(receivedCommand + 3);
    if (newDT > 0) {
```

```
      dt = 1000*newDT;
      // Confirm receipt
      Serial.print(”dt updated: ”);
      Serial.println(dt);
    }
  }
    if (strncmp(receivedCommand, ”VA:”, 3) == 0) {
    float newVA = atof(receivedCommand + 3);
    if (newVA > 0) {
      Va = max_vol*newVA;
      // Confirm receipt
      Serial.print(”VA updated: ”);
      Serial.println(3.2*newVA);
    }
  }
}

void setup(void) {
  Serial.begin(115200);
  while (!Serial)
    delay(10); // will pause Zero, Leonardo, etc until serial console opens
  Serial.println(”Adafruit MCP4728 test!”);
  // Try to initialize!
  if (!mcp.begin()) {
    Serial.println(”Failed to find MCP4728 chip”);
    while (1) {
      delay(10);
    }
  }

  Serial.println(”found”);
mcp.setChannelValue(MCP4728_CHANNEL_A,0,MCP4728_VREF_INTERNAL,MCP4728_GAIN_2X);
mcp.setChannelValue(MCP4728_CHANNEL_B,0,MCP4728_VREF_INTERNAL,MCP4728_GAIN_2X);
mcp.setChannelValue(MCP4728_CHANNEL_C,0,MCP4728_VREF_INTERNAL,MCP4728_GAIN_2X);
mcp.setChannelValue(MCP4728_CHANNEL_D,0,MCP4728_VREF_INTERNAL,MCP4728_GAIN_2X);
mcp.saveToEEPROM();
}

void loop() {
if (commandReceived) {
    processDTCommand();
    commandReceived = false;
  }
  //Changing phase can also be done using 'mcp.fastWrite(0, 0, 0, 0);'
  // Update Channel A
  mcp.setChannelValue(MCP4728_CHANNEL_A, Va);
  mcp.setChannelValue(MCP4728_CHANNEL_B, 0);
  mcp.setChannelValue(MCP4728_CHANNEL_C, 0);
  mcp.setChannelValue(MCP4728_CHANNEL_D, 0);
  delay(dt);
  // Update Channel B
  mcp.setChannelValue(MCP4728_CHANNEL_A, 0);
  mcp.setChannelValue(MCP4728_CHANNEL_B, Va);
  mcp.setChannelValue(MCP4728_CHANNEL_C, 0);
  mcp.setChannelValue(MCP4728_CHANNEL_D, 0);
  delay(dt);
```

```
  // Update Channel C
  mcp.setChannelValue(MCP4728_CHANNEL_A, 0);
  mcp.setChannelValue(MCP4728_CHANNEL_B, 0);
  mcp.setChannelValue(MCP4728_CHANNEL_C, Va);
  mcp.setChannelValue(MCP4728_CHANNEL_D, 0);
  delay(dt);
}


//____For partial charged phase change____
  // Update Channel A and parial C
  mcp.setChannelValue(MCP4728_CHANNEL_A, Va);
  mcp.setChannelValue(MCP4728_CHANNEL_B, 0);
  mcp.setChannelValue(MCP4728_CHANNEL_C, Va/DP);
  mcp.setChannelValue(MCP4728_CHANNEL_D, 0);
  delay(dt);
  // Update Channel B and parial A
  mcp.setChannelValue(MCP4728_CHANNEL_A, Va/DP);
  mcp.setChannelValue(MCP4728_CHANNEL_B, Va);
  mcp.setChannelValue(MCP4728_CHANNEL_C, 0);
  mcp.setChannelValue(MCP4728_CHANNEL_D, 0);
  delay(dt);
  // Update Channel C and parial B
  mcp.setChannelValue(MCP4728_CHANNEL_A, 0);
  mcp.setChannelValue(MCP4728_CHANNEL_B, Va/DP);
  mcp.setChannelValue(MCP4728_CHANNEL_C, Va);
  mcp.setChannelValue(MCP4728_CHANNEL_D, 0);
  delay(dt);
```

To control Arduino using Matlab:

```
% --- Setup Arduino connection ---
arduinoObj = serialport(”COM4”,115200); % Connect to Arduino via serial
   port

% --- Wait for Arduino to be ready ---
fprintf('Waiting for Arduino to be ready...\n');
timeout = 10; % Wait up to 10 seconds
startTime = tic;
readyCount = 0;

while readyCount < 2 && toc(startTime) < timeout
    if arduinoObj.NumBytesAvailable > 0
        data = readline(arduinoObj);               % Read line from Arduino
        disp(”Arduino says: ” + data);             % Show Arduino message
        readyCount = readyCount + 1;               % Count ready signals
    end
    pause(0.1); % Prevent busy waiting
end

if readyCount < 2
    warning('Arduino may not be fully ready. Continuing anyway...');
end

% --- Send voltage amplitude to Arduino ---
fprintf('Setting voltage amplitude on Arduino...\n');
ArduinoInput = ”VA:” + num2str(VA) + ”\n”;
```

```
writeline(arduinoObj, ArduinoInput);

% --- Confirm Arduino response for VA ---
pause(0.5);
if arduinoObj.NumBytesAvailable > 0
    response = readline(arduinoObj);              % Read Arduino
       confirmation
    fprintf('Arduino VA response: %s\n', response);
end

% --- Loop: send new Dt value to Arduino ---
val_str = num2str(val);
ArduinoInput = ”DT:” + val_str + ”\n”;            % DT = frequency value
try
    writeline(arduinoObj, ArduinoInput);          % Send frequency
    fprintf('Sent to Arduino: %s', ArduinoInput);
catch ME
    fprintf('Error sending to Arduino: %s\n', ME.message);
end

% --- Read Arduino response with timeout ---
responseTimeout = 1; % 1 second
responseStart = tic;
while arduinoObj.NumBytesAvailable == 0 && toc(responseStart) <
   responseTimeout
    pause(0.01);
end
if arduinoObj.NumBytesAvailable > 0
    try
        data = readline(arduinoObj);              % Get Arduino response
        fprintf('Arduino response: %s\n', data);
    catch ME
        fprintf('Error reading Arduino response: %s\n', ME.message);
    end
else
    fprintf('No Arduino response within timeout\n');
end

% --- Cleanup: reset Arduino VA and close connection ---
ArduinoInput = ”VA:” + num2str(0.1) + ”\n”;       % Reset VA to safe value
writeline(arduinoObj, ArduinoInput);

try
    clear arduinoObj;                             % Close Arduino
       connection
    fprintf('Arduino connection closed.\n');
catch
    fprintf('Note: Arduino connection may have already been closed.\n');
end
```

# E

# Appendix E: Other Electrode Tests

**Response of the smaller 10-rectangle design when charging different phases at high voltage (1200 V). Red: X-coordinate; Blue: Y-coordinate; Green: total displacement from the starting position, computed via Pythagoras.**

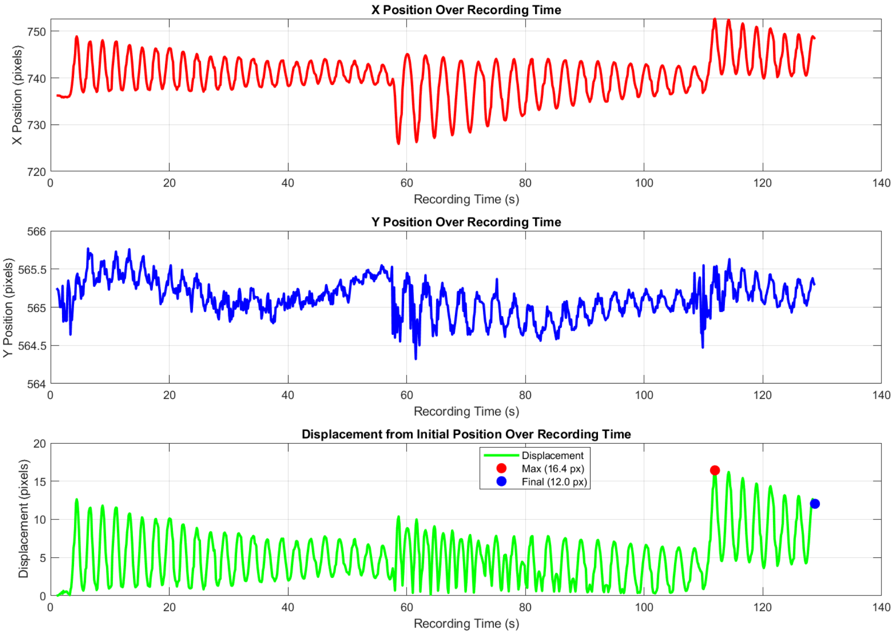

Figure E.1: Response to switching Phase 1 on and off. Resulting in displacement of average of 6.884 pixels.

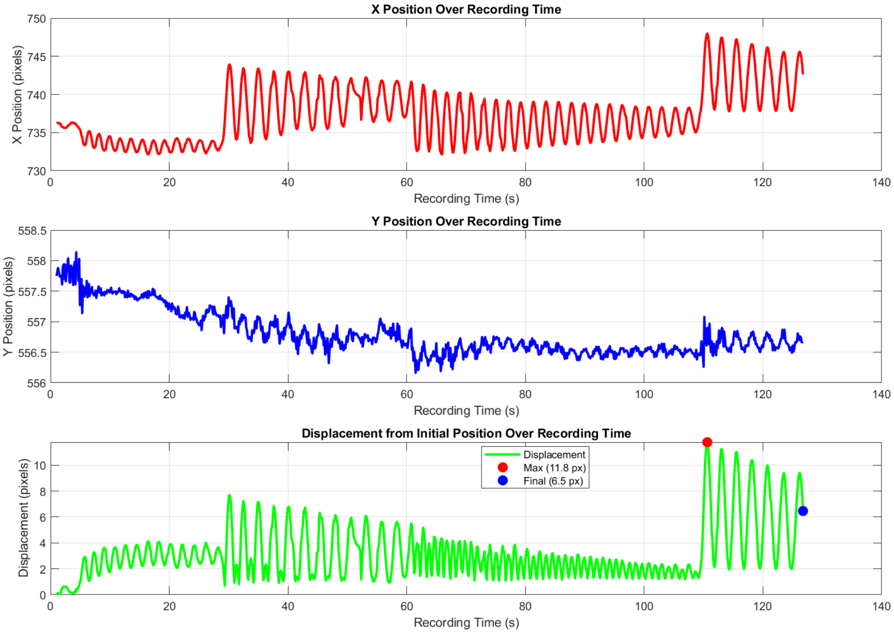

Figure E.2: Response to switching Phase 2 on and off. Resulting in displacement of average of 5.973 pixels.

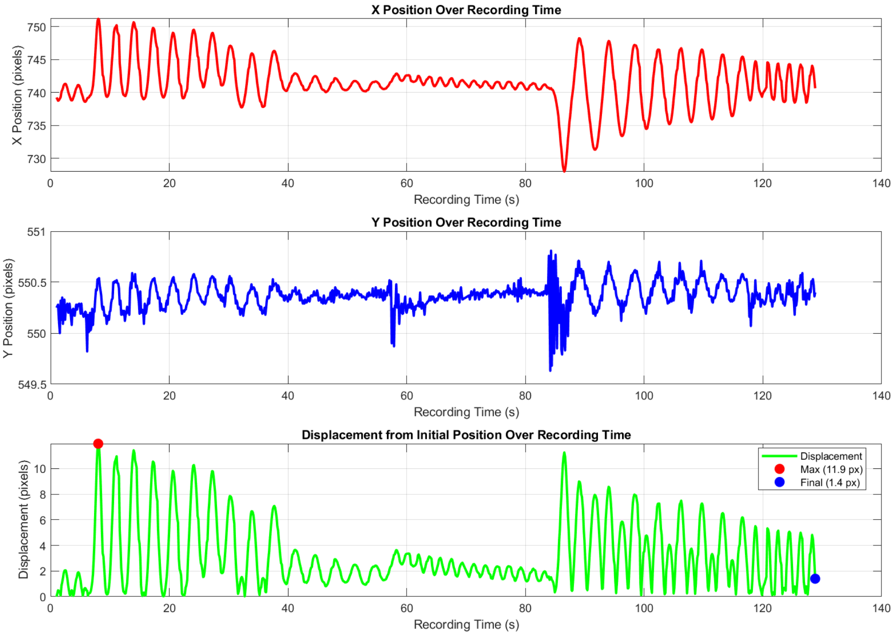

Figure E.3: Response to switching Phase 3 on and off. Resulting in displacement of average of 2.626 pixels.

**Response of the side-rail design when charging different phases at high voltage (1200 V). Red: X-coordinate; Blue: Y-coordinate; Green: total displacement from the starting position, computed via Pythagoras.**

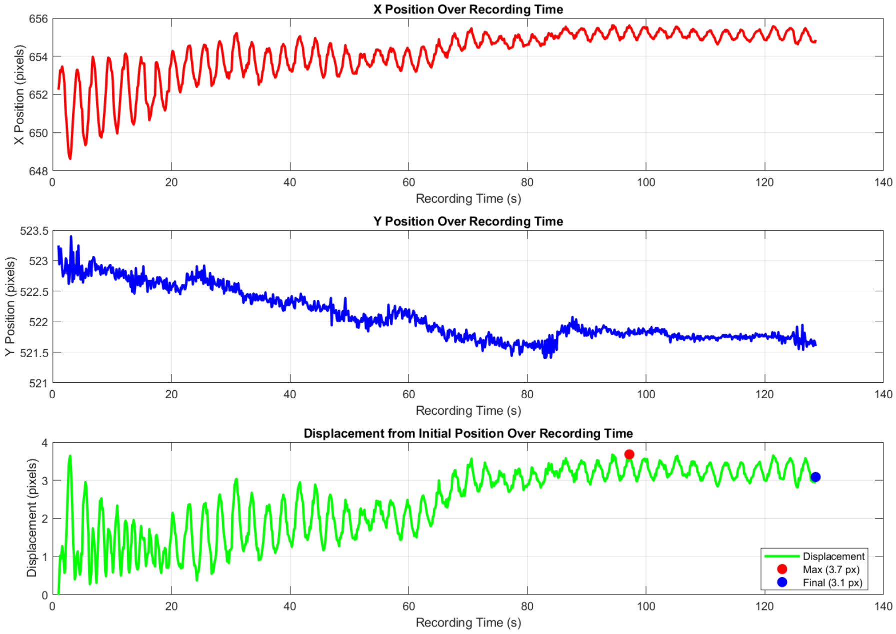

Figure E.4: Response to switching Phase 1 on and off. Resulting in displacement of average of 2.667 pixels.

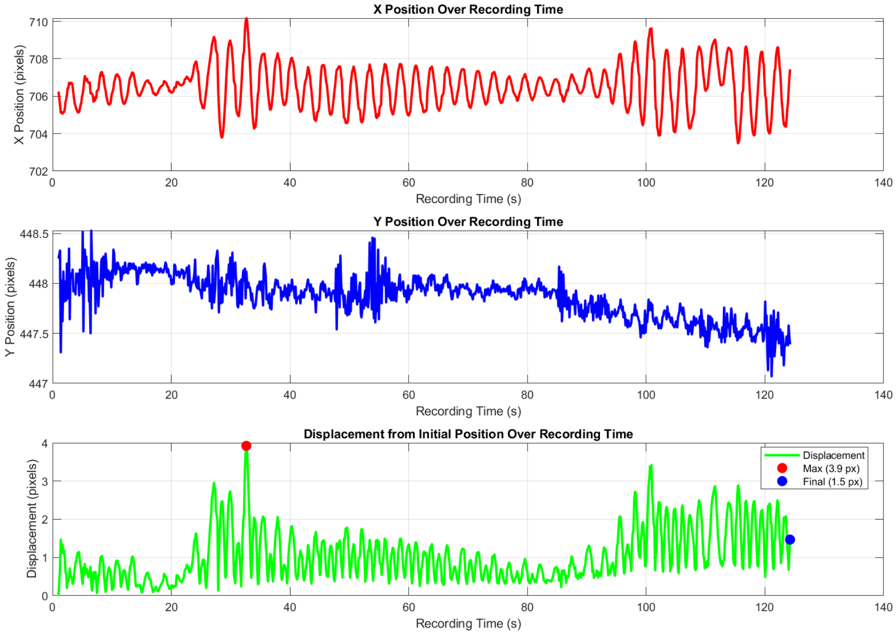

Figure E.5: Response to switching Phase 2 on and off. Resulting in displacement of average of 0.369 pixels.

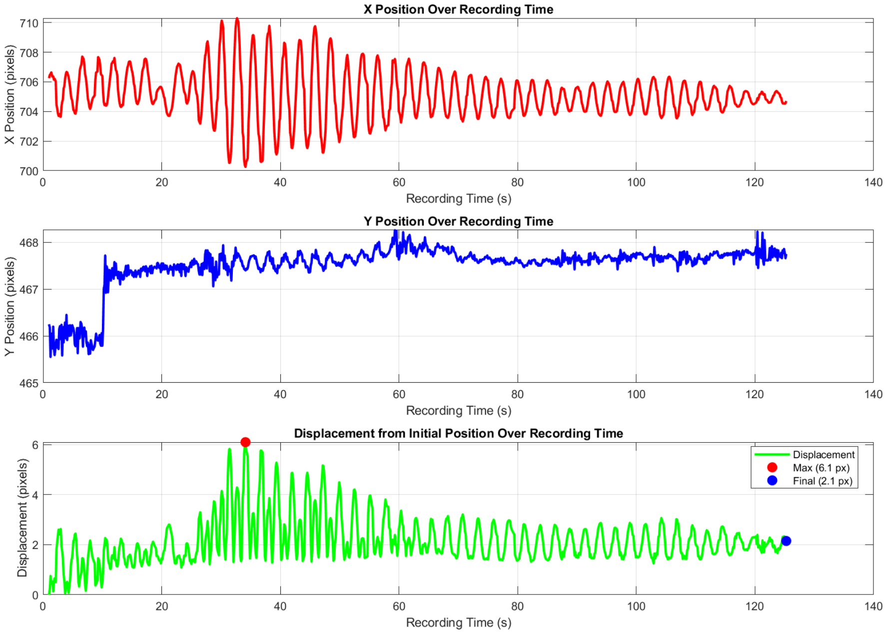

Figure E.6: Response to switching Phase 3 on and off. Resulting in displacement of average of 1.720 pixels.

# Bibliography

[1] ASML, *Mechanics and mechatronics at ASML*, 2024. [Online]. Available: `https://www.asml.com/en/technology/lithography-principles/mechanics-and-mechatronics`.

[2] E. E. Hunter, E. B. Steager, A. Hsu, A. Wong-Foy, R. Pelrine, and V. Kumar, "Nanoliter Fluid Handling for Microbiology Via Levitated Magnetic Microrobots," *IEEE Robotics and Automation Letters*, vol. 4, no. 2, pp. 997–1004, Apr. 2019, Conference Name: IEEE Robotics and Automation Letters, ISSN: 2377-3766. DOI: `10.1109/LRA.2019.2893682`. [Online]. Available: `https://ieeexplore-ieee-org.tudelft.idm.oclc.org/document/8616901` (visited on 06/02/2024).

[3] R. Pelrine, A. Hsu, A. Wong-Foy, B. McCoy, and C. Cowan, "Optimal control of diamagnetically levitated milli robots using automated search patterns," in *2016 International Conference on Manipulation, Automation and Robotics at Small Scales (MARSS)*, Jul. 2016, pp. 1–6. DOI: `10.1109/MARSS.2016.7561725`. [Online]. Available: `https://ieeexplore-ieee-org.tudelft.idm.oclc.org/document/7561725` (visited on 06/02/2024).

[4] K. S. Vikrant and G. R. Jayanth, "Diamagnetically levitated nanopositioners with large-range and multiple degrees of freedom," en, *Nature Communications*, vol. 13, no. 1, p. 3334, Jun. 2022, Publisher: Nature Publishing Group, ISSN: 2041-1723. DOI: `10.1038/s41467-022-31046-4`. [Online]. Available: `https://www-nature-com.tudelft.idm.oclc.org/articles/s41467-022-31046-4` (visited on 06/14/2024).

[5] B. V. Johnson, N. Esantsi, and D. J. Cappelleri, "Design of the $\mu$MAZE Platform and Microrobots for Independent Control and Micromanipulation Tasks," *IEEE Robotics and Automation Letters*, vol. 5, no. 4, pp. 5677–5684, Oct. 2020, Conference Name: IEEE Robotics and Automation Letters, ISSN: 2377-3766. DOI: `10.1109/LRA.2020.3010210`. [Online]. Available: `https://ieeexplore-ieee-org.tudelft.idm.oclc.org/document/9143422` (visited on 06/21/2024).

[6] A. Hsu, A. Wong-Foy, B. McCoy, *et al.*, "Application of micro-robots for building carbon fiber trusses," in *2016 International Conference on Manipulation, Automation and Robotics at Small Scales (MARSS)*, Jul. 2016, pp. 1–6. DOI: `10.1109/MARSS.2016.7561729`. [Online]. Available: `https://ieeexplore-ieee-org.tudelft.idm.oclc.org/document/7561729` (visited on 06/24/2024).

[7] A. Hsu, C. Cowan, W. Chu, *et al.*, "Automated 2D micro-assembly using diamagnetically levitated milli-robots," in *2017 International Conference on Manipulation, Automation and Robotics at Small Scales (MARSS)*, Jul. 2017, pp. 1–6. DOI: `10.1109/MARSS.2017.8001926`. [Online]. Available: `https://ieeexplore-ieee-org.tudelft.idm.oclc.org/document/8001926` (visited on 06/24/2024).

[8] A. Hsu, W. Chu, C. Cowan, *et al.*, "Diamagnetically levitated Milli-robots for heterogeneous 3D assembly," en, *Journal of Micro-Bio Robotics*, vol. 14, no. 1, pp. 1–16, Jun. 2018, ISSN: 2194-6426. DOI: `10.1007/s12213-018-0103-4`. [Online]. Available: `https://doi.org/10.1007/s12213-018-0103-4` (visited on 06/06/2024).

[9] A. Hsu, H. Zhao, M. Gaudreault, A. W. Foy, and R. Pelrine, "Magnetic Milli-Robot Swarm Platform: A Safety Barrier Certificate Enabled, Low-Cost Test Bed," *IEEE Robotics and Automation Letters*, vol. 5, no. 2, pp. 2913–2920, Apr. 2020, Conference Name: IEEE Robotics and Automation Letters, ISSN: 2377-3766. DOI: `10.1109/LRA.2020.2974713`. [Online]. Available: `https://ieeexplore-ieee-org.tudelft.idm.oclc.org/document/9001174` (visited on 06/21/2024).

[10] A. Hsu, R. Pelrine, R. de Gouvea Pinto, and E. W. Schaler, “2D-Compliant, Diamagnetic Levitating Micro-Robots for Operation on Non-Flat, Non-Clean Tracks,” in *2022 International Conference on Manipulation, Automation and Robotics at Small Scales (MARSS)*, Jul. 2022, pp. 1–7. DOI: `10.1109/MARSS55884.2022.9870462`. [Online]. Available: `https://ieeexplore-ieee-org.tudelft.idm.oclc.org/abstract/document/9870462?casa_token=d_s1yYe-sDIAAAAA:nYf_RUv4GP9EgAtoOytMsqCALjtzKHgfVjhS4Gtm6Y_CXfLO7CFuvJLc-_22PTYHmeCyaLEg7` (visited on 05/31/2024).

[11] R. Seth, S. Halder, K. Chatterjee, S. Mandal, and Nagahanumaiah, “Magnetically levitated X–Y plane actuator for micromanufacturing,” en, *Journal of Micromanufacturing*, vol. 3, no. 1, pp. 13–19, May 2020, Publisher: SAGE Publications India, ISSN: 2516-5984. DOI: `10.1177/2516598419896127`. [Online]. Available: `https://doi.org/10.1177/2516598419896127` (visited on 07/01/2024).

[12] H. Sugimoto, T. Hashimoto, T. Arai, H. Suzuki, and A. Chiba, “Novel Bearingless Motor Topology With Diamagnetic Salient-Pole Rotor,” *IEEE Transactions on Industry Applications*, vol. 59, no. 2, pp. 1639–1647, Mar. 2023, Conference Name: IEEE Transactions on Industry Applications, ISSN: 1939-9367. DOI: `10.1109/TIA.2022.3227527`. [Online]. Available: `https://ieeexplore-ieee-org.tudelft.idm.oclc.org/abstract/document/9976237?casa_token=oGGYCg1HZaQAAAAA:iOmqEH7rIeS6o4cQB80m7YBkAbOqaHZWKCmZI-0jSiDf52brkn_JtOFrxQ_cj4smEf3AT3BDZg` (visited on 05/31/2024).

[13] R. Pelrine, A. Hsu, and A. Wong-Foy, “Methods and Results for Rotation of Diamagnetic Robots Using Translational Designs,” in *2019 International Conference on Manipulation, Automation and Robotics at Small Scales (MARSS)*, Jul. 2019, pp. 1–6. DOI: `10.1109/MARSS.2019.8860975`. [Online]. Available: `https://ieeexplore-ieee-org.tudelft.idm.oclc.org/document/8860975` (visited on 06/24/2024).

[14] M. Kobayashi and J. Abe, “Optical Motion Control of Maglev Graphite,” *Journal of the American Chemical Society*, vol. 134, no. 51, pp. 20 593–20 596, Dec. 2012, Publisher: American Chemical Society, ISSN: 0002-7863. DOI: `10.1021/ja310365k`. [Online]. Available: `https://doi.org/10.1021/ja310365k` (visited on 05/31/2024).

[15] Y. Ozawa, Y. Fujii, A. Chiba, H. Sugimoto, H. Suzuki, and H. Bleuler, “Principles and Test Result of Novel Full Passive Magnetic Levitation Motor with Diamagnetic Disk,” in *2021 IEEE Energy Conversion Congress and Exposition (ECCE)*, ISSN: 2329-3748, Oct. 2021, pp. 3943–3948. DOI: `10.1109/ECCE47101.2021.9595636`. [Online]. Available: `https://ieeexplore-ieee-org.tudelft.idm.oclc.org/abstract/document/9595636?casa_token=FLxShZptET0AAAAA:sKtoerehu3pm7JTY0rPVIkb17gtWZTdNXqORu6lkoCEzAVaF4GwCsqpDUIgcuativ` (visited on 05/31/2024).

[16] A. Cansiz and J. Hull, “Stable load-carrying and rotational loss Characteristics of diamagnetic bearings,” *IEEE Transactions on Magnetics*, vol. 40, no. 3, pp. 1636–1641, May 2004, Conference Name: IEEE Transactions on Magnetics, ISSN: 1941-0069. DOI: `10.1109/TMAG.2004.827181`. [Online]. Available: `https://ieeexplore.ieee.org/document/1298938` (visited on 05/30/2024).

[17] S. Yee, L. Oney, T. Cosby, D. P. Durkin, and H. ElBidweihy, “Photothermal actuation of levitated pyrolytic graphite revised,” en, *APL Materials*, vol. 9, no. 10, p. 101 107, Oct. 2021, ISSN: 2166-532X. DOI: `10.1063/5.0061390`. [Online]. Available: `https://pubs.aip.org/apm/article/9/10/101107/1061600/Photothermal-actuation-of-levitated-pyrolytic` (visited on 05/31/2024).

[18] M. Beauchamp, S. Yee, I. O’Carroll, E. Chapman, and H. ElBidweihy, “Optically Powered Milli-Scale Robot System for Nanoliter Fluid Delivery Based on Diamagnetic Levitation,” *IEEE Transactions on Magnetics*, vol. 59, no. 11, pp. 1–5, Nov. 2023, Conference Name: IEEE Transactions on Magnetics, ISSN: 1941-0069. DOI: `10.1109/TMAG.2023.3281968`. [Online]. Available: `https://ieeexplore-ieee-org.tudelft.idm.oclc.org/abstract/document/10141637?casa_token=0k8gYzzxOOYAAAAA:gUdS1K6M4d4-PqpMOD8msTJ0ZHopFTpk7XpV0y66wCCaY sHMBAGP_E4A` (visited on 05/31/2024).

[19] J. H. Kim, J.-B. Pyo, and T.-S. Kim, “Highly Mobile Levitating Soft Actuator Driven by Multistimuli-Responses,” en, *Advanced Materials Interfaces*, vol. 7, no. 21, p. 2 001 051, 2020, _eprint: https://onlinelibrary.wiley ISSN: 2196-7350. DOI: 10.1002/admi.202001051. [Online]. Available: https://onlinelibrary-wiley-com.tudelft.idm.oclc.org/doi/abs/10.1002/admi.202001051 (visited on 06/24/2024).

[20] M. Ewall-Wice, S. Yee, K. DeLawder, *et al.*, “Optomechanical Actuation of Diamagnetically Levitated Pyrolytic Graphite,” *IEEE Transactions on Magnetics*, vol. 55, no. 7, pp. 1–6, Jul. 2019, Conference Name: IEEE Transactions on Magnetics, ISSN: 1941-0069. DOI: 10.1109/TMAG.2019.2892332. [Online]. Available: https://ieeexplore-ieee-org.tudelft.idm.oclc.org/document/8624587 (visited on 07/01/2024).

[21] R. Moser and H. Bleuler, “Precise positioning using electrostatic glass motor with diamagnetically suspended rotor,” *IEEE Transactions on Applied Superconductivity*, vol. 12, no. 1, pp. 937–939, Mar. 2002, Conference Name: IEEE Transactions on Applied Superconductivity, ISSN: 1558-2515. DOI: 10.1109/TASC.2002.1018553. [Online]. Available: https://ieeexplore-ieee-org.tudelft.idm.oclc.org/document/1018553 (visited on 06/02/2024).

[22] Y. Xu, Q. Cui, R. Kan, H. Bleuler, and J. Zhou, “Realization of a Diamagnetically Levitating Rotor Driven by Electrostatic Field,” *IEEE/ASME Transactions on Mechatronics*, vol. 22, no. 5, pp. 2387–2391, Oct. 2017, Conference Name: IEEE/ASME Transactions on Mechatronics, ISSN: 1941-014X. DOI: 10.1109/TMECH.2017.2718102. [Online]. Available: https://ieeexplore-ieee-org.tudelft.idm.oclc.org/document/7954634 (visited on 06/03/2024).

[23] A. Keşkekler, “Characterization and Dynamics of Diamagnetically Levitated Objects,” en, *TU Delft Repository*, 2018. [Online]. Available: https://repository.tudelft.nl/record/uuid:a7878642-2b9e-467e-af5a-d5a846f5f039 (visited on 05/23/2024).

[24] F. Barrot, D. Chapuis, T. Bosgiraud, *et al.*, “Preliminary Investigations on a Diamagnetically Levitated Linear Conveyor,” *IEEJ Transactions on Industry Applications*, vol. 126, no. 10, pp. 1341–1344, 2006. DOI: 10.1541/ieejias.126.1341.

[25] Y. Xu, R. Ling, J. Mahfoud, L. Yang, and J. Zhou, “Numerical and experimental investigations on the influence factors of diamagnetic levitated electrostatic motor,” en, *Journal of the Brazilian Society of Mechanical Sciences and Engineering*, vol. 46, no. 8, p. 468, Jun. 2024, ISSN: 1806-3691. DOI: 10.1007/s40430-024-05047-x. [Online]. Available: https://doi.org/10.1007/s40430-024-05047-x (visited on 07/01/2024).

[26] J. Jin, T. Yih, T. Higuchi, and J. U. Jeon, “Direct electrostatic levitation and propulsion of silicon wafer,” *IEEE Transactions on Industry Applications*, vol. 34, no. 5, pp. 975–984, Sep. 1998, Conference Name: IEEE Transactions on Industry Applications, ISSN: 1939-9367. DOI: 10.1109/28.720437. [Online]. Available: https://ieeexplore-ieee-org.tudelft.idm.oclc.org/document/720437 (visited on 06/14/2024).

[27] A. Karbache and P. Steeneken, “Electrostatic positioning of diamagnetically levitating motion stages, master thesis,” *TU Delft Repository*, no. ED 2024.035, Jun. 2024. [Online]. Available: https://resolver.tudelft.nl/uuid:f5406288-6fed-4d0d-ad19-705302a8e72a.

[28] ANSYS, Inc., *Granta edupack software*, https://www.ansys.com/materials, version 23.2.1, Cambridge, UK, Jun. 2024.

[29] D. B. Fischbach, “Diamagnetic Susceptibility of Pyrolytic Graphite,” *Physical Review*, vol. 123, no. 5, pp. 1613–1614, Sep. 1961, Publisher: American Physical Society. DOI: 10.1103/PhysRev.123.1613. [Online]. Available: https://link.aps.org/doi/10.1103/PhysRev.123.1613 (visited on 06/12/2024).

[30] R. D. Waldron, “Diamagnetic Levitation Using Pyrolytic Graphite,” *Review of Scientific Instruments*, vol. 37, no. 1, pp. 29–35, Jan. 1966, ISSN: 0034-6748. DOI: 10.1063/1.1719946. [Online]. Available: https://doi.org/10.1063/1.1719946 (visited on 06/12/2024).

[31] N. Kothari, “Diamagnetically Levitated Resonant Mass Sensor: Master of Science Thesis,” en, *TU Delft Repository*, 2019. [Online]. Available: https://repository.tudelft.nl/islandora/object/uuid%3Ac037c432-1649-47c2-bd1c-a5662663a716 (visited on 05/23/2024).

[32] X. Chen, “Dynamics of diamagnetically levitating resonators,” en, Ph.D. dissertation, Delft University of Technology, 2023. DOI: `10.4233/UUID:6C4F32EE-60EC-4508-887D-A0066692F5F4`. [Online]. Available: `http://resolver.tudelft.nl/uuid:6c4f32ee-60ec-4508-887d-a0066692f5f4` (visited on 05/23/2024).

[33] T. de Lint, “Investigation of the nonlinear dy namics of a dia magnetically lev itating plate,” en, *TU Delft Repository*, Aug. 2021.

[34] F. Barrot, J. Sandtner, and H. Bleuler, “Acceleration Sensor Based on Diamagnetic Levitation,” en, in *IUTAM Symposium on Vibration Control of Nonlinear Mechanisms and Structures*, H. Ulbrich and W. GÜnthner, Eds., Dordrecht: Springer Netherlands, 2005, pp. 81–90, ISBN: 978-1-4020-4161-7. DOI: `10.1007/1-4020-4161-6_6`.

[35] Y. Su, Z. Xiao, Z. Ye, and K. Takahata, “Micromachined Graphite Rotor Based on Diamagnetic Levitation,” *IEEE Electron Device Letters*, vol. 36, no. 4, pp. 393–395, Apr. 2015, Conference Name: IEEE Electron Device Letters, ISSN: 1558-0563. DOI: `10.1109/LED.2015.2399493`. [Online]. Available: `https://ieeexplore.ieee.org/document/7031404` (visited on 05/30/2024).

[36] Q. Gao, H. Yan, H. Zou, *et al.*, “Magnetic levitation using diamagnetism: Mechanism, applications and prospects,” en, *Science China Technological Sciences*, vol. 64, no. 1, pp. 44–58, Jan. 2021, ISSN: 1869-1900. DOI: `10.1007/s11431-020-1550-1`. [Online]. Available: `https://doi.org/10.1007/s11431-020-1550-1` (visited on 05/31/2024).

[37] M. D. Simon and A. K. Geim, “Diamagnetic levitation: Flying frogs and floating magnets (invited),” *Journal of Applied Physics*, vol. 87, no. 9, pp. 6200–6204, May 2000, ISSN: 0021-8979. DOI: `10.1063/1.372654`. [Online]. Available: `https://doi.org/10.1063/1.372654` (visited on 06/06/2024).

[38] S. D. Senturia, “Microsystem design,” en, in *Microsystem design*, 51, NEW YORK, BOSTON, DORDRECHT, LONDON, MOSCOW: KLUWER ACADEMIC PUBLISHERS, 2005, pp. 110–112, ISBN: 0-7923-7246-8, 0-306-47601-0.

[39] S. Kang, J. Kim, J.-B. Pyo, J. H. Cho, and T.-S. Kim, “Design of Magnetic Force Field for Trajectory Control of Levitated Diamagnetic Graphite,” en, *International Journal of Precision Engineering and Manufacturing-Green Technology*, vol. 5, no. 2, pp. 341–347, Apr. 2018, ISSN: 2198-0810. DOI: `10.1007/s40684-018-0036-3`. [Online]. Available: `https://doi.org/10.1007/s40684-018-0036-3` (visited on 06/02/2024).

[40] K. Poletkin, *Levitation Micro-Systems*. Springer, Dec. 2020.

[41] growescience, *ELECTROSTATIC PRESSURE*, Feb. 2021. [Online]. Available: `https://physicspages.com/pdf/Electrodynamics/Electrostatic%20pressure.pdf`.

[42] P. G. Steeneken, *Introductory Dynamics: 2D Kinematics and Kinetics of Point Masses and Rigid Bodies*. TU Delft OPEN Publishing., Dec. 2023. DOI: `10.59490/tb.83`. [Online]. Available: `https://doi.org/10.59490/tb.83`.